UNIVERSIDADE DE SÃO PAULO
FACULDADE DE FILOSOFIA CIÊNCIAS E LETRAS DE RIBEIRÃO PRETO
PROGRAMA DE PÓS-GRADUAÇÃO EM FÍSICA APLICADA A MEDICINA E BIOLOGIA

Caracterização óptica de amostras altamente espalhadoras na região do visível e infravermelho próximo

Luismar Barbosa da Cruz Junior

Ribeirão Preto
2023
Luismar Barbosa da Cruz Junior

Optical characterization of highly turbid samples in the visible and near infrared spectra

Tese submetida à Faculdade de Fílosofia, Ciências e Letras de Ribeirão Preto da Universidade de São Paulo como requisito parcial para a obtenção do título de Doutor em Ciências.

Área de Concentração: Física Aplicada a Medicina e Biologia
Orientador: Prof. Dr. Luciano Bachmann

Versão corrigida da tese de doutorado apresentada ao programa de pós-graduação em Física Aplicada à Medicina e Biologia em 07 de março de 2023.

Ribeirão Preto

2023

Ficha Catalográfica

Cruz Junior, Luismar Barbosa da

Caracterização óptica de amostras altamente espalhadoras na região do visível e infravermelho próximo. Ribeirão Preto, 2023. 104p.

Tese de Doutorado, apresentada à Faculdade de Filosofia, Ciências e Letras de Ribeirão Preto/USP. Área de concentração: Física Aplicada e Medicina e Biologia. Orientador: Bachmann, Luciano

1. Espectroscopia. 2. Propriedades ópticas. 3. Colorimetria. 4. Ângulo de tipologia individual. 5. Tecido biológico.

Tese de autoria de Luismar Barbosa da Cruz Junior, apresentada ao Departamento de Física da FFCLRP-USP como parte das exigências para obtenção do título de Doutor em Ciências pelo programa de pós-graduação em Física Aplicada à Medicina e Biologia.

Título: Caracterização óptica de amostras altamente espalhadoras na região do visível e infravermelho próximo.
Title: Optical characterization of highly turbid samples in the visible and near infrared spectra.

O presente trabalho em nível de Doutorado foi avaliado em 2023, pela banca examinadora composta pelos seguintes membros:

Prof.(a) Dr. (a) Rickson Coelho Mesquita
Unicamp

Prof.(a) Dr. (a) Cristiano de Mello Gallep
Unicamp

Dr. (a) Thereza Cury Fortunato
Pesquisadora na Tergos Pesquisa e Ensino Ltda.

Ribeirão Preto, 2023.

To my wife and family, who I love unconditionally.

ACKNOWLEDGEMENT

Primeiramente, eu gostaria de agradecer ao professor Dr. Luciano Bachmann, por aceitar me orientar durante o doutorado no programa de pós-graduação em física aplicada a medicina e biologia da USP de Ribeirão Preto. Graças aos seus conhecimentos pude me tornar um pesquisador melhor, mas também uma pessoa mais humana. Seus ensinamentos serão levados para a vida.

Minha esposa Danielly Mota, que me acompanha desde a graduação, obrigado por todo o suporte ao longo de todos esses anos. Agradeço aos meus pais, Luismar Barbosa e Marli Rios, pela educação e incentivo. Agradeço aos meus avós, Elisabeth Akegawa e Mauro Gonçalves, por terem cuidado de mim desde pequeno. Agradeço à minha tia Marcia Rios e primos Marcio Guimarães e Roberto Freitas, que me acolheram como filho e irmão. Minhas irmãs Nayara Gonçalves e Monika Freitas, obrigado por todo carinho. Amo muito cada um de vocês do fundo do meu coração.

An meine ewigen Freunde aus Deutschland. 2021 hatte ich die Gelegenheit, die Stadt Ulm kennenzulernen. In dieser kleinen Ecke Deutschlands habe ich viele Freunde gefunden, die ich Leben lang mitnehmen werde. Zuerst möchte ich Herrn Professor Alwin Kienle für alles danken. Sie waren mir ein Mentor und ein Freund. Philipp und Karsten sind wie große Brüder, die mich durch alle Schwierigkeiten geführt haben und hatten Geduld, dass ich jeden Tag, fast stündlich, an ihrer Tür klopfte und sie um Hilfe oder Rat bat. Die Gespräche auf Spanisch mit Daniel Claus waren einzigartig. Florian Forschum und Andrei sind wunderbare Menschen mit unendlichem Wissen. Danke Felix, Benjamin, Christian, Thomas, Stefan, Markus, Niklas, Alexander Hack, Karl Stock und vielen anderen Freunden. Ich hoffe, dass wir uns in Zukunft wiedersehen können.

Não posso esquecer também da minha professora de Alemão Barbara Emylly Tomaz dos Santos do curso de Alemão Portudeusch, que me ensinou muito sobre a lingua e cultura alemã. Graças a você pude compreender muito de um lugar que tanto me acolheu.

Ao longo desses 4 anos de doutorado, tive a oportunidade de conhecer diversos professores que me ajudaram em diversos aspectos. Dentre esses professores, gostaria de citar alguns que são especiais e estiveram sempre presentes em cada etapa dessa jornada. Professor “Jabá” foi orientador de mestrado da minha esposa, ele possui um coração de ouro e me tratou como um de seus “filhos”, obrigado por toda a sua gentileza. O professor Baffa sempre contanto histórias intressantes e expandindo meus horizontes como pesquisador, por isso, eu agradeço por toda a sua sabedoria. Os professores George e Theo foram cruciais para o bom desenvolvimento

ciêntifico deste trabalho, dando diversas contribuições intelectuais e ajudando a montar um trabalho sólido e único, além de sempre me ajudarem nos momentos dificeis.

Nilza por me ajudar com cada duvida que eu tinha, mesmo que era só ler algum documento no regulamento. Prometo que serei mais atento no futuro. Obrigado Dona Fátima, carinhosamente chamada de Tia Fátima, sempre dando seu alegre bom dia com um sorriso e cuidando da limpeza e organização das salas de estudo e laboratórios.

Amigos do grupo de fotobiofísica Raquel, Bassam, Jaqueline, Guilherme, Raissa, Kaio, Andre, Eduardo, e Murilo vocês são incriveis! Obrigado Emanuel, Natália, Bunoro, Felipe, Seth, Sudi, José Eduardo, Renan, Ricardo, Renata, Gabi e Arthur Tia. Cada um dos meus amigos de departamento foram extremamente importantes para chegar até o fim do doutorado.

Os amigos feitos durante vários periodos da vida sempre serão lembrados. Agradeço aos meus amigos de infância Vinicius Pereira, Luciano, Vinicius e Gustavo Juliate, e Rafael Augusto. Obrigado aos meus amigos de Uberlândia, Gustavo, Lucas, João Paulo, Cássio, Vinicius Leo, Michel, Rafael, Japa. Aos meus amigos da graduação em Física da UFU Marcos, Wellington, Arnaldo, e orientador de mestrado Adamo, vocês sempre serão lembrados com muito carinho ao longo de toda a minha vida. Agradeço também aos amigos que vieram após o casamento, Allysson, Thaina, Alexandre, Mara, Paula e muitos outros.

Agradeço a USP por toda a insfraestrutura fornecida, indo desde laboratórios equipados com instrumentos de pesquisa especializados, computadores, e ambiente propicio para o ensino, pesquisa e extensão. Tive a oportunidade de realizar diversas disciplinas que me auxiliaram na minha formação profissional e tive muitos encontros que expariram meus horizontes.

Por fim, agradeço a CAPES que foi a fundação de amparo que manteve minha bolsa de pesquisa e de intercâmbio ao longo desses 6 anos. Fui aluno de mestrado CAPES, fui aluno de doutorado CAPES, e fui aluno de intercâmbio CAPES. Sem esse auxilio seria impossivel chegar onde estou. Meu mais sincero agradecimento e respeito.

“The important thing is not to stop questioning.
Curiosity has its own reason for existing.”
(Albert Einstein)

Caracterização óptica de amostras altamente espalhadoras na região do visível e infravermelho próximo

RESUMO

Altas concentrações de melanina em peles escuras pode afetar negativamente os resultados em diagnósticos e tratamentos baseados em luz. As propriedades ópticas de peles escuras são conhecidas na literatura, mas até o momento, não havia uma correlação entre as propriedades ópticas e o fototipo de pele através de uma classificação confiável e reprodutível. O ângulo de tipologia individual (ITA) foi desenvolvido na década de 90 para classificar o fenótipo de peles utilizando medidas colorimétricas com equipamentos calibrados. O ITA é diretamente relacionado a constituição química da pigmentação da pele e pode ser usado como um método confiável de categorização das peles. Neste estudo, diferentes fototipos de peles ex-vivo foram opticamente caracterizados, avaliando o coeficiente de absorção, espalhamento, atenuação efetiva, penetração óptica e albedo. Cada um desses parâmetros ópticos possui relevância em aplicações biofotônicas nas ciências da saúde. Para mensurar essas propriedades, foram manufaturadas, caracterizadas e validadas um sistema de esferas integradoras em 3D. Os resultados obtidos indicam a existência de uma correlação entre o ITA e as propriedades ópticas das peles com diferente fototipos. O coeficiente de absorção e atenuação efetiva aumentam com a redução do ITA, ou seja, peles escuras absorvem mais luz. Por outro lado, a penetração óptica e a albedo é maior para maiores ITAs. O coeficiente de espalhamento teve poucas alterações em função dos fototipo de pele. Com os dados experimentais do coeficiente de absorção foi possível determinar um modelo experimental para estimar o coeficiente de absorção usando apenas os parâmetros colorimétricos do ITA, abrindo novas oportunidades para correções em dispositivos ópticos como oxímetros de pulso, relógios inteligentes, oximetria fotoacústica, e outros. Por fim, é apresentado um trabalho desenvolvido durante o intercâmbio no Institut für Lasertechnologien in der Medizin an der Universität Ulm - Alemanha, onde é apresentado um método inovador de realizar medidas de espectroscopia de reflectância no visível e infravermelho próximo independente da distância.

Palavras-chave: Espectroscopia; Biofotônica; Esfera integradora; Propriedades ópticas; Ângulo de tipologia individual, Fototipos.

Optical characterization of highly turbid samples in the visible and near infrared spectra

ABSTRACT

High melanin concentrations in dark skins can negatively affect results in light-based diagnostics and treatments. The optical properties of dark skins are known in the literature, but until now, there has not been a correlation between optical properties and skin phototype through a reliable and reproducible classification. The individual typology angle (ITA) was developed in the 90's to classify the skin phenotype by using colorimetric measurements with calibrated equipment. ITA is directly related to the chemical constitutive skin pigmentation and can be used as a reliable method of skin categorization. In this study, different ex-vivo skin phototypes were optically characterized, evaluating the absorption, scattering and effective attenuation coefficient, optical depth penetration and albedo. Each of these optical parameters has relevance in biophotonics applications in health sciences. To measure these properties, 3D-printed integrating spheres system was manufactured, characterized and validated. The optical results indicate the existence of a high correlation between ITA and the optical properties of skins with different phototypes. The absorption coefficient and effective attenuation increase with the decrease of ITA, that is, dark skin absorbs more light. On the other hand, optical penetration and albedo is higher for high ITA values. The scattering coefficient had lower dependence on the skin phototypes. With the experimental data of the absorption coefficient, it was possible to determine an experimental model to estimate the absorption coefficient using only the ITA colorimetric parameters, opening new opportunities for corrections in optical devices such as pulse oximeters, smartwatches, photoacoustic oximetry, and others. Finally, a work developed during the exchange in the Institut für Lasertechnologien in der Medizin an der Universität Ulm - Germany is presented, where an innovative method of carrying out VIS-NIR reflectance spectroscopy measurements regardless of distance is presented.

Keywords: Spectroscopy; Biophotonics; Integrating sphere; Optical properties; Individual typology angle; Skin phototypes.

LIST OF FIGURES

LIST OF TABLES

SUMMARY

Chapter 1: General Introduction

Biophotonics is an emerging and multidisciplinary research field, which can combine light-based technologies to the life sciences, biology, medicine, pharmaceutical science, environmental science, and agriculture [1]–[3]. The advantage of the biophotonics in the medical sciences with visible (VIS) and near infrared (NIR) light lies on a non-invasive spatial and temporal high-resolution method for therapeutic and diagnostic applications, performing from nanoscales molecules [4] up to a few centimeters skin tissues [5], and making possible to evaluate femtoseconds events [6] or even a day time-lapse [7], covering more than ~20 orders of magnitude in the time dimension and ~6 orders in spatial dimension.

In the next introductory sections, several applications of biophotonics on medicine will be shown, the interactions mechanisms between light and biological tissue will be discussed in detail, as well as the limitations of skin phototypes in medical optics and how the present study intends to improve the research field.

Biomedical optics on human health

It is reported in the literature considerable VIS-NIR light-based clinical procedures to improve the human health. It goes from laser surgery, light-activated therapies, optical diagnostics and imaging, imaging in surgery and therapies and new trends on optical technologies. Several applications are shown as follows.

In laser surgery, it can be used for; photocoagulation in retina [8], reshape the cornea [9]–[11], cataract removal [12], removal of lesions [13] and unwanted skin marks [14], [15], acne scars [16], leg veins [17], port-wine stains [18], facial wrinkles [19], skin lighten [20], hair removal [21], prostate hyperplasia [22], lithotripsy [23], angioplasty [24], cardiologic [25] and vascular [26] surgery, laser ablation through fiber-optic catheter [27], dental soft [27] and hard [28] tissue, oral cavity [29], [30], larynx carcinoma surgery [31], necrosis of small tumor metastases [32], palliation of advanced esophageal cancers [33] and bronchoscopy resection [34].

Light-activated therapies are applied in phototherapy for neonatal Jaundice to prevent several hyperbilirubinemia sequelae (permanent neurological damage) [35], mood disorders like depression [36]–[39] and cognitive alterations due sleep disorder [40], antimicrobial treatment

using blue light for infectious diseases [41], enhancing vaccination [42], optical neuromodulation, photoinduced crosslinking, photodynamic therapy, photothermal therapy and photobiomodulation in wound healing [43], tissue repair and regeneration [44], anti-inflammatory therapies [45], neck pain [46], chronic traumatic brain injury [47].

The optical diagnostics and imaging applications lies in point-of-care diagnostics [48], molecular diagnostics by Raman scattering [49], plasmon resonance [50] and resonant optical cavity sensing [51], diagnostic imaging by standard endoscopy [52], capsule endoscopy [53], ophthalmic imaging [54], optical coherence tomography [55], diffuse optical tomography [56], nonlinear microscopies [57], photoacoustic imaging [58], reflectance confocal microscopy [59]. For imaging surgery and therapy there are endoscopic imaging [60], intraoperative imaging [61], molecular imaging [62], and optical imaging in theragnostic [63].

Some innovative technologies applied to biomedical optics or daily life are also emerging in the recent years, some examples are light-activated nanomedicine [64], optogenetic therapies [65], wearable personal healthcare devices [66], [67], implantable optoelectronics devices [68] and biomaterial photonic devices [69].

These many optical applications on human health are possible due the low optical power demand to generate the desired effect [70]. Optical technologies make possible fast and high-resolution determination of unique processes of molecules, cells and tissue, from morphological, chemical, mechanical and movement features. It is compatible with different optical methods and can be combined with non-optical techniques and advanced technologies to increase performance and deal with a broad range of biomedical challenges [1].

Optical technologies also have practical advantages since they are non-contact, and employing easy signal transmission conductors. The application of light has none or minor side effects, having a wide acceptance among patients [1]. Furthermore, optoelectronic components have become even more compact and less expensive nowadays, which allows the manufacture of fairly priced systems.

Despite all the advantages mentioned before, there are still a wide-open field for improvement on light-based applications on biomedical field. Among them, the melanin high concentration in the epidermal basal layer hinders the optical applications in people with darker skin

phototypes and may leads to an incorrect diagnose. Some reports on literature implies these issues in distinct methods; pulse oximeters [71], brain tissue oximeter [72], optical imaging [73], [74], photoacoustic [75], [76], laser therapies [77], tattoo removal [78], and even the optical sensor on wearable devices [79].

A detailed example of the negative melanin influence on diagnoses can be taken by photoacoustic imaging. In this technique, the higher skin pigmentation attenuates the optical energy and increase the background noise, which decrease the image general resolution and quality in deeper regions [80]–[82]. In these studies, blood vessels could be easily mapped in pale skins, but the high absorption on the surface of darker skins impairing the visualization of underlying blood vessels. This phenomenon happens due to the high absorption of diffused light by the melanin in the skin surface, which is converted into an acoustic noise [83]. Figure 1 shows a representation of the melanin effect on photoacoustic image.

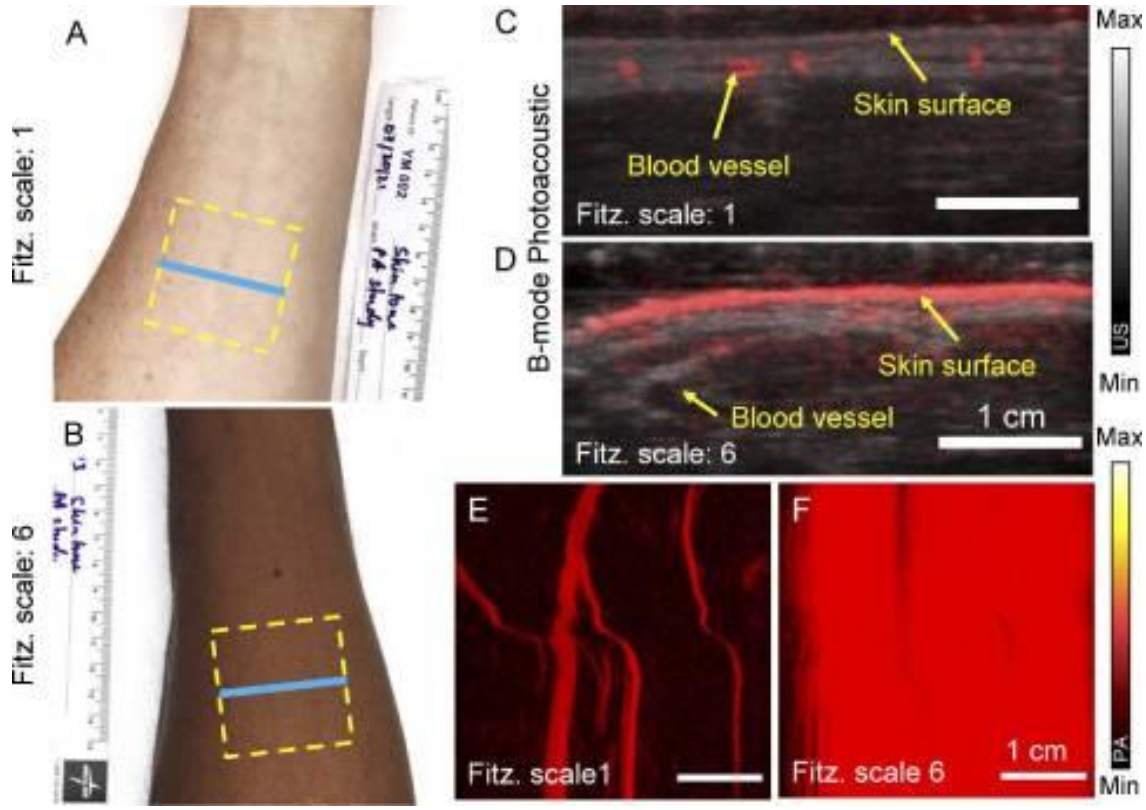

Figure 1 – Volar forearm with A) fair skin (Fitzpatrick scale 1), low melanin concentration and B) dark skin (Fitzpatrick scale 6), higher melanin concentration. In C) the blood vessels could be clearly found in a lighter skin, however D) in the dark skin the opposite was true. As can be seen in E) and F), the visualization becomes even worse in plane images with maximum saturation in Fitz. scale 6. Reference [82].

The lack of knowledge on the skin pigmentation optical influence in applied medical photonics becomes a critical issue when it takes into consideration a daily-basis digital devices like pulse oximeters or smartwatches. In the 2020 Covid-19 world pandemic, clinics and hospitals increased the usage of optical pulse oximeter devices to check blood saturation, due to high hypoxia symptoms in Covid patients [84], [85]. Sjoding et al. [71] reported a study implying a racial bias in this kind of devices. In their study, two large groups (cohorts) of Black patients had nearly three times the frequency of hidden hypoxemia that was not detected by pulse oximetry, unlike White patients. These results suggest that Black patients may have increased risk for hypoxemia in triage due lack of supplemental oxygen in reliance on pulse oximetry, which is a widespread optical device in medical centers.

Thus, one of the main challenges to improve the accuracy on biomedical optics methods, and ensure their applicability in individuals with all kind of skin phototypes is to investigate the effect of pigmentation on light attenuation and penetration. Moreover, as described by Del Bino and Bernerd [86], there is also an appeal for an objective classification of the skin phototypes by a reliable and reproducible method.

Human skin phototypes classification

One of the prior skin classifications were the Fitzpatrick scale, developed by Thomas B. Fitzpatrick of Harvard Medical School in 1975 [87]. It was planned to determine an appropriate ultraviolet A dose for light-skinned persons during psoriasis treatment based on the skin' response to sun exposure, since some patients were having phototoxic reactions during phototherapy [88]. The evaluation method consists of a self-classification questionnaire and clinical evaluation, and is still widely used by physicians during dermatological evaluations since it can be performed through a quickly visual analysis [89]. However, the high subjectivity and low reproductivity of this method is very known in the literature [90], making this method not suitable for accurate photonics corrections on darker-skinned treatments or diagnostics. Besides that, Agbai et al. [91] also reported that "people of color" are categorized into types IV to VI, but their phototypes have an entire broad range colour and do not always match a specific category.

In the last few decades, it has been possible to perform straightforward and accurate measurements to access the human skin colour by using spectroscopy reflectance measures. These methods utilize the Commission Internationale de l'Eclairage (CIE) L*a*b* space to determine skin colour objectively [92]. The L*a*b* color space uses a three-dimensional scale to describe all the colors perceptive by human eyes. The L* axis describes the brightness/luminance and goes from 0 (dark) to 100 (bright). The a* axis describes the green or red colors, and its scales vary from -60 (green) to +60 (red). The last axis, b, also runs between -60 (blue) and +60 (yellow) but with different colors [93]. Figure 2 shows a representation of the CIELAB color space.

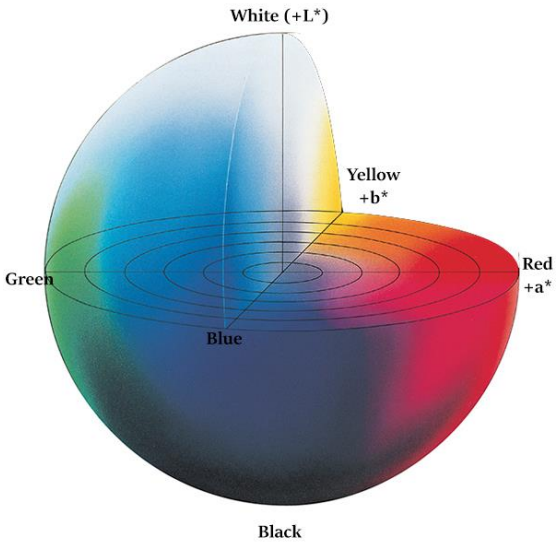

Figure 2 – L*a*b* coordinates representation. Available at [https://sensing.konicaminolta.asia/what-is-cie-1976-lab-color-space/].

The CIELAB coordinates can be directly accessed by a colorimeter, as used in this study, otherwise by spectrometers and a sequence of mathematical equations, see Annex A.

The human skin colour is mainly established by two major biological chromophores: hemoglobin, which provides the skin redness colouration via the vascular microcapillaries, and melanin which provides several degrees of brown pigmentation at the skin surface [5]. It is known that both chromophores have direct correlation with CIELAB coordinates, were a* values are linearly proportional to hemoglobin levels and b* values are related to melanin contents [94].

Alaluf and colleagues [93] assessed skin colour in different ethnicities using CIELAB and the results can be seen in the figure 3. A trend with higher L* and lower b* for lighter-skinned ethnicities could be observed, while the opposite is true for darker-skinned ethnicities, which also have higher a* values.

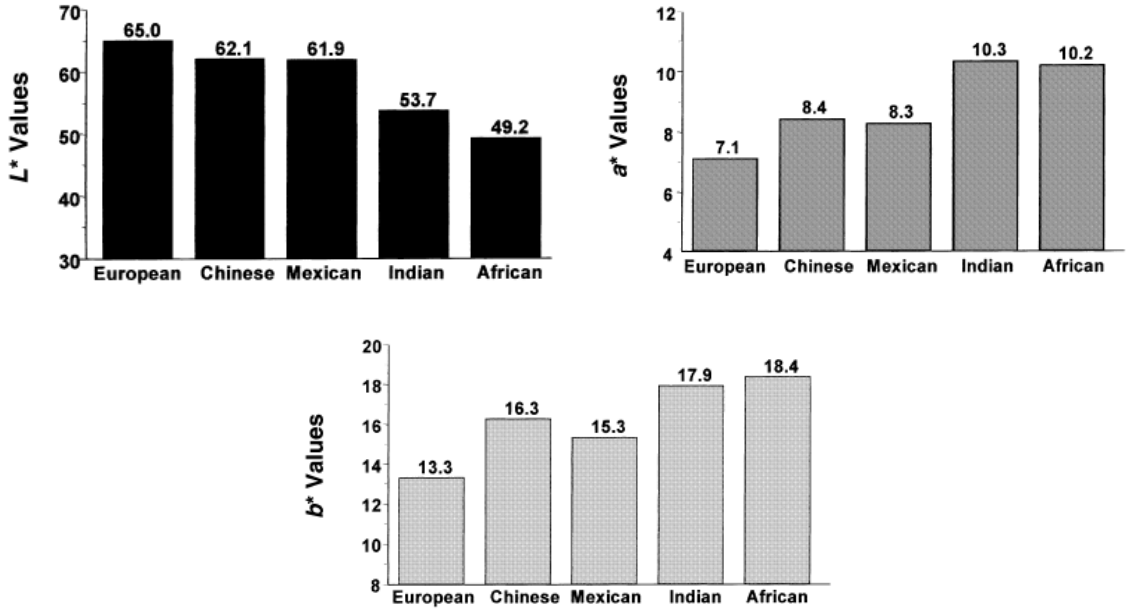

Figure 3 – L*a*b* values from persons across the world. Subjects: 10 Europeans, 8 Chinese, 10 Mexicans, 10 Indians and 10 Africans. All of them were living in South Africa. Reference [93].

Another skin colour categorization method is the individual typology angle (ITA), which also uses the CIELAB colorimetric scale. The ITA was initially proposed by Chardon and collaborators [95] in 1991, as an objective mathematical method of phenotypic classification. ITA is measured in degrees, and can be calculated through equation 1, which uses only the L* and b* colorimetric parameters. The skin type/classification is shown in figure 4 and table 1.

$$ITA = \frac{180}{\pi} \arctan\left(\frac{L^* - 50}{b^*}\right) \quad (1)$$

The individual typology angle may seem as a CIELAB simplified version at first glance, since it uses only L* and b*. However, a large study with 3500 women from France, USA, Mexico, Brazil, Russia, China, Japan, Thailand and India confirmed that ITA have a direct correlation with the constitutive skin pigmentation and is physiologically relevant in all skin population from different geographical areas [86].

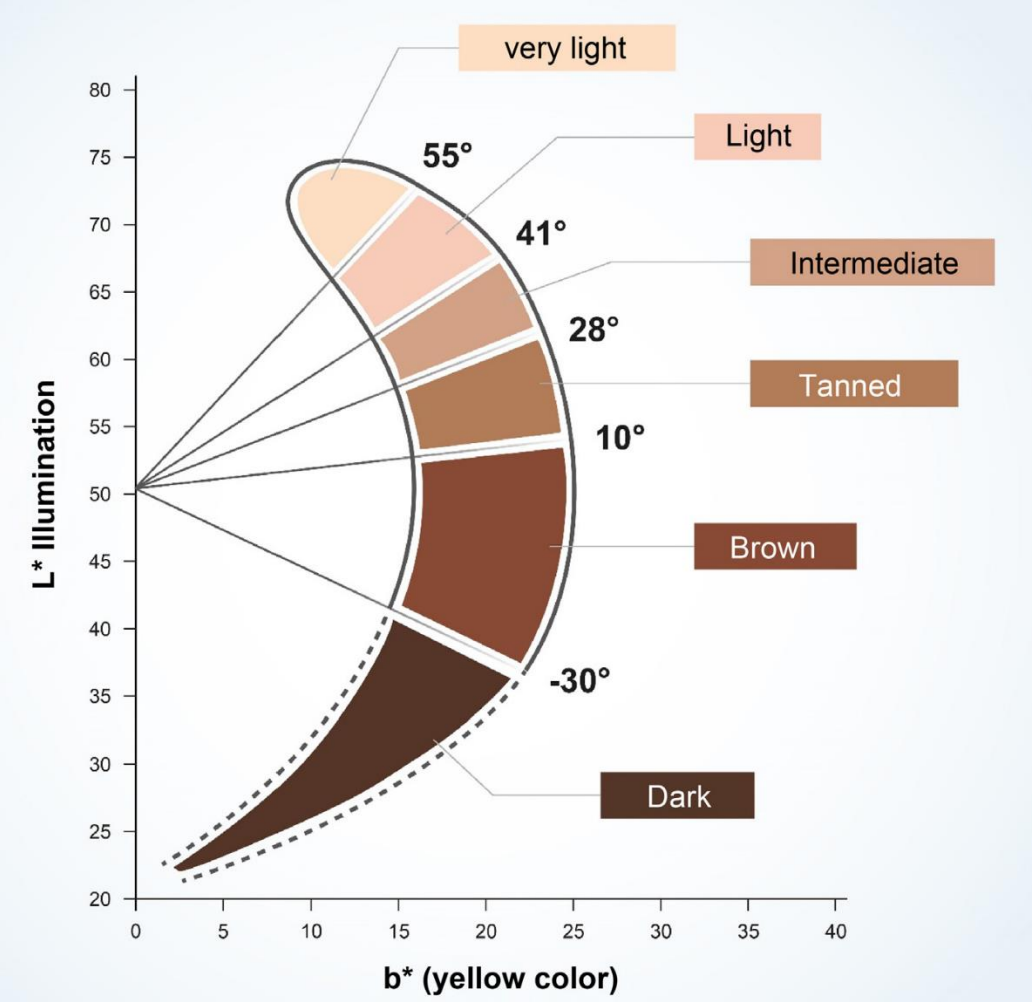

Figure 4 – Individual typology angle diagram and respective colour representation. Note that the ITA is a sequential numerical scale and the color are not unique/static in each classification, pale skins tones are allocated in higher ITA values while very dark skin in the lowest negative values. Figure reference [96].

Table 1 – ITA classification.

ITA (degree)	Typology
ITA > 55º	Very light
41º < ITA < 55º	Light
28º < ITA < 41º	Intermediate
10º < ITA < 28º	Tan
-30º < ITA < 10º	Brown
ITA < -30º	Dark

Zonios et al. [97] in their study found a linear tendency that makes possible to infer a linear correlation between ITA and the melanin concentration (c_m) on the skin surface. Later, Jiang et al. [98] proposed a mathematical formula that summarize these findings, through equation 2.

$$c_m\left(10^{-7}\frac{mmole}{dl}\right) = \left(100 - \frac{100}{48}ITA\right) \quad (2)$$

Since ITA is a reliable and reproducible classification method, several biological studies in the recent years successfully correlate ITA with different chemical constitutive pigmentation and biological effects, such as, eumelanin [99], pheomelanin [99], melanocytes [94], erythemal sensitivity [100], sun exposure [98], hydroxyvitamin D concentrations [101], human skin emissivity [102] and melanocytes ultraviolet-radiation-induced damage [86].

Despite the ITA protagonism in biological and ethnicity studies, until now no study has reported a correlation between the human skin optical properties and ITA for different phototypes. The optical properties of human skin are well known in the literature [5], [98], [103]–[105] for light skins, and in dark-skinned shades [106], [107], but none reproducible phototype classification was performed. These optical properties can be important for correcting optical devices in treatments and diagnoses, or improving existing medical techniques in people with darker skin [108]–[110] and the ITA categorization can be a reliable method to ensure accurate fluence on patients with any skin phototype.

Light interactions on biological skin tissue

The human skin is a complex and heterogeneous biological tissue, where the main chromophores, molecules responsible for pigmentation, are distributed into two main superficial layers; epidermis and dermis [111]–[113]. The inhomogeneous distribution in these chromophores is what produces the diversity in the average optical properties of the human skin tissues for different phototypes.

The epidermis is a blood-free layer with ~100 μm thick, and can be subdivided into two sublayers. The first sub-layer is the stratum corneum, that is known as a non-living epidermis, with ~20 μm thick, and consists basically of dead squamous cells. It is highly keratinized with relatively low water concentrations. The second sublayer is a living epidermis, about ~100 μm thick, and contains mainly melanin, which is produced by the melanocytes [113], [114].

Melanosomes, large melanin particles, having more than 300 nm in diameter, exhibit mainly forward scattering.

On the other hand, dermis is highly vascularized and the main absorbers are blood hemoglobin, carotene, bilirubin and water. It can be subdivided into four layers: papillary dermis (~150 µm thick), upper blood net plexus (~100 µm), reticular dermis (1-4 mm thick) and deep blood net plexus (~100 µm) [113], [114]. The dermal scattering properties are mainly defined by fibrous structure, collagen fibrils packed in collagen bundles, and lamellae structures [115]. A schematic cross-section is shown in figure 5.

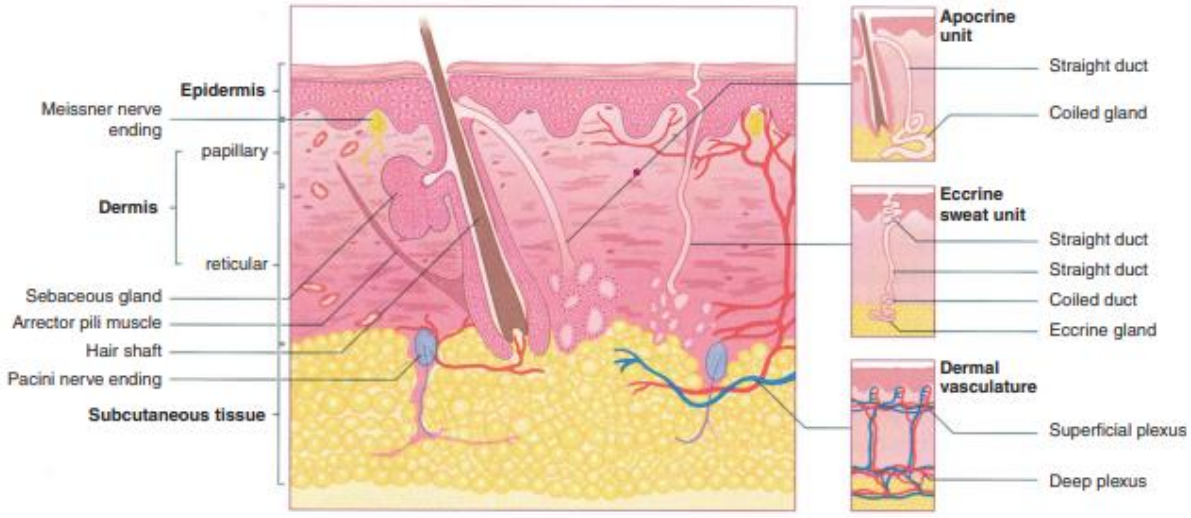

Figure 5 – Schematic cross-section of the human tissue. Reference [114].

The optical properties of the skin tissue are usually characterized by the average absorption (μ_a) and reduced scattering (μ_s') coefficient, which consider the photon absorption or scattering event. The anisotropy factor (g) is also taken into consideration and indicates the preferential light propagation direction in the medium and can be expressed as the average cosine of the scattering angle, as shown in equation 3.

$$g = < \cos(\theta) > \tag{3}$$

Since the absorption and scattering events are probabilistic, it is possible to estimate the photon scattering direction by using Henyey-Greenstein phase function [116], equation (4), which is an important parameter in diffuse light propagation theory.

$$p(\theta) = \frac{1}{4\pi}\frac{1-g^2}{\left(1+g^2-2gcos(\theta)\right)^{\frac{3}{2}}} \quad (4)$$

The scattering properties on human skin are defined by reticular dermis since it is relatively thicker (up to 4 mm) and comparable scattering coefficient from epidermis, while the absorption is mainly defined by hemoglobin bands (oxy- and deoxy-hemoglobin), melanin and water. A light propagation diagram is shown in figure 6.

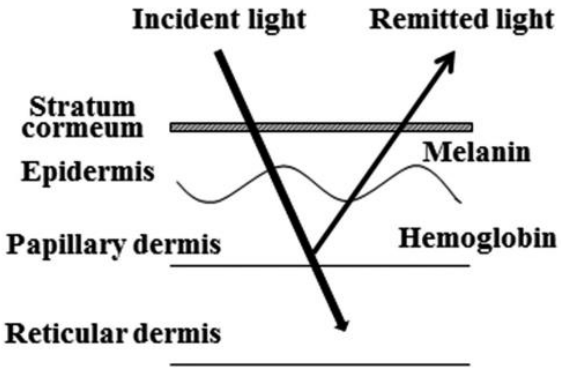

Figure 6 – Light penetration diagram through skin layers. Reference [117].

To calculate μ_a and μ_s, the radiative transport equation (RTE) can be applied, equation (5), and it describes the energy transfer phenomenon by electromagnetic waves.

$$\frac{1}{c}\frac{\partial\varphi(\vec{r},\hat{\Omega},t)}{\partial t} + \hat{\Omega}\cdot\nabla\varphi(\vec{r},\hat{\Omega},t) + \mu_t(\vec{r})\varphi(\vec{r},\hat{\Omega},t) = \mu_s\int P(\hat{\Omega},\hat{\Omega}')\,\varphi(\vec{r},\hat{\Omega},t)d\hat{\Omega}' + q(\vec{r},\hat{\Omega},t) \quad (5)$$

$\varphi(\vec{r},\hat{\Omega},t)$ is the radiance of the incident photons, $\mu_t = \mu_a + \mu_s'$ is the transport coefficient, $P(\hat{\Omega},\hat{\Omega}')$ the phase function, $q(\vec{r},\hat{\Omega},t)$ is the light source signal, and c the light speed.

To solve the equation, it is necessary to provide various information about the sample, such as, refractive index, anisotropic factor, thickness, the diffuse reflectance and transmittance of the samples and some boundaries conditions. The experimental diffuse reflectance and transmittance can be performed using integrating spheres, and the calculation of the optical coefficients can be done using the inverse adding-doubling (IAD) method.

The IAD method was proposed by Dr. Prahl [118] in 1993. The adding-doubling (AD) method can used to calculate the reflectance and transmittance with a known μ_a and μ_s, while the inverse method proposed by Prahl uses the experimental reflectance and transmittance to compute μ_a and μ_s by solving the RTE equation by diffuse theory. The IAD algorithm consider the albedo for all media types, optical depths and phase functions, being useful for all kind of turbid media.

To make possible to IAD solve the RTE, some conditions were taken into consideration, since it could not be solved by direct mathematical methods; time-independent light distribution, homogeneous optical properties*, infinite plane-parallel slab, smooth boundaries, Fresnel's law reflectance, no polarization or fluorescence [118]. Annex B show a general diagram of the IAD algorithm.

*Human skin tissues are not homogenous; however, the algorithm considers the average optical property of the medium. Furthermore, the refractive index and anisotropy factor of the skin layers are similar.

Despite the boundary's conditions, the IAD method gives lots advantages, such as; work on any combination of optical properties, compute glass slides, take into consideration the integrating sphere format and samples thickness to perform light loss corrections, also being a fast and easy to use method [119].

Thesis aim

The thesis aimed to determine the optical properties of ex-vivo human skin samples with distinct phototypes at broadband spectrum in the visible (400-750 nm) and near infrared (750-1300 nm) spectral range, and associate it with the individual typology angle, proposing a correlation between optical and colorimetric properties. A handmade integrating sphere was manufactured and validated in the photobiophysics laboratory to optically analyze the samples by using the IAD method. The optical properties analyzed in this study was; absorption coefficient, scattering coefficient, effective attenuation coefficient, depth penetration and albedo.

Thesis Outline

This thesis consists of four original articles published or submitted under review in international peer review journals. From chapter 2 until chapter 5, it has self-consistent individual introduction, methodology, results and discussions, and conclusions sections, distributed as follows;

Chapter 2: Present the manufacture and characterization of a 3D-printed integrating sphere set-up, which is the essential system used for the optical characterization of the biological tissue in the following sections. This paper was published at Instrumental Science & Technology in 2020.

Chapter 3: Present the optical properties of human skin phototypes and their correlation with individual angle typology. These findings were published at Photobiomodulation, Photomedicine and Laser Surgery in 2023.

Chapter 4: Present the absorption and reduced scattering coefficient estimation in pigmented human skin tissue by experimental colorimetric fitting. These findings were recently submitted to an international peer review journal.

Chapter 5: Present the PhD exchange CAPES-Print collaborative study titled: distance independent total reflectance setup for spectrally resolved determination of optical properties of highly turbid media. It was published in the Applied Optics in 2022.

Chapter 6: Is a general conclusion and future works indications.

Chapter 2: Manufacture and Characterization of a 3D-Printed Integrating Sphere

Abstract: 3D printers are more accessible in both academic and research groups, becoming instruments to facilitate the construction of high-quality scientific equipment for laboratories. In the present study, a 3D printed integrating sphere was validated to acquire diffuse reflectance and transmittance on turbid samples in order to compute optical absorption and reduced scattering through the inverse adding doubling algorithm. The 3D printed integrating sphere was validated in three stages: analysis of the integrating sphere coating reflectance using two possible coating materials (barium sulfate powder and a mixture of barium sulfate and paint), the sphere wall reflectance, and using two accurate optical polyurethane phantoms to measure the absorption and reduced scattering coefficients. The results indicate that the system developed with this methodology shows satisfactory reflectance compared to commercial models and is able to acquire experimental diffuse reflectance and transmittance measurements to compute the optical coefficients of turbid samples due to the use of an inverse adding doubling (IAD) algorithm. However, this system is limited to the region from 500 to 1300 nm due to a decrease in the reflectance of the coating.

Keywords: 1. 3D printed 2. Double integrating sphere 3. Inverse adding-doubling

Based on the manuscript published in Instrumental Science & Technology, 2020

L. B da Cruz Junior and L. Bachmann; “Manufacture and characterization of a 3D-printed integrating sphere”. *Instrum. Sci. Technol., 49(3)*, p.276-287, 2020.

Doi: 10.1080/10739149.2020.1824922.

2.1 - Introduction

Integrating spheres and inverse adding doubling (IAD) algorithm are widely used on optical property acquisitions like absorption (μ_a) and reduced scattering (μ'_s) coefficient and anisotropy factor (g), being considered a standard reference to acquire these optical properties in highly turbid samples [118], [120], [121]. The integrating spheres are applied to collect diffuse reflectance and diffuse transmittance and IAD algorithm applied to acquire the absorption and reduced scattering coefficient using integrating sphere experimental data.

Nowadays, to obtain an integrating sphere is not difficult and may be purchased on websites of optical equipment industries. However, despite the ease of location on the market, an economic factor may limit their acquisition, especially in new research groups that have limited resources, or even to be used as didactic instrumentation in classrooms.

An affordable option is using 3D printers for equipment manufacture. Several articles have previously been reported using 3D printers to develop high-quality scientific equipment for laboratories, such as holders [122], lab jacks[122], choppers[122] micromanipulators[123] and syringe pumps [124]. More recently 3D printers have been used to print integrating spheres [125], [126]. Although 3D printed integrating spheres have been previously reported in the literature, there is limited information on the validation of the coating and reflectance of the assembled sphere to be used with the IAD algorithm for the acquisition of optical coefficients in highly scattering samples.

The integrating sphere theory assumes that the internal wall has uniform and high diffuse reflectivity. It also requires a small sample port area, compared to the total internal surface area of the integrating sphere, typically less than 4% [127], and the coating must not display fluorescence. A baffle is also required to avoid direct radiation from being reflected or transmitted from the sample to the detector [128].

The IAD algorithm, combined with the experimental measurements from the integrating sphere setup, is employed to compute μ_a and the μ'_s coefficients of samples in turbid media. Proposed by Dr. Scott Prahl [118], the IAD theory consists in solving the transport equation until the theoretical solution (guided by sample and equipment input parameters) matches the experimental reflected (M_R) and transmitted (M_T) radiation of the sample normalized by the source acquired with integrating sphere system, according to equations (5) and (6):

$$M_R = r_{std}\left(\frac{R_{sample} - R_{bk}}{R_{source} - R_{bk}}\right) \quad (5)$$

$$M_t = \left(\frac{T_{sample} - T_{bk}}{T_{source} - T_{bk}}\right) \quad (6)$$

where R_{sample} and T_{sample} are the reflectance and transmittance of the sample, respectively; both R_{source} and T_{source} are the source signal through reflectance sphere (reference tiles at the sample port) and transmittance sphere (without the sample), respectively; R_{bk} and T_{bk} are the background noise on each integrating sphere; and r_{std} is the standard calibration reflectance. The experimental data acquisition is shown in Figure 11. A complete manual to apply the IAD algorithm can also be found in the literature [119].

In general, one needs to know the refractive index (n), thickness (d), and the anisotropy factor (g) of the sample. Regarding the integrating spheres, the diameters of the detector, entrance port, sample port and sphere diameter and wall reflectance must be uploaded as well to run the algorithm.

2.2 – Methodology

Integrating sphere manufacture

The set-up of the basic structure for a double integrating sphere system was based on Pickering's work [121]. The design and results are summarized in Figures 7–13. Figure 7A illustrates our sketch with the respective dimensions. The 3D Model was developed by employing the Inventor 2016 software (Autodesk, USA) (Figure 7B) and printed (Figure 7C) on a 3D printer (Core H4, GTMaX3D, Brazil) at our Physics Department (FFCLRP-USP) and used a polylactic acid (PLA) filament for 3D printing as the matrix. The printing process required that the baffle be obtained separately and later attached with epoxy resin glue. The spheres were printed in duplicate to set up a double integrating sphere system. The 3D model for the integrating spheres may be downloaded as supplementary document to this paper.

Figure 7 - A) Integrating sphere sketch with its respective dimensions. 150 mm diameter and 4 mm thickness, input (a) and output (b) ports have 30 mm diameter and are aligned in the same axis. The detector port (c) has 10 mm diameter, and the baffle (d) has 10 mm diameter. B) 3D model. C) Printed assembled integrating spheres and internal view of each part separately with the attached baffle.

Reflectance standard and coating

Based on Knighton's study [129], two different coatings were evaluated: pure barium sulfate powder (JBquímica, Brazil) and a mixture of barium sulfate powder with white paint (Suvinil, Brazil) at 50%, 70%, or 90% (by weight percentage of barium sulfate/paint). Their reflectance was compared with polytetrafluoroethylene (PTFE) reference standard (WS-2, Avantes Inc, USA) as a reflectance ratio (ratio) according to equation (7):

$$r_{coating} = \left(\frac{R_{coating} - R_{bk}}{R_{PTFE} - R_{bk}}\right) \tag{7}$$

where $R_{coating}$ is the reflectance of pure barium sulfate powder or of the mixture of barium sulfate with paint, and R_{PTFE} is the reflectance of $PTFE$, our reference standard.

We computed the average coating reflectance ($\bar{r}_{coating}$) of our homemade coating standard using equation (8), was employed the absolute reflectance average 0.98 of PTFE (provided by Avantes Inc.), from 400 to 1650 nm:

$$\bar{r}_{coating} = 0.98\left(\sum \frac{r_{coating}}{N}\right) \tag{8}$$

where N is the wavelength number measured with the spectrometers to cover the spectral range. The spectral range was limited from 500 to 1300 nm, due to reduction of reflectance below 500 nm and above 1300 nm. More details are described in the results section.

Owing to its higher reflectance, pure barium sulfate powder (without paint) was chosen as coating in the system (Figure 12). The internal walls of the spheres were coated with a flat matte white spray paint (Colorgin, Brazil), which served as glue, and deposited the barium sulfate powder on these walls. It was also used a spongy textured object to attach the powder to the surface and to increase its durability. Fabric or any other soft material can be employed in this last step. Figure 8 shows a diagram of the coating steps.

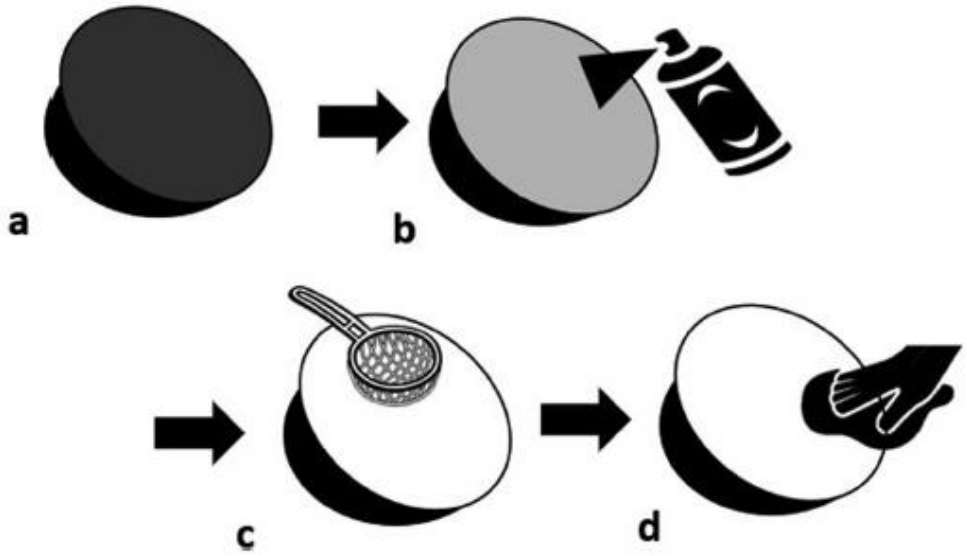

Figure 8 - Schematic diagram of coating process for (a) a raw printed integrating sphere. (b) Use of white spray paint as a clue to attach the barium sulfate coating powder at (c). (d) A fabric is used to press the powder on the wall to homogenize the surface. Processes (c) and (d) were repeated until the sphere wall is fully covered.

Wall reflectance

After its internal wall was coated, it is possible to measure the wall reflectance (r_w) of the final assembled system, according to equation (9), which is an approximation presented by Moffitt [130] to access r_w:

$$r_w = 1 - \frac{A_s}{A}\left(\frac{R_0^{diffuse}}{R_{std}^{diffuse} - R_0^{diffuse}}\right) \quad (9)$$

Equation (9) indicates that r_w is adjusted by the sample port area A_s and to the total internal area of the sphere A and the ratio between the amount of light that remains in the system without $R_0^{diffuse}$ and with $R_{std}^{diffuse}$ a port cover. To measure $R_{std}^{diffuse}$, a coated port cover is used with barium sulfate to close the sample port entrance as shown in Figures 9A and 9B. For $R_0^{diffuse}$, the sample port must be free. This parameter helped to evaluate the system but it is also a mandatory correction parameter for the IAD algorithm.

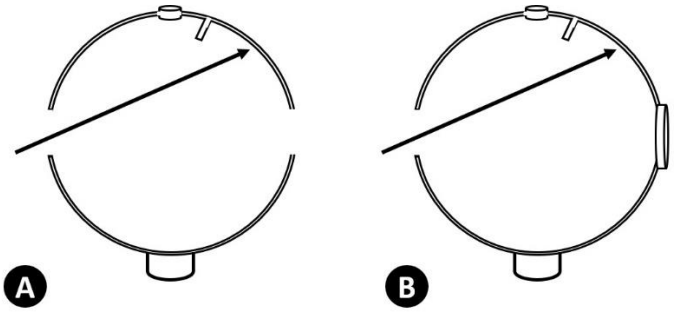

Figure 9 - In A) it is possible to obtain $R_0^{diffuse}$ by using an empty output port. B) to obtain $R_{std}^{diffuse}$, we close the output port by using our homemade barium sulfate standard.

Experimental set-up

Figure 10 shows the schematic diagram of the experimental system. A SLS201 source (Thorlabs, U.S.A.) was employed with a convergent lens (L) to collimate the light beam. It collected the diffused reflected and transmitted signal with a spectrometer (RPS900-R, International Light) in the visible and near-infrared range (400 to 950 nm), and with a second spectrometer (Avaspec-NIR, Avantes, Netherland) in the near infrared range (950 to 1650 nm). An optical fiber with a cosine corrector on was used on detector ports S1 and S2 and was employed the same spectrometer to measure the reflectance and transmittance signals.

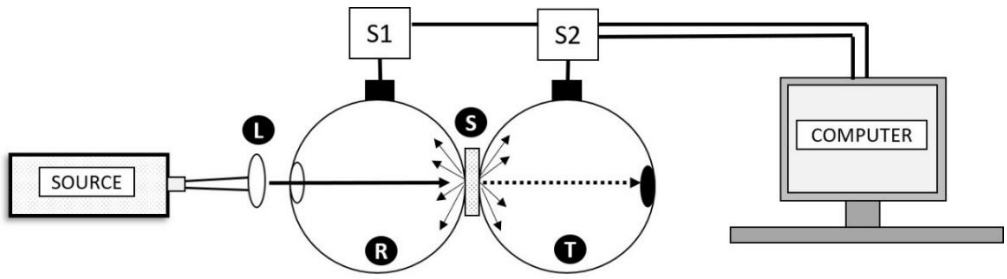

Figure 10 - Source delivers the beam into a converging lens (L) to collimate the light signal that illuminates the sample (S) placed between the spheres. The reflectance sphere (R) receives the backward radiation, which is detected by a spectrometer (S1). The transmittance sphere (T) collects the forward radiation on the spectrometer (S2).

Figure 11 describes the data acquisition steps using the approach by Pickering [121]: (A) with the sample coupled between the spheres, it is measured the sample diffuse reflectance (R_{sample}) with the detector on S1, and changed to S2 to measure the sample transmittance (T_{sample}); (B) after removing the sample, the transmittance standard (T_{std}) is measured with detector on S2; (C) the reference standard is attached to the sample port of the first sphere to measure the reflectance standard (R_{std}) with the detector on S1; and (D) the entrance port is closed to measure the background noise upon the reflectance (R_{bk}) and transmittance (T_{bk}) spheres.

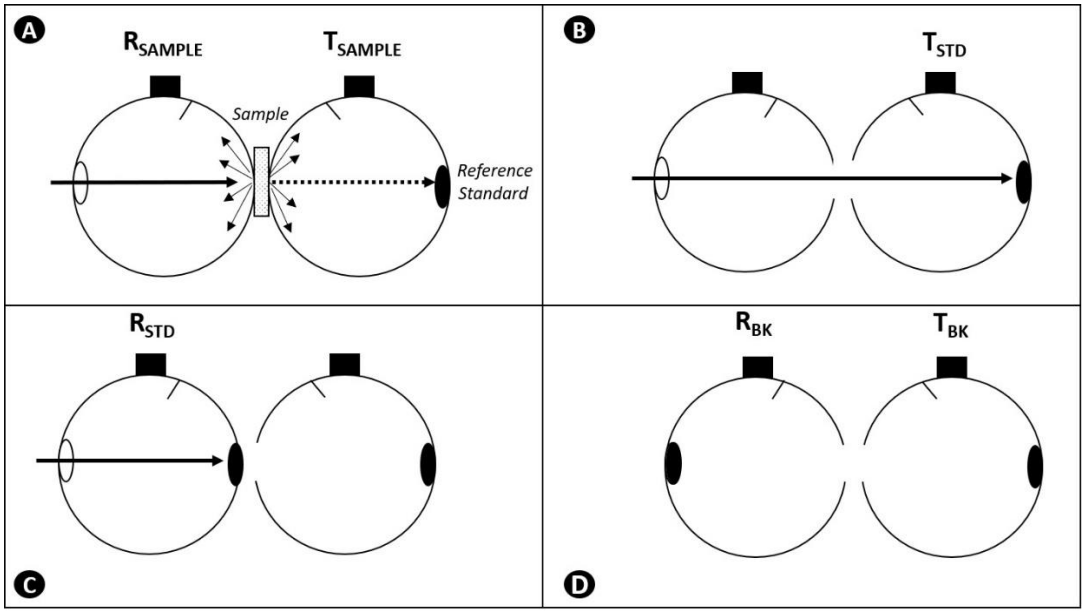

Figure 11 - Experimental scheme for double integrating sphere measurements using the approach by Pickering.[2] R_{SAMPLE} is the raw diffuse reflected light and T_{SAMPLE} is the raw transmitted diffuse light of the sample. T_{STD} and R_{STD} are the source signal on transmittance and reflectance sphere and R_{BK} and T_{BK} are the background noise on each sphere.

Validation samples

To validate the system, two calibrated phantoms were used: Biomimic (INO, Canada) purchased from Institute National Optical (INO), model OP-HBO-C-632-0-0.5-25 (batch number B0654) and OP-HBO-C-632-1-10 (batch number B0656). The OP-HBO-C-632-0-0.5-25 phantom contain a mixture of polyurethane and titanium oxide, while OP-HBO-C-632-1-10 also contain ink absorber dye to increase absorption. These phantoms are similar to Dayton [131] and Moffitt [132] phantoms in terms of composition and optical properties.

Our phantom has reference values for absorption and reduced scattering coefficient at 630 nm as shown on Table 2 along with our experimental values that were computed by INO using time-resolved transmittance technique [133]. To calculate the optical coefficients of the polyurethane phantoms on IAD, the anisotropy factor g of 0.62 was used for 4.9-mm- thickness and 1.511 as the refractive index, as provided by INO. All measurements were made in triplicate to ensure reproducibility of the experimental validation method.

Table 2 - Experimental and reference values with standard deviation for optical absorption (μ_a) and reduced scattering (μ'_s) coefficients at 630 nm for the calibrated phantoms, OP-HBO-C- 632-0-0.5-25 and OP-HBO-C-632-1-10.

	OP-HBO-C-632-0-0.5-25	
	Experimental	Reference (1% error)
μ_a	0.00526 ± 0.00030	0.00537
μ'_s	2.689 ± 0.062	2.380
	OP-HBO-C-632-1-10	
	Experimental	Reference (1% error)
μ_a	0.109 ± 0.002	0.124
μ'_s	1.231 ± 0.022	1.000

2.3 – Results

Coating reflectance

Figure 12 shows the spectral reflectance of pure barium sulfate and its mixtures with paint from our crafted coating; and integrating sphere r_w of the assembled system. The obtained results show that observed reflectance is close to the value for pure barium sulfate and lower reflectance values for the mixtures. The reflectance for all dropped sharply below 500 nm and above 1300 nm. Small bands near 950 nm were observed due changes in the spectrometer at this range. For the reflectance wall, the average reflectance remained close to 0.90 across the investigated range, but non-reliable ranges below 500 nm and above 1300 nm were ignored.

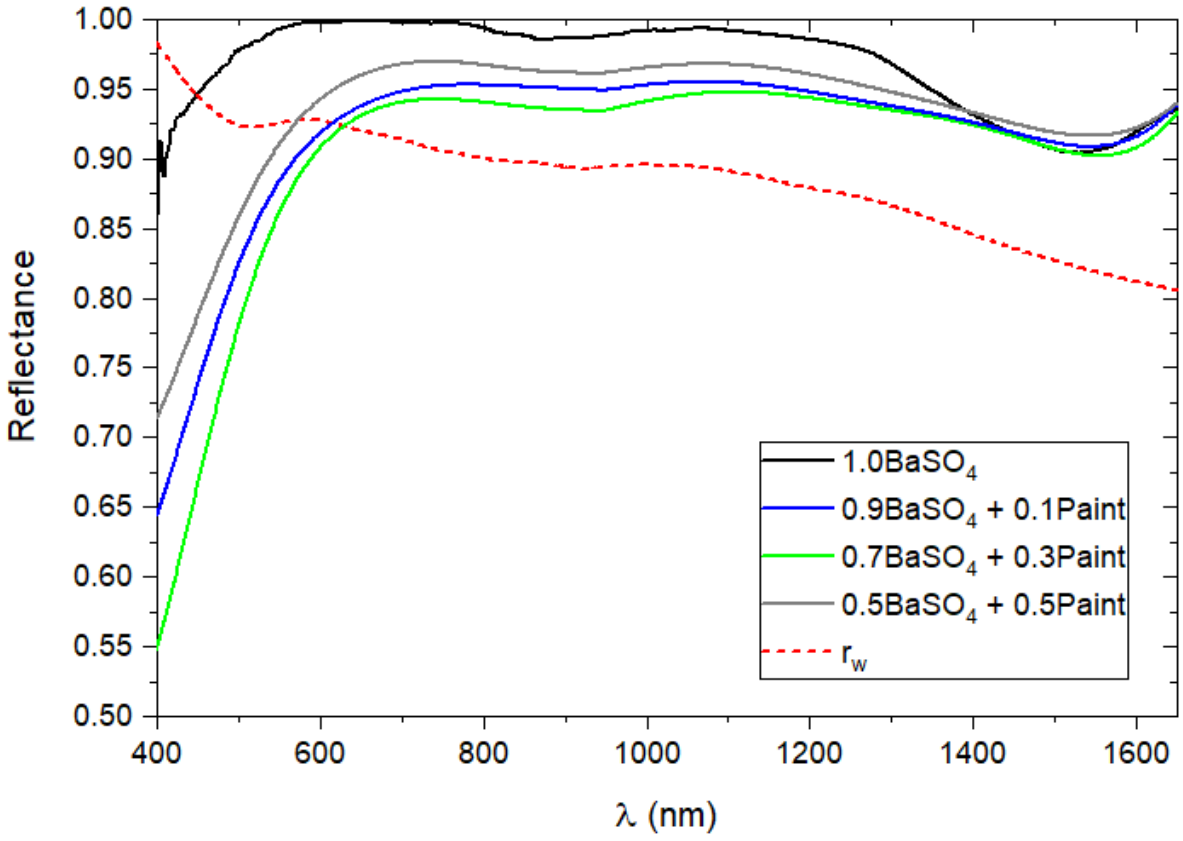

Figure 12 - Reflectance of the crafted coating compared to commercial PTFE and wall reflectance r_w of the sphere from 400 nm to 1650 nm.

By using the experimental measurements for pure barium sulfate reflectance in Figure 12 and applying equation (8), it is possible to compute the average standard coating reflectance $\bar{r}_{coating}$ and the average wall reflectance $\bar{r}_w$: The determined $\bar{r}_{coating}$ of 0.97 and $\bar{r}_w$ of 0.90 parameters were used as correction factors for the IAD algorithm. To measure optical properties with this system reliably, it is recommended that only the optical range from 500 to 1300 nm be used.

Validation phantom optical properties

Figure 13 shows the average absorption and reduced scattering coefficient of the two calibrated phantoms, OP-HBO-C-632-0-0.5-25 and OP-HBO-C- 632-1-10, from 500 to 1300 nm with their respective standard deviations. The acquired values were compared nominally in Table 2 at 630 nm, the unique wavelength that the phantom is calibrated. As expected, the system measured absorption and reduced scattering coefficient are near the reference values. Small standard deviations across the spectrum were observed, with a slight increase in the region close

to 950 nm due to spectrometer changes. The reduced scattering coefficient slowly decreases throughout the higher wavelengths on both samples.

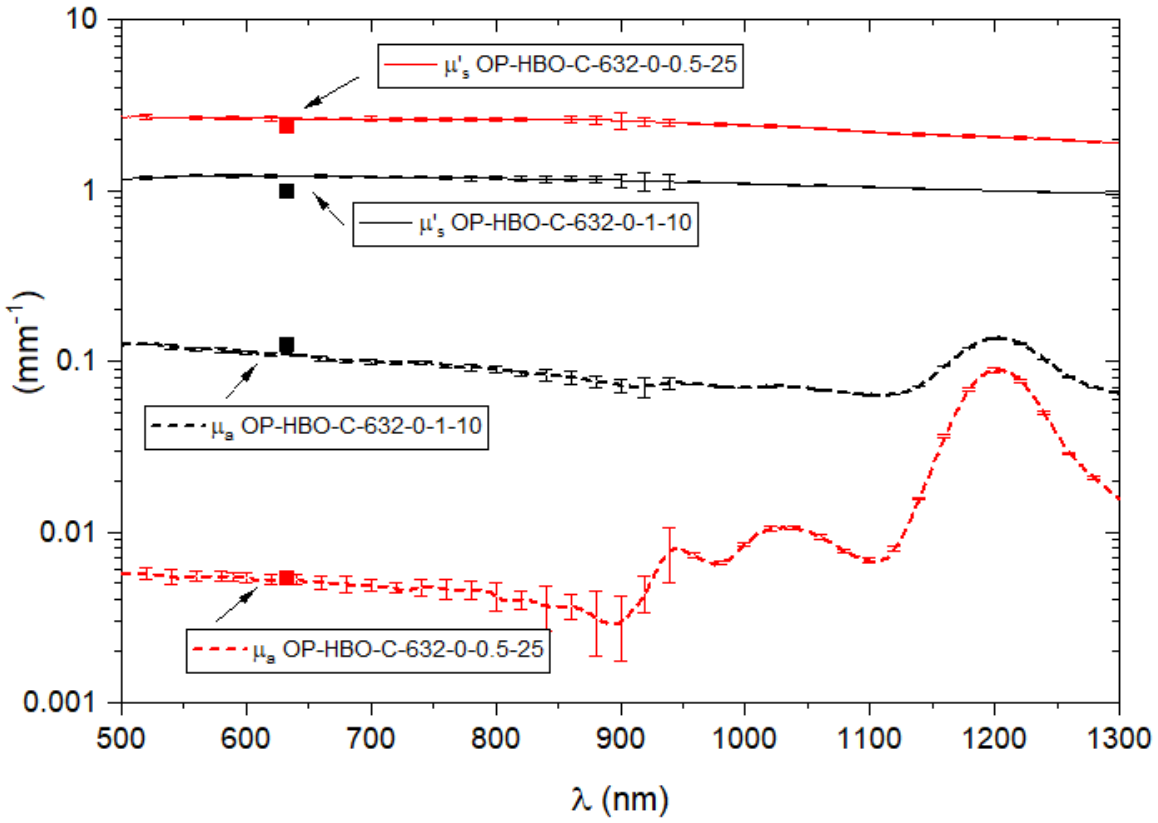

Figure 13 - Optical absorption (μ_a) and reduced scattering (μ'_s) coefficients for the polyurethane phantom measured by our system as compared to a reference value at 630 nm. The red and black dots are the reference values provided by INO and can be checked on table 2.

2.4 – Discussions

Figure 12 shows that the coating reflectance sharply dropped in the blue and in the NIR regions. It is expected a drop in the reflectance below 500 nm [129] due to barium sulfate and at 1450 nm [134] due to water. The reflectance of the paint mixture was lower across the same range. Barium sulfate powder was used as the coating material because of its higher reflectance. However, a mixture of paint and barium sulfate may also be viable in some cases because it has better adhesion to the internal wall and lasts longer without powder loss.

In this system, changes in spectrometers and optical sources elicited by a small break near 950 nm. This discontinuity was not so visible in our case, but in other systems it can be important due to the low signal to noise ratio in some spectral ranges and to the limits of spectrometers or optical sources employed in the system. This break can be worse if sources with different collimation are used: this provokes different radiation losses in the system. The radiation that is not measured in the transmittance and reflectance detectors and which is not computed as radiation loss in the algorithm will result in erroneous calculation of the optical properties. Thus, different systems can generate distinct results, and a step may appear in the spectral data.

The barium sulfate reflectance ratio of our sample was stable; the average value was close to 99% of the PTFE reflectance value (considering the 500 to 1300 nm range and based on the commercial PTFE standard reflectance ($r_{std} = 0.98$). By employing this mean value of measured reflectance, lower values were obtained for the final standard calibration reflectance ($\bar{r}_{coating} = 0.97$). For the wall reflectance, the literature value is $\bar{r}_w = 0.975$ [130]. Herein, the average measured r_w was 0.90. This value was lower because our coating consisted of barium sulfate instead of PTFE in the commercial spheres employed in the literature [130]. Additionally, the barium sulfate coating was handmade, which resulted in some irregularities in the internal wall, which reduced the final reflectance. The sphere sample port corresponded to 1% of the total area of the sphere and agrees with commercial models, which have typical values lower than 4%.

The system was validated by measuring the optical properties of two calibrated phantoms with known values for a specific wavelength. The measured absorption and the reduced scattering coefficients matched the reference value at 630 nm and also agreed with the literature [131], [132]. As shown in Figure 13, infrared absorption bands were observed due polyurethane [135]. The employed system and phantoms was designed to measure and to calibrate samples with high turbidity. The results also show that it is possible to access the absorption and reduced scattering coefficient on samples with high and low absorption. Although we did not calibrate for wavelengths other from 630 nm, bands were not observed near 950, 1050, and 1200 nm on reduced scattering coefficient which shows that the algorithm properly measured the reduced scattering coefficient and consequently the absorption coefficient in that region.

2.5 – Conclusions

Here, we report a reliable 3D-printed integrating sphere system coated with pure barium sulfate powder that was validated by calibrated polyurethane phantoms. The reflectance of the coating and the wall was close to the values obtained for commercial systems. The measured optical coefficients of a calibrated phantom at 630 nm indicate good accuracy of this system and show small standard deviation across the spectrum, implying that the system can be used to acquire absorption and reduced scattering coefficients in turbid samples using the IAD algorithm.

2.6 – Chapter 2 Supplementary Notes

The IAD algorithm used in this study is freely available on Professor Prahl's website [omlc.org] with open-source code. The IAD method solves the radiative transport equation by diffusion approximation, taken into consideration the uniqueness theorem and solutions of RTE based on the conditions of the samples and the experimental source, making it possible to obtain the samples' optical properties. An example of the solution through IAD is presented in Supplementary Figure 1.

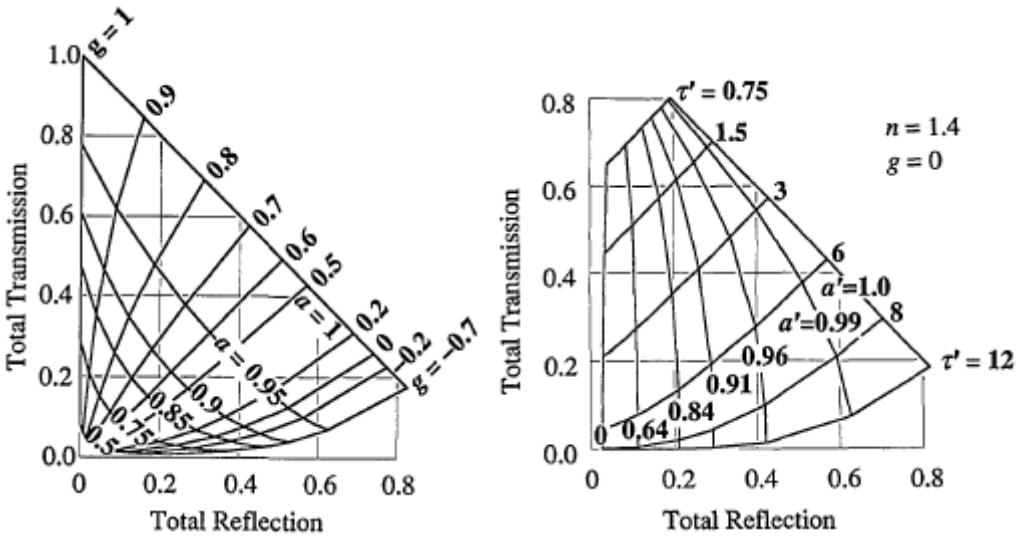

Supplementary Figure 1. Correlation between the samples' reflectance and transmittance with its optical properties. Reference [118].

where τ is called the optical thickness, and can be found through equation s.1:

$$\tau = d(\mu_a + \mu_s) \qquad \text{s. 1}$$

d is the physical thickness of the sample, a is the albedo, and g is the anisotropy factor of the system, both of them were already defined in chapter 2. In the Supplementary Figure 1, it is possible to see how the IAD algorithm correlate the experimental reflectance and transmittance of a sample with its optical properties.

Designing and manufacturing a 3D printed integrating sphere can be a challenging task. These devices are typically made from high-quality, uniform diffusing materials, such as PTFE, and require precise fabrication to ensure accurate measurement results. One of the primary challenges of creating a 3D printed integrating sphere is achieving a uniform and consistent internal surface coating. Any irregularities or inconsistencies in the internal surface of the sphere can cause unwanted light loss, leading to inaccurate measurement results.

Another challenge is ensuring the spherical geometry of the device. The sphere's shape must be precisely controlled to ensure that the light emitted from the source is uniformly distributed inside the sphere. Any deviation from a perfectly spherical shape can result in the light being reflected or absorbed unevenly, leading to measurement errors.

The size of the integrating sphere is critical, as it must be large enough to accommodate the light source being measured while still being small enough to fit into a testing apparatus. Achieving the correct size can be challenging, as any deviation from the desired size can result in measurement errors.

Regarding the validation of the possible coating materials presented in section 2.2 – Reflectance standard and coating. Each possible eligible coating was arranged in small tiles and evaluated using a commercial sphere coated with spectralon. A photo of the assembled system can be seen in Supplementary Figure 2, which may help in better understanding the measurements performed in this study.

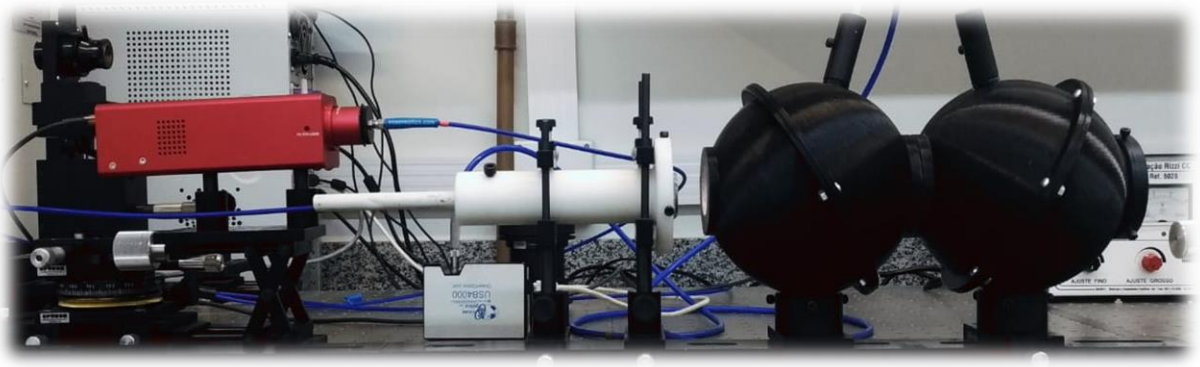

Supplementary Figure 2. 3D printed double-integrating sphere system manufactured and validated in this thesis.

Experimental details: A 2-seconds integration time and an average of 10 measurements were used for the RPS900-R spectrometer, and 2-seconds with an average of 5 measurements were used for the AVASPEC spectrometer. Then, the measurements were performed in triplicate. This experimental design was selected to ensure the lowest noise and that the measurements were as stable as possible.

The light source was left to warm up for at least 30 minutes before each measurement, while the spectrometers performed continuous measurements for the same period to ensure that both were warmed up before performing the experimental measurements.

Alignment was checked before all experimental measurements, ensuring that the system was always concise before each measurement. In addition, verification of beam diameter, lens focus, and other details were always checked.

Overall, designing and manufacturing a 3D printed integrating sphere requires careful consideration of many factors, including the material used, the internal surface finish, the spherical geometry, and the size of the device. Overcoming these challenges can lead to a reliable and cost-effective method of measuring light sources, which can have applications in a wide range of industries, including lighting design, optics, and photography.

Chapter 3: Optical Properties of Human Skin Phototypes and Their Correlation with Individual Angle Typology

Abstract: This study aims to correlate human skin phototypes with complete optical characterization (absorption, scattering, effective attenuation, optical penetration, and albedo coefficients) based on individual typology angle (ITA) values and colorimetric parameters. A colorimeter was used to group twelve ex-vivo fresh human skin samples according to their phototype; the CIELAB color scale and ITA values were employed. An integrating sphere system and the IAD algorithm were applied during optical characterization, conducted from 500 to 1300 nm. On the basis of ITA values and their classification, the skin samples were separated into six groups: two intermediate, two tan, and two brown. In the visible range, for lower ITA values (darker skins), the parameters absorption and effective attenuation coefficient increased, whereas the parameters albedo and depth penetration decreased. In the infrared region, all the phototypes had similar parameters. The scattering coefficient was similar for all the samples and did not change with ITA values. ITA analysis, a quantitative method, showed that the human skin tissue optical properties and their pigmentation colors were highly correlated.

Keywords: 1. Individual Typology Angle 2. Optical Characterization 3. Spectroscopy 4. Human Skin

Based on the manuscript under review in Photobiomodulation, Photomedicine and Laser Surgery, 2022

L. B da Cruz Junior, C. E. Girasol, P. S. Coltro, R. R. J. Guirro and L. Bachmann; “Optical Properties of Human Skin Phototypes and their Correlation with Individual Angle Typology”. *Photobiomodulation, Photomedicine and Laser Surgery, 41(4)*, p.175-181, 2023.

Doi:10.1089/photob.2022.0111

3.1 – Introduction

Understanding how light propagates in biological tissues is extremely important for diagnostic and therapeutic methods [15], [136]. This knowledge may improve patients' and physicians' safety and increase comprehension of medical treatments, to help to develop new therapeutic methods [71]. Light propagation in a turbid medium, which is the case of most biological tissues, can be described by radiative transport equation (RTE) [137] or transport equations (TE) [118] through four optical parameters: absorption (μ_a) and scattering (μ_s) coefficients, refractive index (n) and anisotropic factor (g).

Several articles have described the optical characterization of ex-vivo human skin samples [5], [104], [138], [139]; however, most of them have analyzed stored or post-mortem samples between a day and one week after patient's surgery or death. Genina et al.[140] showed that, depending on the storage process, the optical properties may change. In addition, skin phototypes are not usually considered. When skin phototypes are taken into consideration, the Fitzpatrick scale is often used to categorize the samples according to melanin response to sunlight. Nevertheless, grouping skins by phototypes in one large batch on the basis of the Fitzpatrick scale could induce a subjective evaluation [90]. Indeed, other factors can change the tissue optical properties, including age[141], chromophore concentration [5], lesions [142], and exposure to the sun [94].

To reduce subjectivity when grouping human skins by phototypes, the individual typology angle (ITA) can be employed. Chardon [95] initially proposed using ITA to establish skin color categories by applying the L*a*b* scale measured through a spectrometer or colorimeter. Bino's study [86] showed that ITA is directly correlated with constitutive skin pigmentation, and Zonios [97] found a linear relationship between ITA and melanin concentration. However, no relationship with optical properties has been described so far.

There are several medical and technological applications where knowledge about the optical information of different skin phototypes can be relevant for improving treatment and device sensitivity. Some examples include tattoo removal [15], and low-level laser therapy [136]. Recently, Sjoding et al. [71] suggested that pulse oximeter devices could lead to errors and be less accurate for people with darker skin pigmentation. Therefore, a quantitative and

reproductive method is needed for better understanding how skin phototypes influence photonic procedures. In this sense, this study aims to correlate the skin phototype with the respective optical properties in fresh ex-vivo samples.

3.2 – Material and Methods

The optical properties of twelve fresh samples of abdominal *ex*-vivo human skin were analyzed within three hours after surgery and separated into six different groups according to their individual typology angle (ITA) values, obtained by colorimetric measurements. All the donors were adult females aged between 36 and 65 years, and the measurements were performed on the skin after cleaning. An integrating sphere system was employed to measure diffuse reflectance and transmittance. Then, the optical absorption (μ_a) and reduced scattering (μ'_s) coefficients were computed by the inverse adding-doubling (IAD) method. By using the experimental absorption and reduced scattering coefficients, the effective attenuation coefficient (μ_{eff}), depth penetration (δ), and albedo (a) of the samples were calculated and correlated with ITA values.

Tissue samples

Tissue samples were obtained in association with the Plastic Surgery Division of Ribeirão Preto Medical School, University of São Paulo, after regular abdominoplasty surgery procedures for improving the body contour. All the procedures were performed according to ethical standards and were approved by the Ethics Committee (ethics appreciation certificate 0630218.2.0000.5440 and approval number 3.275.034).

Human abdominal skin samples were obtained from different donors and grouped into six sets according to their ITA values. There were twelve skin tissue samples, separated into group 1, n = 5, intermediate, ITA = 32.7^o; group 2, n = 2, intermediate, ITA = 29.0^o; group 3, n = 1, tan, ITA = 22.4^o; group 4, n = 2, tan, ITA = 18.4^o; group 5, n = 1, brown, ITA = -4.2^o; and group 6, n = 1, brown, ITA = -13.5^o. All the skin tissue samples can be seen in Figure 14. As a reference, groups 1 and 2 are Fitzpatrick type I or II, groups 3 and 4 are Fitzpatrick type III, group 5 is Fitzpatrick type IV, and group 6 is Fitzpatrick type V; however, there is no direct correlation between the Fitzpatrick scale and ITA values [143].

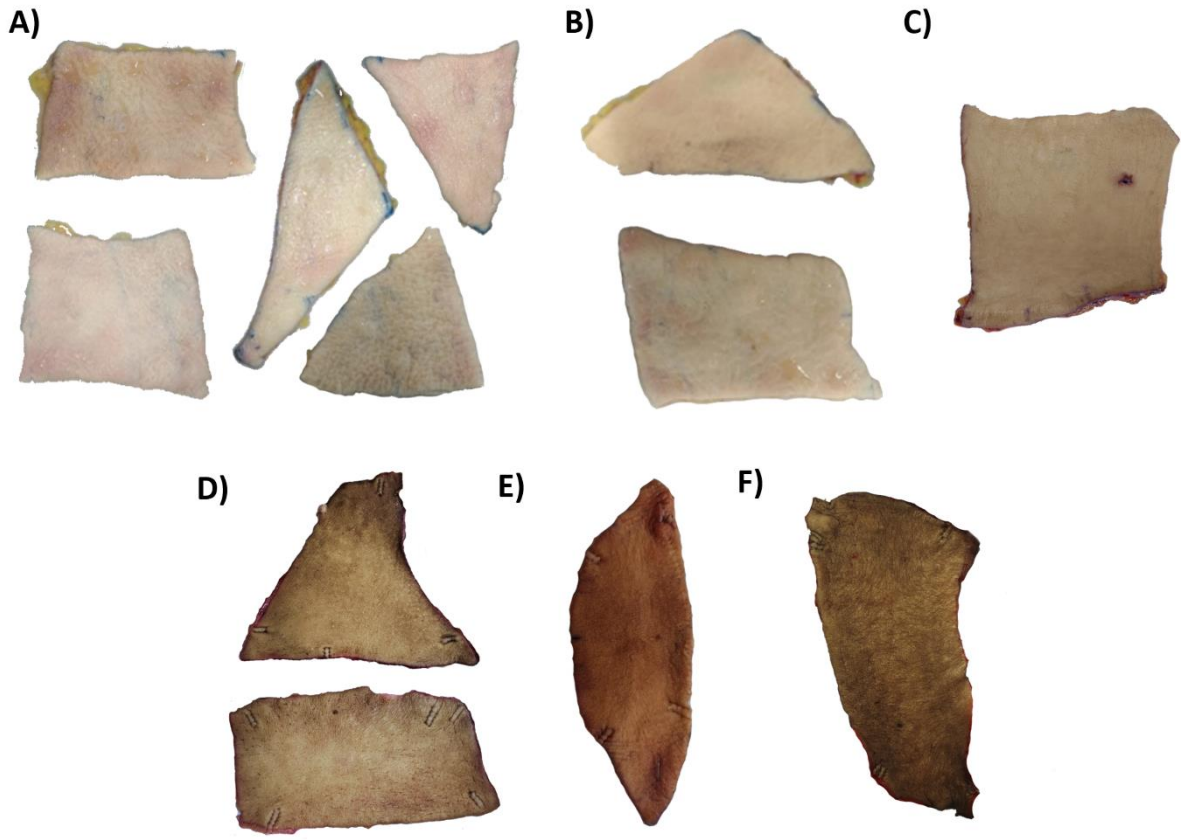

Figure 14: Human skin samples grouped and categorized by ITA: A) group 1 has five samples with mean ITA = 36.7 ± 0.6 and intermediate typology. B) group 2 has two samples, mean ITA = 29.0 ± 0.4, and intermediate typology. C) group 3 has one sample, ITA = 22.4 ± 1.0, and tan typology. D) group 4 has two samples, mean ITA = 18.4 ± 0.8, and tan typology. E) group 5 has one sample, ITA = -4.2 ± 0.9, and brown typology. F) group 6 has one sample, ITA = -13.5 ± 0.7, and brown typology. Only the background was removed.

Sample preparation for the optical measurement consisted of manually removing most of the fat, blood, and fluids from the collected samples, to leave only intact dermis and epidermis. The measurements were performed within three hours after the surgery, so sample freshness was maintained. Thickness ranged from 1.69 to 1.92 mm.

Colorimetry

A colorimeter (DeltaVista450G, Delta Color, Brazil) was used to assess the L*a*b* scale, which uses a three-dimensional scale to describe all the colors perceived by human eyes. L* describes brightness/luminance, while a* describes green and red colors, and b* is related to blue and yellow colors. Measurements were carried out in triplicate; only the average was

considered. Experimental values were used in Equation (10) to compute ITA and skin typology. To avoid experimental errors, a recalibration routine was performed before each measurement.

$$ITA = \frac{180}{\pi} \arctan\left(\frac{L^* - 50}{b^*}\right) \quad (10)$$

ITA, measured in degrees, was used to analyze sample pigmentation[16] and classification was as follows: higher than 55º = very light, 55º to 41º = light, 41º to 28º = intermediate, 28º to 10º = tan, 10º to -30º = brown, and lower than -30º = dark [86], [95].

Optical system and data acquisition

3D-printed double integrating spheres with sphere diameter of 150 mm, input and sample port of 35-mm, detector port and baffle of 10 mm, and barium sulfate as internal coating were employed. An SLS201 light source (Thorlabs, U.S.A) and two spectrometers – an RPS900-R (International light, USA) for measurements from 500 to 950 nm and an AVASPEC-NIR (Avantes, Netherland) for measurements from 950 to 1300 nm – were used. More details about the manufacturing and validation of this system can be seen in Cruz Junior's study [144].

The IAD algorithm was employed to acquire the optical absorption and reduced scattering coefficients. The IAD method consists in iteratively solving the transport equation for a layered semi-infinite medium with a known refractive index to compute μ_a and μ_s' [118]. Information about the system is also required to compensate for light losses. Three experimental values must be supplied to the algorithm: experimental diffuse reflectance (M_r) and transmittance (M_t), according to Equations (11) and (12), and anisotropy factor (g), as a corrective factor.

$$M_r = R_{std}\left(\frac{R_{sample} - B_k}{R_{source} - B_k}\right) \quad (11)$$

$$M_t = \left(\frac{T_{sample-B_k}}{T_{source} - B_k}\right) \quad (12)$$

where R_{sample} and T_{sample} are the experimental diffuse reflection and transmission of the sample, respectively; R_{source} and T_{source} are the source signal on the reflectance sphere and transmittance sphere, respectively; R_{std} is the standard reference reflectance; and B_k is the background noise. More information about the algorithm and experimental procedure can be

found in the IAD manual provided by Prahl20. For the samples, anisotropy factor $g = 0.9$ and refractive index $n = 1.4$ were employed because these are the most common values for skin tissues [5].

Optical evaluation

To describe a turbid medium optically, the refractive index (n), anisotropy factor (g), absorption (μ_a), and scattering (μ_s) coefficients should be known.

Some properties may also be described as a combination of the previous parameters; for example, the reduced scattering (μ_s') and effective attenuation (μ_{eff}), coefficients, depth penetration (δ), and albedo (a), according to Equations (13)–(16).

$$\mu_s' = (1 - g)\mu_s \tag{13}$$

$$\mu_{eff} = \sqrt{3\mu_a(\mu_s' + \mu_a)} \tag{14}$$

$$\delta = \frac{1}{\mu_{eff}} \tag{15}$$

$$a = \frac{\mu_s'}{\mu_s' + \mu_a} \tag{16}$$

μ_s' considers the average scattering angle ($g = < cos\ \theta >$) as an isotropic correction of μ_s in turbid samples; μ_{eff} regards the absorption and scattering effects that reduce the fluence; δ indicates the depth where the light falls to $1/e$ of its initial value after its first interaction with the medium, where e is the Euler number; and a indicates the portion of the attenuated light that is scattered [5].

Since the scattering coefficient pattern decreases with increasing wavelength, a power law curve can be fitted according to Equation 7.

$$\mu_s' = c_1 \left(\frac{\lambda}{500\ nm}\right)^{-c_2} \tag{17}$$

where c_1 and c_2 are arbitrary model parameters for amplitude and scattering power, respectively, and the function is normalized by a reference wavelength (500 nm).

3.3 – Results and Discussions

Colorimetric measures

The Fitzpatrick scale is a classification system commonly used to categorize skin tones based on their response to sun exposure. On the other hand, ITA is a newer skin tone classification system that takes into account skin color by reliable spectroscopic measures. The ITA system is more comprehensive and accurate in assessing an individual's skin tone, making it a better choice in situations where precise color matching is required, such as in the cosmetic industry, light-based treatments, and optical devices (e.g., optical oximeters). Therefore, the Fitzpatrick scale may be changed to ITA in situations where more detailed and accurate skin tone classification is necessary.

By using the experimental L* and b* values of each sample, we obtained the ITA values through Equation 10 and grouped the samples according to their ITA values. The results can be seen in Table 3.

Table 3: Average and standard deviation for L*a*b color scale, ITA values, and skin classification of the six abdominal skin sample groups.

Group	L*	a*	b*	ITA (degree)	Typology
1	60.7 ± 1.2	3.9 ± 1.0	16.4 ± 2.0	32.7 ± 0.6	Intermediate
2	59.5 ± 0.2	5.0 ± 1.2	17.3 ± 0.5	29.0 ± 0.4	Intermediate
3	56.7 ± 1.0	9.5 ± 0.8	16.3 ± 1.6	22.4 ± 1.0	Tan
4	57.6 ± 1.2	6.1 ± 1.2	22.3 ± 1.8	18.4 ± 0.8	Tan
5	48.5 ± 1.6	8.4 ± 0.3	20.9 ± 0.1	-4.2 ± 0.9	Brown
6	44.8 ± 0.7	10.5 ± 0.5	21.7 ± 0.7	-13.5 ± 0.7	Brown

The L*a*b* results resembled the description presented in Alaluf's study [93]. We observed that skin samples with lighter classification, such as groups 1 and 2, generally had higher L* and lower b*. The inverse was true for darker skin. We also noted that parameter a* gradually increased for darker classifications, except for the sample in group 3, categorized as tan.

Some sample groups appeared to be visually similar in terms of color; however, the ITA measurements showed that the skin samples were different. For instance, group 1, with ITA of 32.7º, and group 2, with ITA of 29.0º, were categorized as intermediate types, but had ΔITA of 3.7º. Group 3, with ITA of 22.4º, and group 4, with ITA of 18.4º, were categorized as tan, but had ΔITA of 4.0º. The opposite happened in samples with distant ITA values but the same classification – group 5, with ITA of -4.2º, and group 6, with ITA of -13.5º, which had ΔITA of 9.3º, but were still the brown type.

Absorption and Reduced Scattering Coefficients

Figure 15 shows the experimental absorption from 500 to 1300 nm and the reduced scattering coefficient wavelength dependence of the skin groups labeled by ITA values. The average values are shown in solid lines, and vertical bars correspond to the standard deviation.

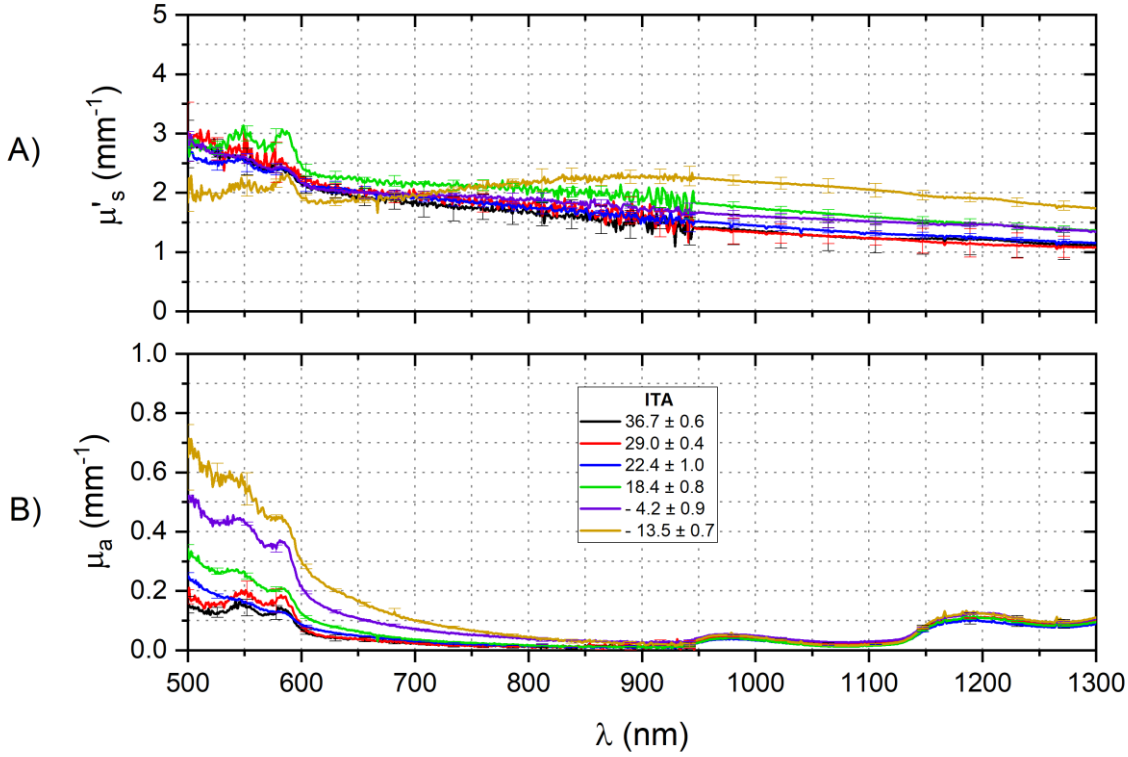

Figure 15: Optical A) reduced scattering (μ'_s) and B) absorption (μ_a) coefficients of the human tissue groups labeled by ITA values. μ'_s has a decreasing pattern through wavelength for all the samples, but the darker sample in group 6 behaves abnormally. μ_a increases when ITA values decrease in the visible range; however, it does not significantly change in the NIR range.

The scattering coefficient decreased in most spectra in Figure 15A, except for ITA = -13.5º. The low μ'_s for ITA = -13.5º from 500 to 600 nm was due to the high absorption in this range, which decreased the albedo see Figure 15B. The latter may not completely converge to the IAD algorithm[5]. However, μ_a in this sample seemed to be reliable.

Scattering was higher at 500 nm (~3 mm^{-1}) and lower at 1300 nm (~1.3 mm^{-1}). Bashkatov [5] described that μ'_s decreases from 500 to 800 nm and stabilizes at higher wavelengths. We observed this behavior for all the skin samples included in this study, but in a lower wavelength range, from 500 to 650 nm. By using Equation 17, we performed a power law fit from the reduced scattering coefficient (Table 4) to compute coefficients c_1 and c_2. In this analysis, we did not consider μ'_s of group 6, with ITA of -13.5 º, due to its abnormal pattern.

Table 4: Power law parameters c_1 and c_2 of the reduced scattering coefficients of our experimental skin data. The R-squared (R^2) parameter is also presented to ensure the fit.

Group	c_1	c_2	$\mathbf{R^2}$
1	2.60 ± 0.01	0.95 ± 0.01	0.96
2	2.82 ± 0.01	1.03 ± 0.01	0.96
3	2.56 ± 0.01	0.83 ± 0.01	0.99
4	2.76 ± 0.01	0.68 ± 0.01	0.95
5	2.54 ± 0.01	0.67 ± 0.01	0.93
6	Disregarded		

The power law fitting data confirmed that all the sample groups had similar μ'_s. All the samples had close amplitude c_1 values; c_2 decreased for darker skins, but they were still close.

Melanin is the main absorbing chromophore in the visible range and produces the skin pigmentation; its absorbance decreases from 500 to 900 nm. Samples in group 1, with the highest ITA values, had the lowest μ_a, but the absorption gradually increased for sample groups with lower ITA values (darker samples). This was expected because, the higher the melanin concentration, the proportionately higher the absorption coefficient [145].

The bands at 540 and 575 nm correspond to oxyhemoglobin bands [146], whereas the bands at 970 and 1200 nm refer to water bands [5], [104], [105]. Our results strongly indicated that these bands did not change according to the ITA values. At 1212 nm, the absorption band may overlap due to fat residues [147], but low concentrations of these residues were present in the samples.

Some authors [94] correlate the skin color by using CIELAB. The a* axis is proportional to the hemoglobin concentration on the blood. This result is expected because the a* scale indicates skin redness. ITA uses only parameters L* and b* to generate its values, so the presence of hemoglobin impacted our results little. Nevertheless, in *in-vivo* samples, the presence of hemoglobin may provide more information and should be taken into consideration. Water is also very abundant in biological samples. It is transparent in the visible range, but absorbs in the infrared region, so it does not change the colorimetric evaluation proposed herein.

Groups 1 and 2, with ITA of 32.7º and 29.0º respectively, had similar μ_a to previously published values [5], [104], [138], [146], [147] obtained for lighter samples. Differences in μ_a values presented here as compared to the literature values could be related to (i) the storage time [140], given that we used fresh samples within three hours after surgery; (ii) the part of the body from which the sample was collected, given that we only analyzed female abdomen tissue; and (iii) the local pigmentation variation due biological individuality. Comparison with dark skin samples in the literature was not possible because we did not find any study that directly correlated the μ_a and μ'_s values of type IV, V, and VI skin with the L*a*b* and ITA color scale. Nevertheless, we found a study with L*a*b* and Fitzpatrick scale in phototypes I, II, III, and IV that indicated higher absorbance correlation for darker skin [148].

We observed lower standard deviation in the absorption coefficient of all the samples from the same group. This was expected because the melanin concentration in samples from the same group should be similar[16]. However, for μ'_s, the standard deviation was relatively larger, which was probably related to the donor's age [141], but not with ITA itself.

Effective attenuation, albedo and depth penetration

By using the experimental absorption and reduced scattering from Figure 15 in Equations 14 and 16, we computed the effective attenuation and albedo of the skin samples Figure 16.

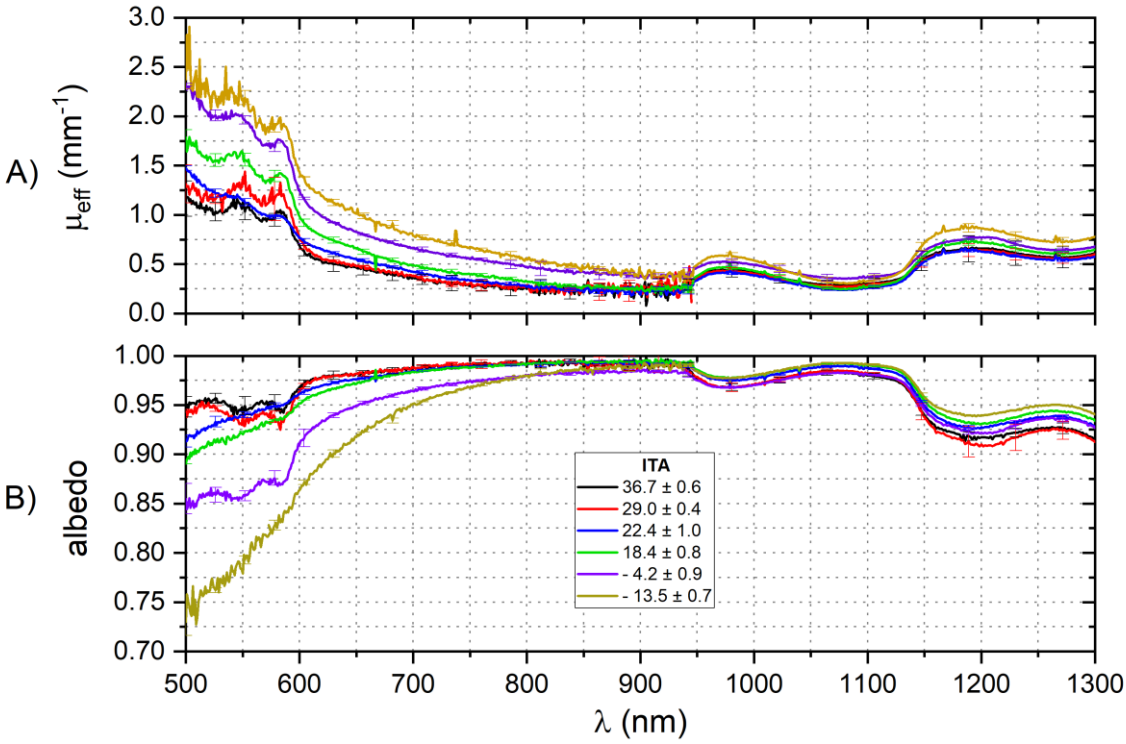

Figure 16 - Skin A) effective attenuation coefficient (μ_{eff}) and B) albedo (a). μ_{eff} increases when ITA decreases, and the inverse is observed for albedo. Prahl indicated that lower albedo ($a > 0.85$) increases the chances of not converging with the IAD algorithm [119].

The effective attenuation coefficient combines scattering and absorption, so it is an asset for estimating how light would be effectively attenuated when interacting with the tissue [149]. This coefficient can also indicate how opaque the medium can be. This coefficient has a similar pattern to the absorption coefficient, but higher values, and it gradually increases for darker skins (lower ITA values) in the visible range.

Figure 16B shows the albedo of the six skin groups. Between 500 and 600 nm, the albedo had the lowest value, and it became even lower for darker skins, ITA = -13.5º, for instance. In the NIR range, the albedo did not significantly change for different sample groups. Although the albedo does not carry crucial information for medical applications, it is relevant in optical analysis. Algorithms that derive from the transport equation such as the IAD and Monte Carlo simulations that use the Radiative Transport Equation assume that the scattering coefficient of the sample is much higher than its absorption, and the albedo indicates how light scattering is

compared to total attenuation ($\mu_a + \mu'_s$). Our results suggested that much darker samples, such as group 6, may not be suitably characterized in the visible region through this methodology, as can be seen in the case of μ'_s in Figure 15A, which showed lower scattering coefficient for this sample in the visible range, but high values for further wavelengths.

The inverse of effective attenuation ($1/\mu_{eff}$) refers to the optical depth penetration [150]. δ indicates how deep light can propagate in human tissue until its initial intensity is reduced to $1/e$ (~36%). Figure 17 shows the experimental depth penetration of the six sample groups.

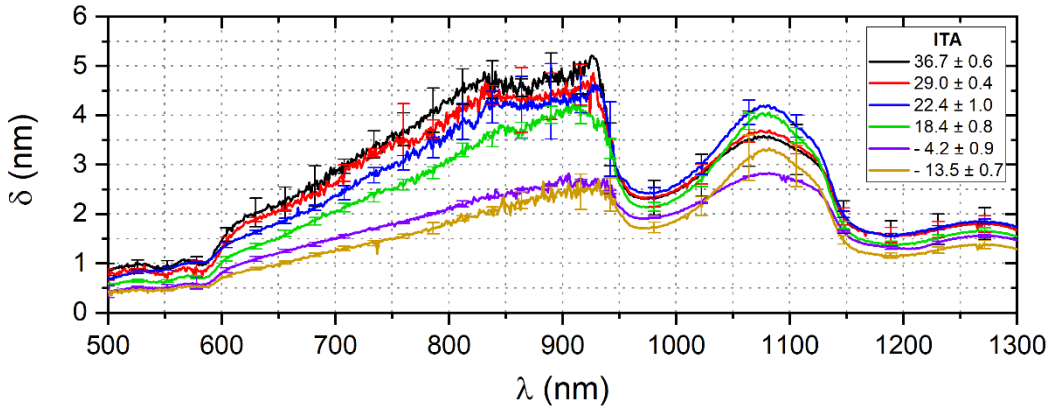

Figure 17 - Human skin depth penetration and their ITA response. Higher ITA values have deeper light penetration, while penetration decreases for lower ITAs.

We observed two high penetration regions. The first ranged from 600 to 900 nm, and the second ranged between 1050 and 1100 nm. Both regions are known as first and second therapeutic windows, respectively, and are useful in optical therapies like PDT [136], [151]. Light penetration was higher in the first therapeutic window region and decreased greatly for darker skins – their maximum was close to 5.2 mm for ITA = 32.66º, 4.9 mm for ITA = 29.05º, 4.6 mm for ITA = 22.42º, 4.2 mm for ITA = 18.36º, 2.8 mm for ITA = -4.15º, and 2.7 for ITA = -13.45º. Bashkatov [5] also reported similar light skin values for Caucasian skin, with maximum penetration depth close to 4.5 mm in the first therapeutic window.

The region with the lowest optical penetration in the visible range lay from 500 to 600 nm, which was due to melanin absorption with the contribution of the hemoglobin bands. In the NIR region, there were two sites of low penetration due to the water bands.

3.4 – Conclusions

We performed an optical characterization on fresh ex-vivo abdominal skin samples. Through the power law coefficient, we observed that the scattering coefficients of the skin groups are similar and do not change with ITA. The absorption and effective attenuation coefficients increase with decreasing ITA, and the inverse is true for albedo and depth penetration. These results are only valid in the visible region because ITA is a classification based on colorimetric parameters. Our findings indicate the importance of considering skin color in optical analysis, especially for the design of photonic treatments and devices.

3.5 – Chapter 3 Supplementary Notes

The discussion about the limitation of the Fitzpatrick scale is well-known and reported in various studies. The limitations of this scale can be observed by considering the following points:

1. Limited range: The scale only classifies skin tone into six categories, which does not accurately represent the wide range of skin tones. *
2. Cultural bias: The scale was developed based on a Caucasian population and may not accurately reflect the skin tones of other races and ethnicities.
3. Inaccurate assessment: The scale is based on a subjective self-assessment, which can lead to inaccurate results.
4. Lack of context: The scale does not take into account factors such as skin type, ethnicity, and environmental factors that can influence skin color.
5. Binary approach: The scale only categorizes skin tone as either "light" or "dark," which can perpetuate harmful stereotypes and reinforce colorism.

* The ITA values are also subdivided into 6 categories, but the categorization is given by numerical values between +75 to -50 (or even lower), where the accuracy of the typology is given by the accuracy of the equipment. The measurements presented in this study were performed with calibrated equipment with accuracy in decimals.

Although the Fitzpatrick scale has these limitations, it is currently used by dermatologists, mainly because it is easy to access (visual inspections and self-report only) and can assess the skin's risk to sun exposure, which is its main use. A list of uses can be seen below:

1. It can help guide the selection of appropriate skin treatments and procedures.
2. It can help determine an individual's risk for skin cancer and sun damage, which is the main purpose of the scale.
3. It can aid in the selection of the most suitable sun protection products for an individual's skin type and color.
4. It can assist in the evaluation in certain skin treatments, such as lightening or brightening agents.
5. It can provide a common language for communication between healthcare professionals and their patients regarding skin color and potential skin issues.

The use of calorimeters in dermatological clinics is important for improving procedures, diagnostics, and photobiomodulation but they are not commonly used in dermatologists' offices. Convincing the medical community to adopt this equipment requires more than just the arguments presented in this article. It also depends on regulation, training, and acceptance. To persuade the community, it is essential to show that more detailed categorization of skin color-tone can leads to better dermatological outcomes.

To facilitate the introduction of these procedures, it is necessary accurate and user-friendly equipment or devices that are suitable for routine use in hospitals and clinics. Ideally, these devices should provide ITA values, which are more informative than just L*a*b* values. To improve correspondence among studies in the areas of photomedicine and dermatology, there should be efforts to ensure accurate colorimetric characterization of skin in a practical and easy manner, similar to the approach taken by our study, to correlate the optical and colorimetric properties for possible future applications in photobiomodulation and photomedicine.

About the skin samples ex-vivo samples used in this study: Skin samples that have been preserved may not accurately reflect their original appearance, as preservation processes can lead to changes in tissue color and discoloration. Formalin fixation, for example, may cause a yellow-brown discoloration in preserved skin samples. This can make color analysis less accurate than when using fresh skin samples that retain their natural color, which can vary based on factors like oxygenation, hydration, and blood flow.

Preservation methods like fixation and staining can cause changes in the color and appearance of skin tissue, leading to inaccurate color measurements and analysis. Fresh skin samples are typically livelier in color than preserved ones, and their true color is preserved, providing a more accurate basis for color analysis.

In this study, unfortunately, there was no characterization of the samples after storage as they were discarded following ethical committee protocols. However, information about changes in optical properties (reflection) due to storage processes is indicated in the text through reference. In this sense, we offer our most sincere apologies for not being able to answer this question in its entirety.

Chapter 4: The Absorption and Reduced Scattering Coefficient Estimation in Pigmented Human Skin Tissue by Experimental Colorimetric Fitting

Abstract: This study aims to estimate the optical properties, absorption (μ_a) and reduced scattering (μ'_s) coefficients, of *ex*-vivo human skin through the individual typology angle (ITA) by only using the skin color parameters. Human skin samples were grouped according to their ITA value, measured using a colorimeter for validation. An integrating sphere and the inverse adding-doubling algorithm was applied to compute the samples μ_a and μ'_s. The μ_a increases with the decreasing of ITA. An axis swap was performed to generate the μ_a versus ITA, for all wavelengths between 500 and 800 nm, with a gap of 10 nm. A linearization was performed and a correlation was found. An equation to fit μ_a based solely on the ITA values was estimated. The μ'_s does not change with ITA, but it could be adjusted through a power law fitting. Both equations have a coefficient of determination R^2 higher than 0.93, indicating a good agreement with our model. An experimental model to estimate the absorption and reduced scattering coefficients of *ex-vivo* human skin through ITA was found. The model has high agreement with the experimental data, with R^2 between 0.932 and 0.997, and these findings may be relevant for photobiomodulation and light treatment applications to estimate the melanin effect on the therapy.

Key words: 1. Spectroscopy. 2. Biophotonics. 3. Colorimetry. 4. Human skin tissue. 5. Individual typology angle.

Based on the manuscript submitted in 2023

L. B da Cruz Junior, C. E. Girasol, P. S. Coltro, R. R. J. Guirro and L. Bachmann; “The Absorption and Reduced Scattering Coefficient Estimation in Pigmented Human Skin Tissue by Experimental Colorimetric Fitting”. Under review.

4.1 – Introduction

Biophotonics devices are an important asset for human health. However, the effect of pigmentation on treatments and diagnoses still needs further investigation. It has been reported that higher concentrations of melanin in the skin may affect optical techniques response, such as: pulse oximeters [71], brain tissue oximeter [72], optical imaging [73], [74], photoacoustic [75], [76], laser therapies [77], tattoo removal [78], and even the optical sensor on wearable devices [79]. As mentioned by Battle Jr and Hobbs [77], despite the limitations, laser procedures in pigmented skin are an open frontier with a growing demand. Thus, a clear understanding of the interaction of light with the human tissue in pigmented skins with a reproducible method is essential.

Currently, the Fitzpatrick color scale is widely used to categorize the skin color. The Fitzpatrick color scale [88] classifies skin tone into 6 scales according to response to sun exposure, where type 1 corresponds to pale white skin while type 6 are darker skin tones. The evaluation method consists of a self-classification questionnaire and clinical evaluation. However, the high subjectivity and low reproducibility of this method is known in the literature [90]. To avoid the limitations of this method, Chardon et al. [95] developed an objective method of categorization by a numerical index, named as individual typology angle (ITA), which is obtained through colorimetric measurements with calibrated equipment.

To calculate the ITA values, a colorimeter or a spectrometer should access the L*a*b* color scale, which uses a three-dimensional color space to describe all colors perceived by the human eye. The L* axis describes luminance/brightness, a* is related to green and red colors, and b* to blue and yellow. Recently, Bino and Bernerd [86] observed that ITA is proportional to the concentration of skin pigments, and Zonios et al. [97] indicated that the concentration of melanin ($C_{melanin}$) is linearly correlated with ITA and can be estimated through equation 18 [98]. Thus, it is possible to describe the constitutive properties of pigments only with the skin's colorimetric response:

$$C_{melanin} = \left(100 - \frac{100}{48}\right) \cdot ITA \tag{18}$$

Recently, it was shown that the optical properties (μ_a and μ'_s) of the skin are related to its color through ITA [152], and this information could be important in biomedical optics applications, as a correction factor for the fluence delivery in all skin phototypes. In this sense, we aim in this study to evaluate how skin color is correlated to its optical properties, suggesting an experimental fitting method to access these optical properties using only the colorimetric response of the ITA, since it is a quantitative and reproducible method which indicates the concentration of pigments present in the skin.

4.2 – Materials and Methods

Colorimetric measures

A colorimeter (Delta Vista 450G, Delta Color, Brazil) was employed to access the L*a*b* color scale of all the samples. The measurement was performed in triplicate and the average was taken into consideration. By using the L* and b* measured values, it is possible to compute the individual typology angle (ITA) of the samples through the equation 19.

$$ITA = \frac{180}{\pi}\arctan\left(\frac{L^* - 50}{b^*}\right) \tag{19}$$

ITA uses CIELAB colorimetric measurements to quantify and categorize the skin color according to its pigmentation as follows: very light > 55º > light > 41º > intermediate > 28º > tan > 10º > brown > -30 > dark [86], [95].

Optical set-up

A 3D-printed integrating sphere system and an RPS900-R spectrometer (International Light Technologies, USA) were employed to acquire the diffuse reflectance and transmittance from the human skin tissue. An SLS201 (Thorlabs, USA) light source was employed, providing a signal between 500 nm and 1300 nm. However, in this study, only the range from 500 nm up to 800 nm was analyzed, since we aim to correlate the samples' visible color and their optical properties. The inverse adding-doubling method was used to compute the optical absorption and reduced scattering coefficient [118] through the experimental diffuse reflectance and transmittance. For detailed information about the system and measurement method, see reference [144]. As described in [152], we used refractive index $n = 1.4$ and anisotropic factor

$g = 0.9$ to compute these optical properties using the IAD algorithm because these are the most common values for skin tissues [5].

Ex-vivo human skin tissue

In this study, twelve ex-vivo human skin tissues were optically analyzed. The samples were divided into six groups according to their ITA values which can be seen in Table 5.

Table 5 - Average and standard deviation L*a*b color scale, ITA values, and skin typology of the six abdominal skin sample groups.

No. Samples	L*	a*	b*	ITA (degree)	Typology
5	60.7 ± 1.2	3.9 ± 1.0	16.4 ± 2.0	32.7 ± 0.6	Intermediate
2	59.5 ± 0.2	5.0 ± 1.2	17.3 ± 0.5	29.0 ± 0.4	Intermediate
1	56.7 ± 1.0	9.5 ± 0.8	16.3 ± 1.6	22.4 ± 1.0	Tan
2	57.6 ± 1.2	6.1 ± 1.2	22.3 ± 1.8	18.4 ± 0.8	Tan
1	48.5 ± 1.6	8.4 ± 0.3	20.9 ± 0.1	-4.2 ± 0.9	Brown
1	44.8 ± 0.7	10.5 ± 0.5	21.7 ± 0.7	-13.5 ± 0.7	Brown

The samples were acquired in collaboration with the Department of Plastic Surgery from Ribeirão Preto Medical School of the University of São Paulo. Sample preparation for the optical measurement consisted of removing fat, blood, and fluids, leaving the dermis and epidermis intact. The measurements were performed within three hours after the surgery, maintaining the freshness of the samples and avoiding storage procedures that may change the optical properties of the samples [140]. The tissue thickness ranged from 1.69 mm up to 1.92 mm, but some fat residues may have been considered in the final thickness of each sample. All procedures were performed according to the ethical standards (ethics appreciation certificate 0630218.2.0000.5440 and approval number 3.275.034).

4.3 – Results and Discussions

Figure 18 shows the skin tissue's absorption and reduced scattering coefficients dependence through wavelength, from 500 nm up to 800 nm. The average values are shown in solid lines and vertical bars correspond to the standard deviation.

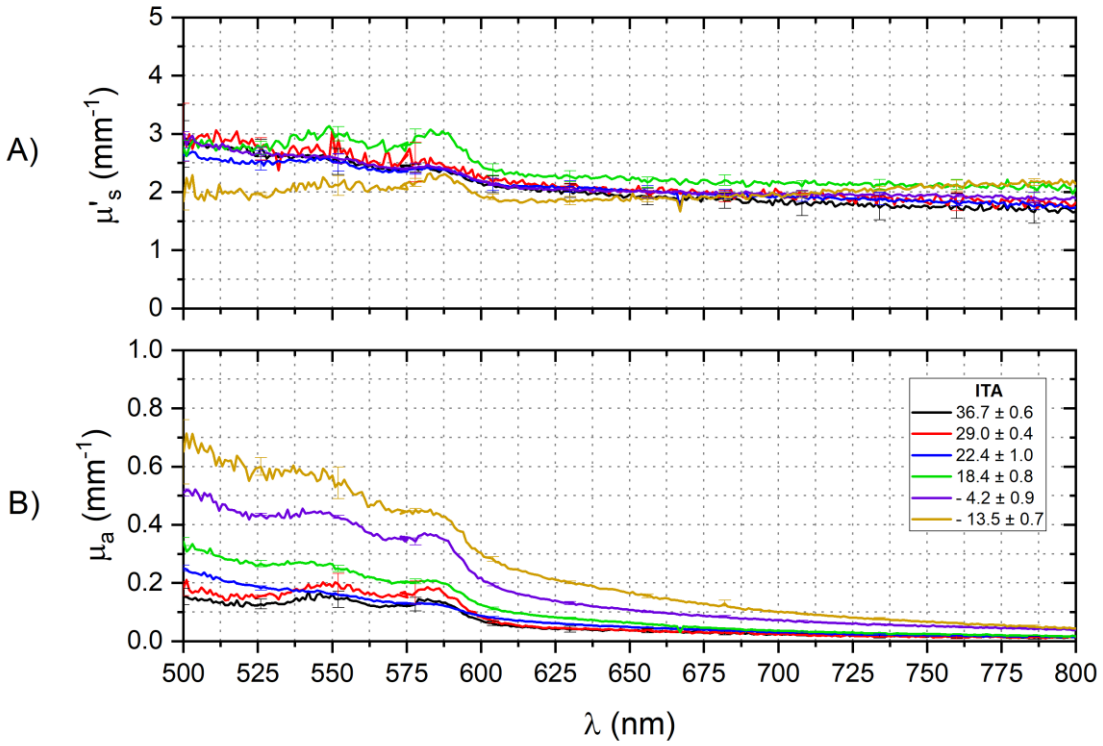

Figure 18 - A) Scattering and B) absorption coefficient of the skin tissue samples, labeled by ITA values. The scattering coefficient does not drastically change with ITA, but the absorption coefficient gradually increases with decreasing ITA values.

The μ'_s in Figure 18 – (A) decreases with increasing wavelength and they remain similar for all groups of samples. Our previous study [152] indicated that scattering did not change with ITA. On the other hand, the same study indicated that μ_a has high dependence with ITA values, were μ_a increases with the decreasing ITA, as can be seen in Figure 18 – (B).

At 540 and 575 nm there are two hemoglobin (Hb) absorption bands [146]. Huang [94] showed that the a* axis of the L*a*b* scale is directly related to the presence of blood, which Hb is the main absorber. Since ITA does not use the a* axis, the traces of Hb will not be considered in

this study. The later analyses were made only for melanin absorption, which is the main pigmentation of the skin. In the near infrared region, human skins have water absorption bands at 970 nm and 1200 nm [5], [139], however, these values do not change for different ITA values [152]. This result was expected because the ITA is a numerical representation of the constitutive pigmentation of the skin (13), being suitable for an analysis in the visible region only.

Using the experimental data from Figure 18 it is possible to make a change of axis from wavelength (λ) to ITA. Figure 19 shows the μ'_s and μ_a dependence as a function of ITA for several wavelengths, from 500 nm to 800 nm with a 10 nm gap and without the Hb range.

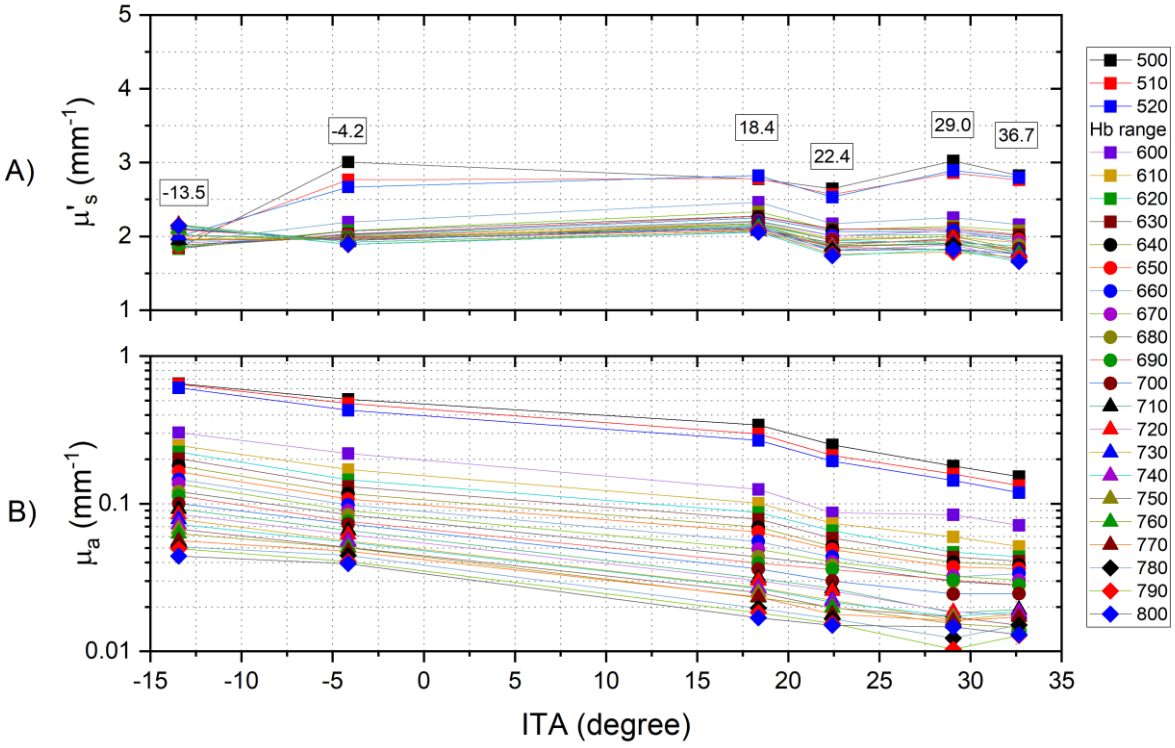

Figure 19 - a) scattering and b) absorption coefficient dependence on ITA values, from 500 nm up to 800 nm, with a 10 nm step. Hemoglobin range (630 until 690 nm) was not taken into consideration.

In Figure 19 – (A), the μ'_s drop abruptly for ITA = -13.45º in initial wavelengths. This result was previously discussed [152], being associated to lower albedo in range, which may not totally converge some data from the IAD method. In this sense, wavelengths at 500, 510 and 520 will be analyzed without ITA = -13.45º. The absorption coefficient in Figure 19 – (B) is in logarithmical scale (log (μ_a)) and shows a possible linear behavior. The Hb bands ranging from

530 up to 590 nm at the μ_a was not taken into consideration, but all the data were considered to μ'_s.

To confirm these possible indications about the behavior in μ'_s and μ_a, a linear fitting on ITA dependence for several wavelengths was made for both of them and the result can be seen in Figure 20. A linear fitting following according to equation 20 and equation 21:

$$\mu'_s = k_1 + k_2 \cdot ITA \tag{20}$$

$$\log(\mu_a) = c_1 + c_2 \cdot ITA \tag{21}$$

were k_1, k_2, c_1 and c_2 are arbitrary model parameters. To ensure the mathematical adequacy, the model adapted μ_a to $\log(\mu_a)$ from the logarithmical scale used in Figure 19.

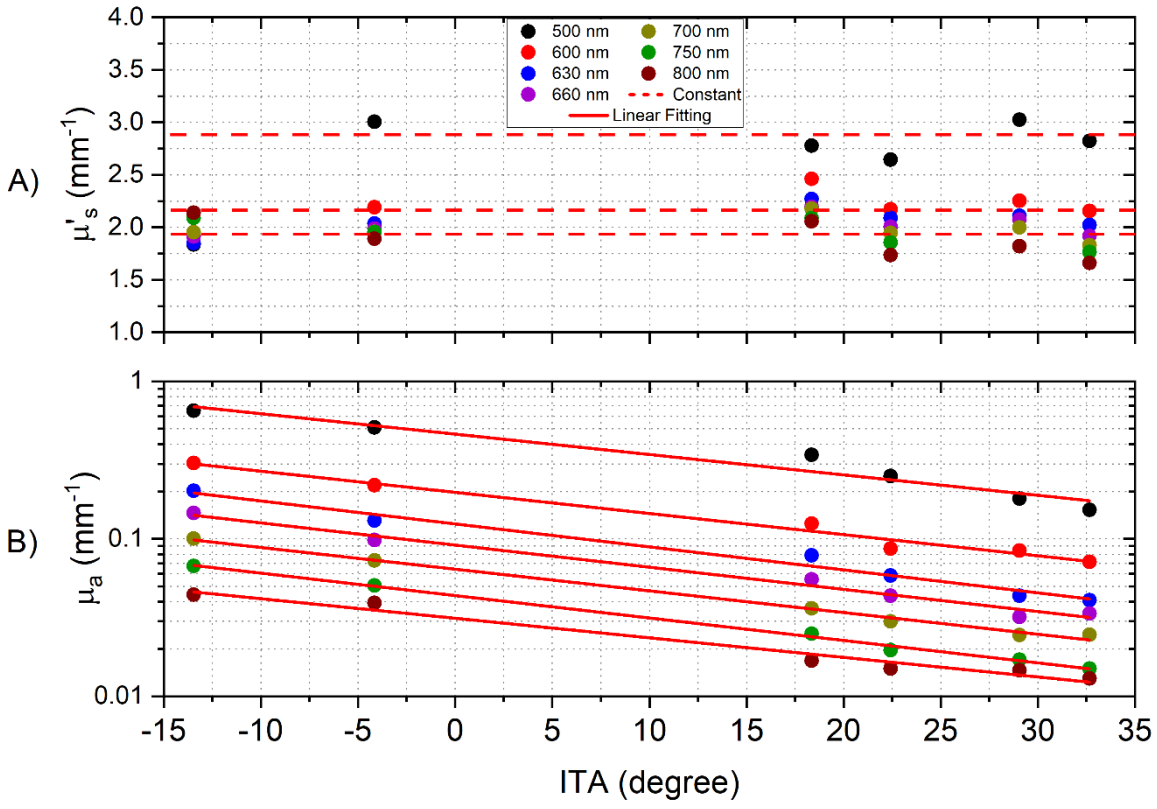

Figure 20 - Linear fitting of the optical parameters at 500, 600, 630, 660, 700, 750 and 800 nm. The scattering coefficient at a) does not significatively chance with ITA, however, the absorption coefficient at b) linearly decrease with the ITA increasing.

As can be seen in Figure 20 – (A), all the μ'_s remained in the vicinity of a constant region instead of a linear profile. This behavior was maintained for all wavelengths between 500 and 800 nm, including the Hb region. On the other hand, the linear fitting was able to successfully fit the absorption coefficient on a logarithmic scale. The linear fitting coefficient can be detailed seen in Figure 21 for μ'_s and Figure 22 for μ_a over the entire spectra. Table 6 also shows the data of k_1, k_2, c_1 and c_2 ranging from 500 up to 800 nm, by 10 nm step.

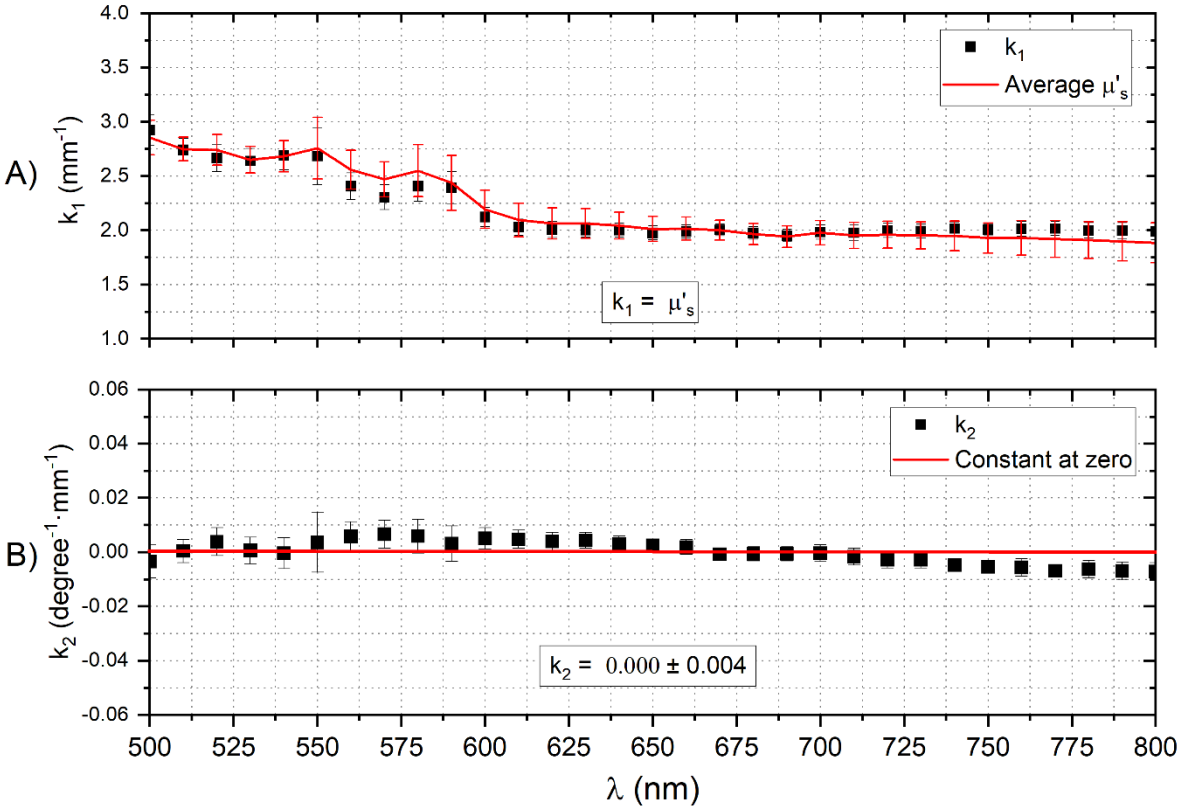

Figure 21 - Linear fitting parameters for the scattering coefficient. The slope term oscillates in the vicinity of zero for all wavelengths, and has mean value of 0.000 ± 0.004. On the other hand, k_1 exhibit values close to the average μ'_s, indicating that we can make the linearization as a constant factor only.

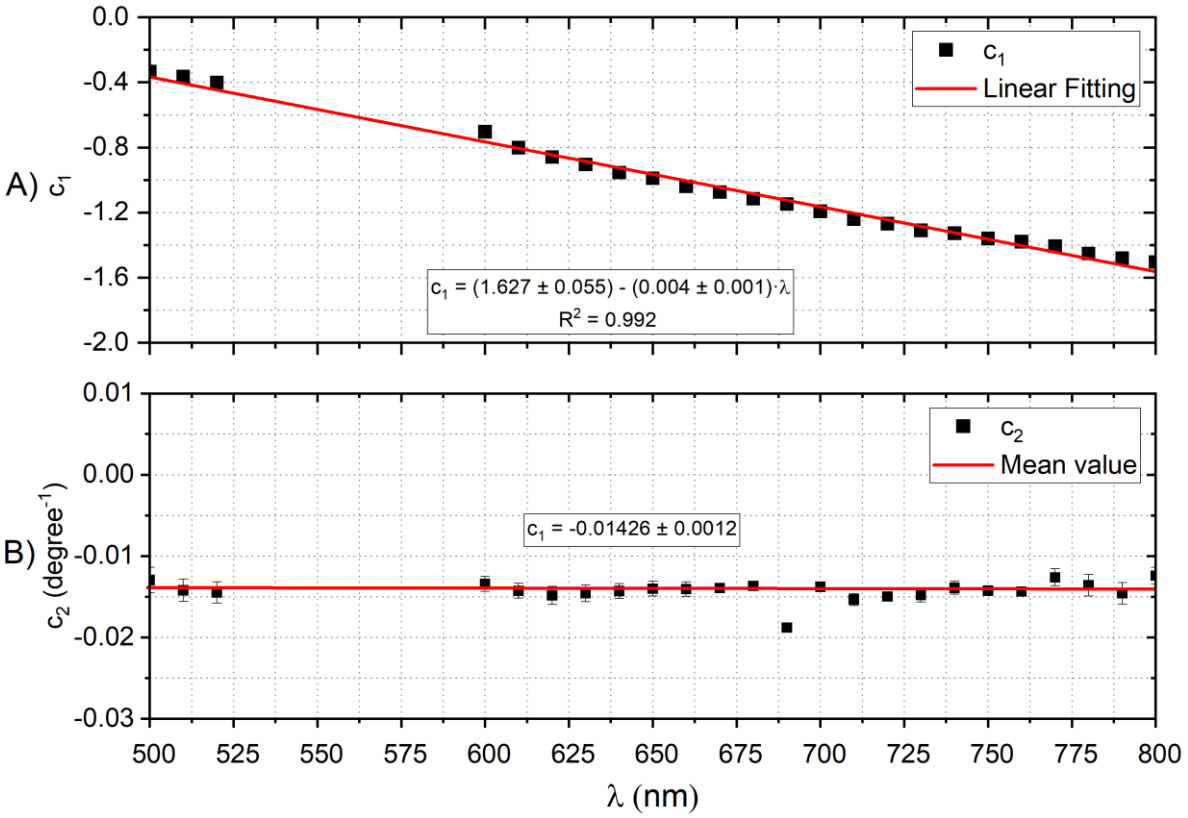

Figure 22 - While μ'_s parameters showed no correlation through ITA, the opposite is true for μ_a. A) the intercept c_1 change linearly according to λ and can be described by the equation 22 with a coefficient of determination $R^2 = 0.99$. B) indicates a constant slope c_2, with mean value -0.014 ± 0.001.

Table 6 - Reference values for k_1 $[mm^{-1}]$, k_2 $[(degree.mm)^{-1}]$, c_1 [dimensionless], c_2 $[degree^{-1}]$ and R-squared of c_2 as function of λ $[nm]$.

λ	k_1	k_2	c_1	c_2	R^2
500	2.924 ± 0.144	-0.004 ± 0.006	-0.334 ± 0.035	-0.013 ± 0.002	0.945
510	2.741 ± 0.102	0.000 ± 0.004	-0.364 ± 0.030	-0.014 ± 0.001	0.965
520	2667 ± 0.124	0.004 ± 0.005	-0.400 ± 0.030	-0.014 ± 0.001	0.965
530	2.639 ± 0.114	0.001 ± 0.005	-	-	-

540	2.689 ± 0.134	0.000 ± 0.006	-	-	-
550	2.684 ± 0.226	0.004 ± 0.011	-	-	-
560	2.405 ± 0.123	0.006 ± 0.005	-	-	-
570	2.304 ± 0.114	0.007 ± 0.005	-	-	-
580	2.406 ± 0.140	0.006 ± 0.006	-	-	-
590	2.391 ± 0.146	0.003 ± 0.006	-	-	-
600	2.122 ± 0.088	0.005 ± 0.003	-0.704 ± 0.020	-0.013 ± 0.001	0.942
610	2.027 ± 0.075	0.005 ± 0.003	-0.801 ± 0.020	-0.014 ± 0.001	0.984
620	2.007 ± 0.073	0.004 ± 0.003	-0.859 ± 0.025	-0.015 ± 0.001	0.978
630	2.002 ± 0.066	0.004 ± 0.003	-0.905 ± 0.023	-0.015 ± 0.001	0.980
640	2.002 ± 0.065	0.003 ± 0.003	-0.954 ± 0.020	-0.014 ± 0.001	0.984
650	1.976 ± 0.063	0.003 ± 0.002	-0.989 ± 0.020	-0.014 ± 0.001	0.983
660	1.989 ± 0.060	0.002 ± 0.003	-1.039 ± 0.020	-0.014 ± 0.001	0.984
670	2.003 ± 0.054	-0.001 ± 0.002	-1.074 ± 0.020	-0.014 ± 0.001	0.983
680	1.976 ± 0.058	-0.001 ± 0.003	-1.115 ± 0.007	-0.014 ± 0.000	0.984
690	1.950 ± 0.058	-0.001 ± 0.003	-1.148 ± 0.013	-0.018 ± 0.001	0.994

700	1.984 ± 0.067	0.000 ± 0.003	-1.192 ± 0.012	-0.014 ± 0.001	0.998
710	1.977 ± 0.069	-0.002 ± 0.003	-1.241 ± 0.016	-0.015 ± 0.001	0.993
720	1.998 ± 0.066	-0.003 ± 0.003	-1.268 ± 0.010	-0.015 ± 0.000	0.994
730	1.992 ± 0.066	-0.003 ± 0.003	-1.310 ± 0.019	-0.015 ± 0.001	0.991
740	2.011 ± 0.060	-0.005 ± 0.000	-1.326 ± 0.018	-0.014 ± 0.001	0.996
750	2.005 ±0.056	-0.005 ± 0.002	-1.360 ± 0.008	-0.014 ± 0.000	0.987
760	2.011 ± 0.070	-0.006 ± 0.003	-1.379 ± 0.009	-0.014 ± 0.000	0.987
770	2.016 ± 0.064	-0.007 ± 0.000	-1.406 ± 0.023	-0.013 ± 0.001	0.997
780	1.998 ± 0.072	-0.006 ± 0.003	-1.451 ± 0.030	-0.014 ± 0.001	0.997
790	1.996 ± 0.073	-0.007 ± 0.003	-1.481 ± 0.030	-0.015 ± 0.001	0.967
800	1.988 ± 0.074	-0.007 ± 0.003	-1.504 ± 0.023	-0.013 ± 0.001	0.963

The k_2 parameter in Figure 21 indicates that the slope term oscillates in the vicinity of zero for all wavelengths, and has mean value of $k_2 = 0.000 \pm 0.004$. On the other hand, k_1 exhibit values close to the average μ'_s, indicating that we can make the linearization as a constant factor only. So, we can simplify equation 20 to $\mu'_s = k_1$, since $k_2 \ll k_1$, confirming that μ'_s has no dependence on ITA for all λ from 500 nm to 800 nm.

While μ'_s parameters showed no correlation through ITA, the opposite is true for μ_a. Figure 22 – (B) indicates a constant value for the fitting coefficient c_2, with mean value -0.014 ± 0.001. However, the intercept c_1 change linearly according to λ and can be described by the equation 23 with a coefficient of determination $R^2 = 0.99$.

$$c_1 = 1.657 - 0.004\lambda \tag{23}$$

It is possible to set up a relationship between the optical coefficients, μ_a and μ'_s, as a function of the ITA. By using equation 21 and applying the exponential on $\log(\mu_a)$ to obtain μ_a we reach at equation 24.

$$\mu_a = 10^{c_1} \cdot 10^{c_2 \cdot ITA} \tag{24}$$

As shown in the previous section, c_2 has a constant value of -0.014, and c_1 changes according to equation 23. These values can be substituted into equation 24, then:

$$\mu_a = 10^{1.657 - 0.004 \cdot \lambda} \cdot 10^{-0.014 \cdot ITA} \tag{25}$$

A readjust in equation 25 can be performed, leading to equation 26:

$$\mu_a = 45.4 \cdot 10^{-0.004 \cdot \lambda} \cdot 10^{-0.014 \cdot ITA} \tag{26}$$

The equation 26 relates μ_a to the ITA values for all λ within the visible range, except to the Hb range. Now it is possible to estimate μ_a on *ex-vivo* human skin solely by their ITA values and choosing the wavelength of interest. The λ is already in nm.

The μ'_s cannot be estimated using the same routine because it does not change according to ITA values. However, is well now by the literature that a general power law fitting (24) describes with a good precision the μ'_s decay through λ by using equation 27:

$$\mu'_s = z_1 \left(\frac{\lambda}{500\ (nm)} \right)^{-z_2} \tag{27}$$

were z_1 and z_2 are amplitude and decay parameters from the power law equation. In this study, a 500 nm was used to normalize the power law equation; it can be chosen randomly but this value is preferred. Using the mean value from all μ'_s, we found the parameter $z_1 = 2.84 \pm 0.04$ and $z_2 = 1.03 \pm 0.06$ with $R^2 = 0.932$. Replacing them in equation 27 makes possible to equation 28 fully describe the decreasing pattern of μ'_s with the increasing of λ.

$$\mu'_s = 2.84 \cdot \left(\frac{\lambda}{500\ (nm)}\right)^{-1.03} \quad (28)$$

By using the ITA presented in this study as reference to equation 26 and 28, an experimental model of μ_a and μ'_s can be estimated and set side by side with the experimental values from Figure 18. The Figure 23 show this comparison.

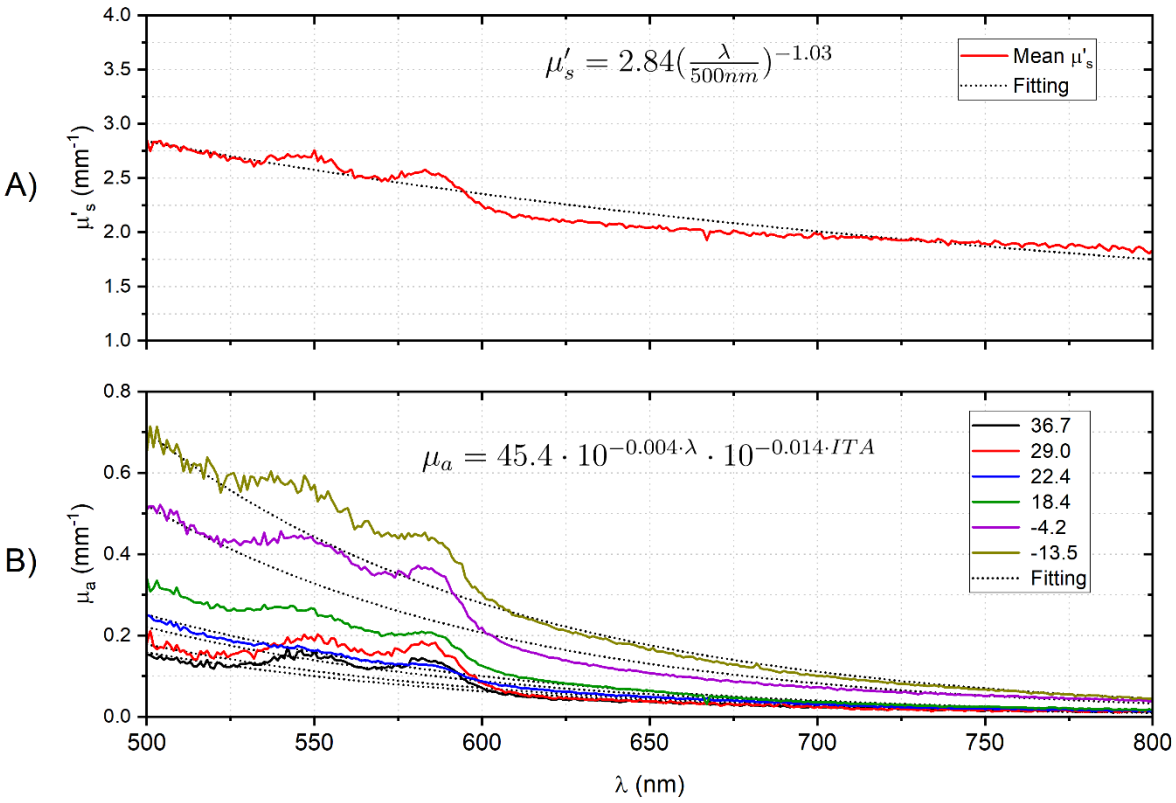

Figure 23 - Comparison between the experimental values and the fitting.

As can be seen in Figure 23, all the optical coefficients could be fitted with a good reliability. In both graphs, the μ'_s and μ_a indicate a compatibility with the experimental model, with R^2 between 0.932 and 0.997, indicating a high suitability of the model proposed in this work with the experimental results. The Hb bands were not considered in this analysis.

Some spectral regions show higher deviation with the experimental model, but this could be related to experimental limitations. The μ_a of the sample $ITA = 18.4$ showed the higher discrepancy, and this result may be associated with the ITA measuring, since human skin's

pigmentation is inhomogeneously distributed. The ITA is a relationship between the skin pigmentation and its color by a numerical approach, thus, our results are limited for the visible spectral range.

Very dark skins, such as ITA = -13.45º of this study, may not completely convert μ'_s due the higher melanin absorption found on the epidermis. This limitation was also reported in a study using spatial frequency domain imagens in different human phototypes, which the scattering coefficient were lower in higher Fitzpatrick score [74].

Our results are valid for *ex-vivo* samples. In *in-vivo*, the optical and colorimetric properties may be different because there are more physiological interactions, since the constitutive pigmentation being set by biological regulations, such as, melanoblasts migration, melanocytes density, enzymatic functions and expressions, melanin synthesis (eumelanin and pheomelanin), melanosomes transport and melanin distribution. Also, toxic compounds, like hydroquinone, may also change the skin pigmentation [112]. However, the epidermal melanocytes slowly increase under normal circumstances and are resistant to apoptosis [111], indicating that the experimental fitting proposed in this study could be applied to evaluate the melanin solely in *in-vivo* samples. This method is not suitable for hemoglobin bands, since it does not take the a^* parameter into consideration, and hyperpigmented skins were not studied in this paper, but in the future, it should be taken into consideration to confirm if the experimental model is still valid.

4.4 – Conclusions

A correlation between the absorption and reduced scattering coefficients of *ex-vivo* human skins were done through the individual typology angle by a numerical approach. The μ_a exhibited a direct relation with ITA. This pattern could be described through an exponential equation, where the parameters were acquired through a linearization method. The μ'_s does not change with ITA, but it could be described using a power law fitting. This experimental model has its limitation since it won't work for hemoglobin bands, and ranges other than visible. Both optical coefficients could be determined with R^2 higher than 0.93, indicating that the methodology is adequate and can estimate the optical parameters only with the ITA value of the skin.

4.5 – Chapter 4 Supplementary Notes

Chapter 5: Distance Independent Total Reflectance Setup for Spectrally Resolved Determination of Optical Properties of Highly Turbid Media

Abstract: A measurement system for a distance insensitive acquisition of the reflectance from turbid media is presented. The geometric relationships of the detection unit are discussed theoretically and subsequently verified using Monte Carlo simulations. In addition, an experimental setup is presented to prove the theoretical considerations and simulations. The use of the presented measurement system allows measurements of the reflectance in a distance range of approximately 2.5 cm with a deviation of less than ± 0.5% for highly scattering media. This contrasts with the use of a fiber in a classical detection unit placed at a defined angle and position relative to the sample surface, which results in deviations of ± 30% in the measured reflectance over the same distance range.

Based on the manuscript published in Applied Optics, 2022

P. Hank, K. Pink, L. B. da Cruz Junior, F. Foschum and A. Kienle; "Distance insensitive reflectance setup for the spectrally resolved determination of the optical properties of highly turbid media". Applied optics, 61(29), p.8737-8744, 2022.

DOI: 10.1364/AO.469925

***This paper is a collaboration research performed during the CAPES-Print exchange at Institut für Lasertechnologien in der Medizin (ILM) an der Universität Ulm in Germany:** Mr. Cruz Junior performed the experimental measurement present on the paper to validate the proposed theory. The current text was not written by Mr. Cruz Junior, only suggestions on the manuscript were given. A feedback letter about his stay at the ILM can be found attached at the Annex C file.

5.1 – Introduction

The correct description of light propagation in turbid media requires knowledge of their optical properties, including the phase function, scattering and absorption [153].

The phase function $p(\hat{s}, \hat{s}')$, which gives the probability density to be scattered at a scattering center from the incoming direction $\hat{s}$ into a certain direction $\hat{s}'$, can be characterized with the help of a goniometric setup [154]–[156]. However, in many applications, the Henyey-Greenstein phase function is used as an approximation when the exact phase function is not known [116].

Using the reduced scattering coefficient $\mu'_s = \mu_s(1-g)$ is, for instance, one option to draw conclusions about the microstructure of a medium [157]. In this context, g is the anisotropy factor and μs is the scattering coefficient. By using the absorption coefficient μa and specific absorption bands of different absorbers the volume concentration in the medium under investigation can be determined [158].

For the determination of the reduced scattering coefficient and the absorption coefficient, there are several possible measurement systems and associated theoretical models, which makes it possible to determine μ'_s and μ_a by measuring, for example, the reflectance or transmission of a scattering sample, respectively. This is called solving the inverse problem. Further possible measuring systems to determine the optical properties are in the time domain [159]–[163], the temporal frequency domain [164], the spatial domain [165]–[170], or the spatial frequency domain [171]–[175].

However, the searched coefficients are often determined only for a limited number of wavelengths due to limited measuring time and capability of the systems. Nevertheless, to correctly determine the concentrations of several chromophores based on absorption bands, for instance, a reasonably detailed spectral resolution of the absorption spectrum is required. To obtain this, hybrid systems can be used [175].

To determine the spectrally resolved reduced scattering coefficient, the spatially resolved reflectance for a small number of wavelengths can be used. The values between the measured wavelengths can be estimated using a power law. The spectrally resolved reduced scattering

coefficient can then be used in combination with the spectra of the total reflectance [175], where white light is directed onto a sample and the reflected light is detected spectrally resolved, e.g., with a fiber and a spectrometer, to obtain the spectrally resolved absorption coefficient by comparing to a Monte Carlo simulations.

The determination of the optical properties can be used, for instance, in process control. An important application is the control of tablets, where the pharmaceutical ingredient concentration should be checked in addition to the scattering coefficient, which correlates to the compression pressure [157].

The aim of this study is to investigate an experimental setup for measuring a distance independent total reflectance from a scattering medium to determine the optical properties. The advantage is the simplified positioning and the higher robustness of the measurement. For this purpose, the theoretical aspects are first derived and presented in detail. The theoretical preliminary considerations are then verified with a Monte Carlo method implemented by ourselves. Finally, we show experimental results of the measurement system, which also substantiate the theoretical considerations. For the experimental verification we used self-made epoxy resin phantoms with different scattering properties. Improvements of approximately two orders of magnitude were observed.

5.2 - Theory

The general idea for detecting the distance independent total reflectance is based on the use of an optical fiber with a core diameter d and a lens with a focal length f, which is depicted in Figure 24.

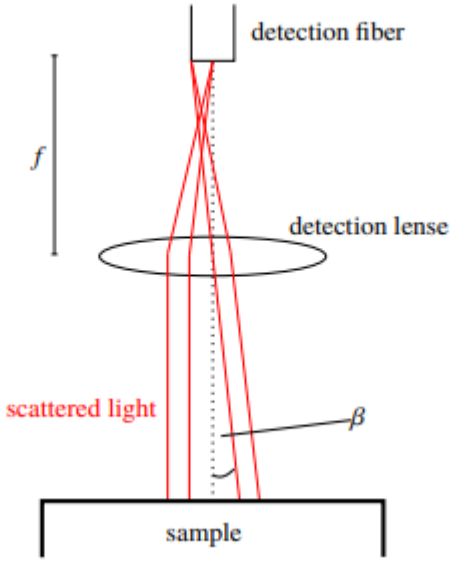

Figure 24 - Sketch showing the geometrical arrangement of the scattering sample and the detection unit.

The distance between the fiber and the lens equals exactly f, as shown in Figure 25, which is a zoom of the detection unit of Figure 24. By positioning the detection fiber at the distance of the focal length of the lens, all rays of the same angle are imaged to the same location on the fiber. This results in the transition from the spatial regime to the angular regime.

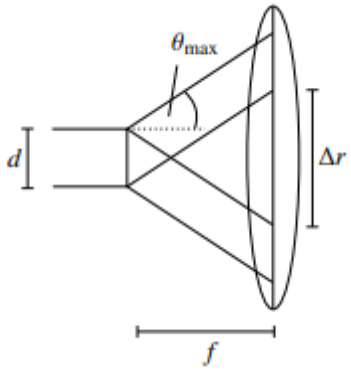

Figure 25 - Sketch showing the relationship between numerical aperture and illumination area of the lens based on a fiber diameter d and a focal length f.

When coupling light into a fiber, the numerical aperture A_N of the fiber must be taken into account. It specifies the maximum incident angle θ_{max} under which photons can still be coupled into the fiber. The numerical aperture can be calculated by

$$A_N = \sin(\theta_{max}) = \sqrt{n_{core}^2 - n_{clad}^2}. \quad (29)$$

With n_{core} and n_{clad} as the refractive indices of the core and the cladding, respectively. To ensure that photons passing through the lens and reach the fiber at an angle less than θ_{max}, the lens diameter must be limited or an aperture with diameter Δr must be installed. Δr results from the numerical aperture of the fiber and can be calculated according to

$$\Delta r = 2ftan(\arcsin(A_N)) - d. \tag{30}$$

Since the fiber is at a distance f from the lens, photons leaving the turbid medium at the angle β relative to the optical axis of the detection unit are focused to the same location ρ. The relationship between β and ρ follows from

$$\frac{\rho}{\beta} = \tan(\beta) \tag{31}$$

If we take the diameter of the fiber into account, we find that only photons leaving the turbid medium in an angular range of

$$\beta \in [0, \beta_{max}] \tag{32}$$

are coupled into the fiber, where

$$\beta_{max} = \arctan\left(\frac{d}{2f}\right) \tag{33}$$

applies. In addition to the condition that all photons hitting the lens can also be coupled into the fiber due to A_N, there is also the requirement that all photons with an angle $\beta \in [0, \beta_{max}]$ always also hit the limited circular area of the lens. This is guaranteed for photons, which are leaving the turbid medium within a circular area defined by

$$A_{ROI} = \pi \frac{y_{ROI}^2}{4} \tag{34}$$

y_{ROI} represents the diameter of the of the region of interest (ROI) at a specific distance x_{max} between the lens and the sample. The medium is, in the extreme case, located at a distance x_{max} from the lens and there the value for y_{ROI} is minimal. The geometric relationship is shown graphically in Figure 26.

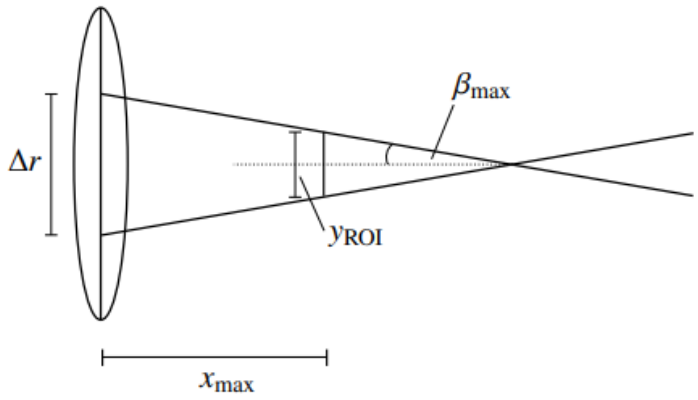

Figure 26 - Illustration of the relationship between the distance of the scattering medium to the lens and its illumination area, and the influence of the detectable photons within an angular range $\beta \in \left[0, \arctan\left(\frac{d}{2f}\right)\right]$ defined by the fiber and lens, where β describes the exit angle of a photon relative to the optical axis of the detection unit.

From the ray theorem follows

$$\frac{x - x_{max}}{y_{ROI}} = \frac{x}{\Delta r}, \tag{35}$$

where x can be determined by

$$\frac{\Delta r}{2x} = \tan(\beta_{max}) = \frac{d}{2f} \quad \Leftrightarrow \quad x = \frac{f}{d}\Delta r \tag{36}$$

For this purpose, equation (33) was used. Resolved to y_{ROI} results in

$$y_{ROI} = \left(1 - \frac{x_{max}}{x}\right)\Delta r = \Delta r - x_{max}\frac{d}{f} = 2f tan(\arcsin(A_N)) - d\left(1 + \frac{x_{max}}{f}\right). \tag{37}$$

If one chooses the maximum distance x_{max} with a defined fiber and lens, then the diameter y_{ROI} of the circular area results, in which the photons can leave the medium under an angle of β_{max} or smaller and still be detected. The illumination spot A_{ill} of the medium should be chosen much smaller than A_{ROI} to ensure that photons leaving the medium outside the illumination spot are still within A_{ROI}. The decisive quantities for light propagation here are, besides the refractive index of the turbid medium, the phase function, the absorption coefficient and the scattering coefficient.

5.3 – Material and Methods

Figure 27 illustrates the used experimental setup. This setup was implemented in a Monte Carlo simulation in order to be able to perform a simulation-based verification, in addition, to the experimental verification. For the Monte Carlo simulations, the Henyey-Greenstein phase function

$$p(\theta_{scattered}) = \frac{1}{4\pi} \frac{1 - g^2}{[1 + g^2 - 2g\cos(\theta_{scattered})]^{3/2}} \tag{38}$$

was used with an anisotropy factor of g = 0.617. The refractive index of the medium was assumed to be n_{med} = 1.56 to match the refractive index of the customary produced epoxy resin optical phantoms. The simulation has the advantage that the proof of concept can be performed with ideal components and without stray light. The extent to which real components lead to deviations will be part of section 5.4.

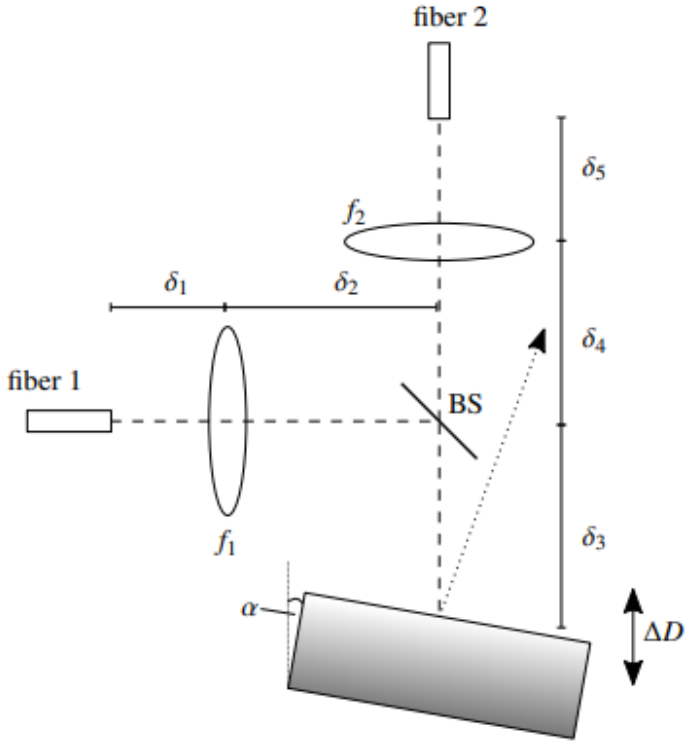

Figure 27 - Sketch showing the components used and their relative distances. BS refers to a beam splitter. Furthermore, $\delta_1 = 2f_1$, $\delta_5 = f_2$, $\delta_2 + \delta_3 = 2f_1$ and $D = \delta_3 + \delta_4 = 20$ cm is valid. To avoid the direct reflection from the surface, the sample is tilted by $\alpha = 10°$. The white light is delivered by fiber 1, which has a core diameter of 200 µm, and the light reflected from the scattering medium is coupled into the spectrometer. by

fiber 2, which has a diameter of d = 1 mm and a numerical aperture of $A_N = 0.22$. As focal lengths $f_1 = 80$ mm and $f_2 = 40$ mm was chosen.

For the sketched distances we have $\delta_1 = 2f_1,\ \delta_5 = f_2,\ \delta_2 + \delta_3 = 2f_1$ and $D = \delta_3 + \delta_4 = 20$ cm, while for the focal lengths $f_1 = 80$ mm and $f_2 = 40$ mm was chosen. The beam splitter is abbreviated with BS and the sample under investigation is tilted by $\alpha = 10°$ in order to prevent the direct reflection from the surface from being coupled into the detection system. The light source is a xenon short-arc light source (SLS401, Thorlabs Inc., 56 Sparta Avenue, Newton, New Jersey 07860, United States). It is coupled into the system via fiber 1. Fiber 2 is coupled to a spectrometer (Maya 2000-Pro, Ocean Insight, Maybachstrasse 11, Ostfildern, D-73760, Germany) for the detection of the spectrally resolved intensity. The numerical aperture of fiber 2 is $A_N = 0.22$ and the fiber diameter is d = 1 mm.

5.4 – Results

Experimental data were collected using a setup as explained in the previous chapter. Further, Monte Carlo simulations were performed reproducing the experimental setup. Different sample distances $D = \delta_3 + \delta_4$ were investigated to verify that the system is distance independent. In addition, the Monte Carlo method was used to investigate the change of the detected signal in case that the detection fiber (fiber 2) was located at a defined position in space without using any optics.

Verification by Monte Carlo method

The used Monte Carlo simulation propagates energy packages in a ray tracing manner through models of all the optical components used for the experimental setup, starting at the light source and counted at the entrance of the detection fiber. Both lenses are only modeled as ideal parts. The position of the sample was changed within a range of $\Delta D = \pm 1.5$ cm in steps of 0.5 cm, where $D = \delta_3 + \delta_4$ represents the distance from the detection lens to the sample surface. Furthermore, samples with different reduced scattering coefficients were simulated ranging from $\mu'_s = 0.1$ mm^{-1} to $\mu'_s = 100$ mm^{-1}. The absorption coefficient was kept constant at $\mu_a = 0.001$ mm^{-1}. All graphs in Figure 28 and Figure 29 show a good distance independence with differences in the detected intensity below ± 0.5% over the simulated distance range of 3 cm. $\Delta D = 0$ cm is the distance of the focus for the illumination and considerably smaller than x_{max}. To demonstrate the difference to the direct acquisition by a detection fiber positioned at

the distance $D = 10$ cm to the probe surface under an angle of 10°, the relative deviation to the mean value of all distances is shown in the lower graphs of all figures. 10 cm is a common distance in this context. The reflectance

$$I_{MC} = \frac{N_{detected}}{N_{simulated}} \tag{39}$$

was plotted, where $N_{simulated}$ is the number of photons simulated and $N_{detected}$ represents the number of photons detected by the fiber at a certain distance D. Deviations up to ± 30% are observable. In Figure 28 samples with larger reduced scattering coefficients were simulated. On the left side the results for a sample with a reduced scattering coefficient $\mu'_s = 100$ mm^{-1} are shown and on the right the results for $\mu'_s = 10$ mm^{-1}.

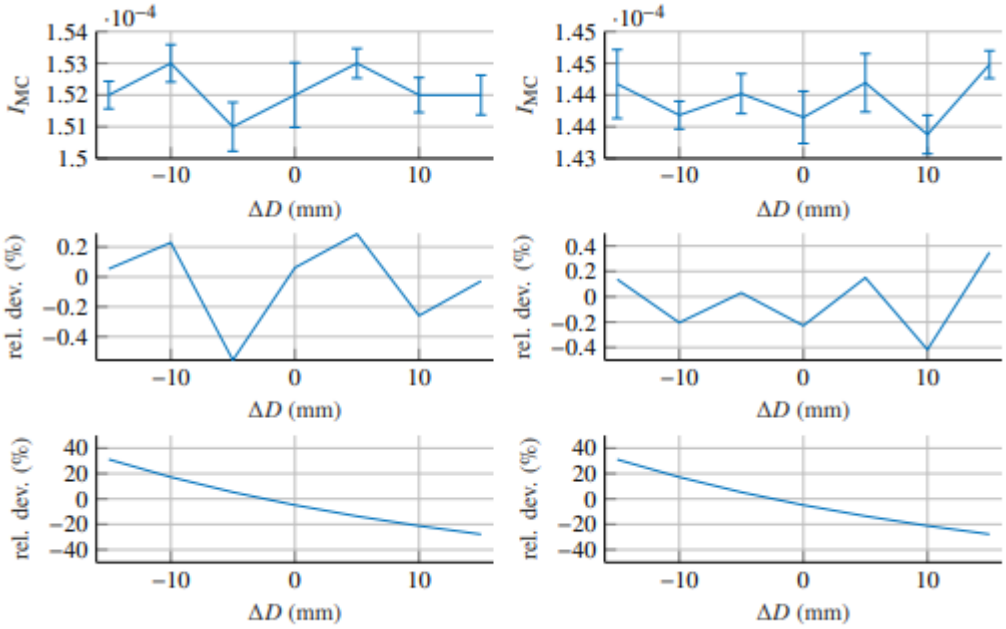

Figure 28 - The upper graphs show the reflectance versus distance as mean values for three consecutive simulations including the standard deviation. The middle graphs show the relative error to the mean value of the respective distances. The lower graphs give the relative error for all distances simulated for a fiber detector without using a lens. The left column was simulated with $\mu'_s = 100$ mm^{-1}, while the right column was simulated with $\mu'_s = 10$ mm^{-1}. μ_a is constant at 0.001 mm^{-1}.

In Figure 29 the results of the same simulations as in Figure 28 are shown, but with changed optical properties, namely $\mu'_s = 1$ mm^{-1} and $\mu'_s = 0.1$ mm^{-1}. In the middle graphs a small drop of I_{MC} can be recognized for the largest ΔD. The drop can be explained by the decrease of the size of the ROI with larger distance combined with the low scattering and the resulting

longer mean free paths. These two effects lead to the loss of light which exits the sample outside of the ROI. After a certain minimum distance this effect becomes relevant.

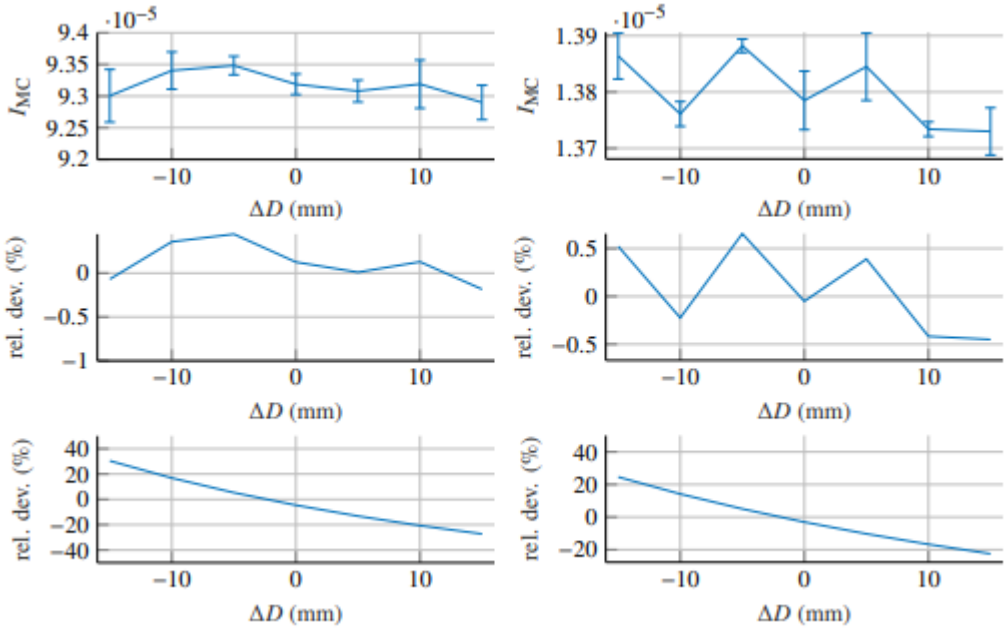

Figure 29 - The upper graphs show the reflectance versus distance as mean values for three consecutive simulations including the standard deviation. The middle graphs show the relative error to the mean value of the respective distances. The lower graphs give the relative error to the mean value for all distances simulated for a non-distance independent fiber detector. The left column was simulated with $\mu'_s = 1$ mm^{-1}, while the right column was simulated with $\mu'\_s = 0.1$ mm^{-1}. μ_a is constant at 0.001 mm^{-1}.

Experimental verification

The experiment was carried out by changing the distance $D = \delta_3 + \delta_4$ over 3 cm in steps of 0.5 cm. To obtain the reflectance, the experimentally measured spectra were always normalized to a measurement with a calibration standard (Spectralon, Labsphere Inc., 231 Shaker St, North Sutton, NH 03260, USA) at $\Delta D = 0.0$ cm having a reflectance of 99%. To calculate the relative deviation the mean reflectance of all distances was used. In Figure 30 the upper graph shows a defined subspectrum, which is called spectrum of interest, where the chromatic aberration influences the measurement the least. In the lower graph the relative deviation to the mean value at each wavelength of all distances for the whole spectrum is shown. The optical properties of the sample used for these measurements were $\mu'_s = 8.28$ mm^{-1} and $\mu_a = 0.0014$ mm^{-1} at $\lambda = 633$ nm. In the region of the spectrum of interest the relative deviation is lower

than ± 1%. In particular, the upper graph indicates that as the distance D of the sample surface and the detection lens decreases, the detected intensity slightly increases.

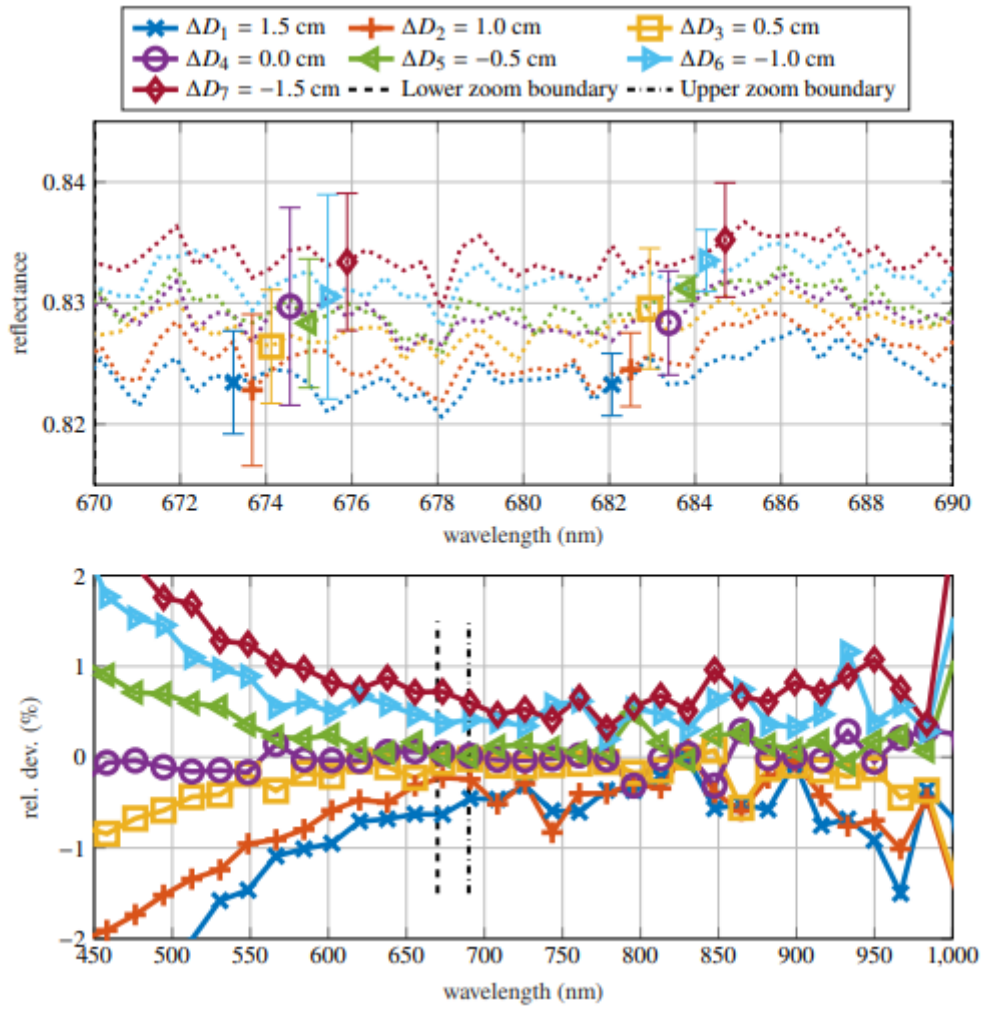

Figure 30 - Reflectance measurements of a sample with $\mu'_s = 8.28\ mm^{-1}$ and $\mu_a = 0.0014\ mm^{-1}$ at $\lambda = 633$ nm. Upper graph: Reflectance of the spectrum of interest between 670 nm and 690 nm. Lower graph: Relative deviation of the spectra to the mean value of all measured curves.

In Figure 31 measurements with a phantom having a reduced scattering coefficient of $\mu'_s = 60.87\ mm^{-1}$ and the same absorption coefficient $\mu_a = 0.0014\ mm^{-1}$ at $\lambda = 633$ nm are shown. Especially, the spectrum of interest shows that there is no systematic deviation of the curves relative to each other excluding the curve ΔD_1, where deviations are recognizable. The relative deviation is smaller than ± 0.5%. Outside of the spectrum of interest and especially for the shorter wavelengths a distance dependence is recognizable. This can be explained due to the chromatic aberration of the detection lens.

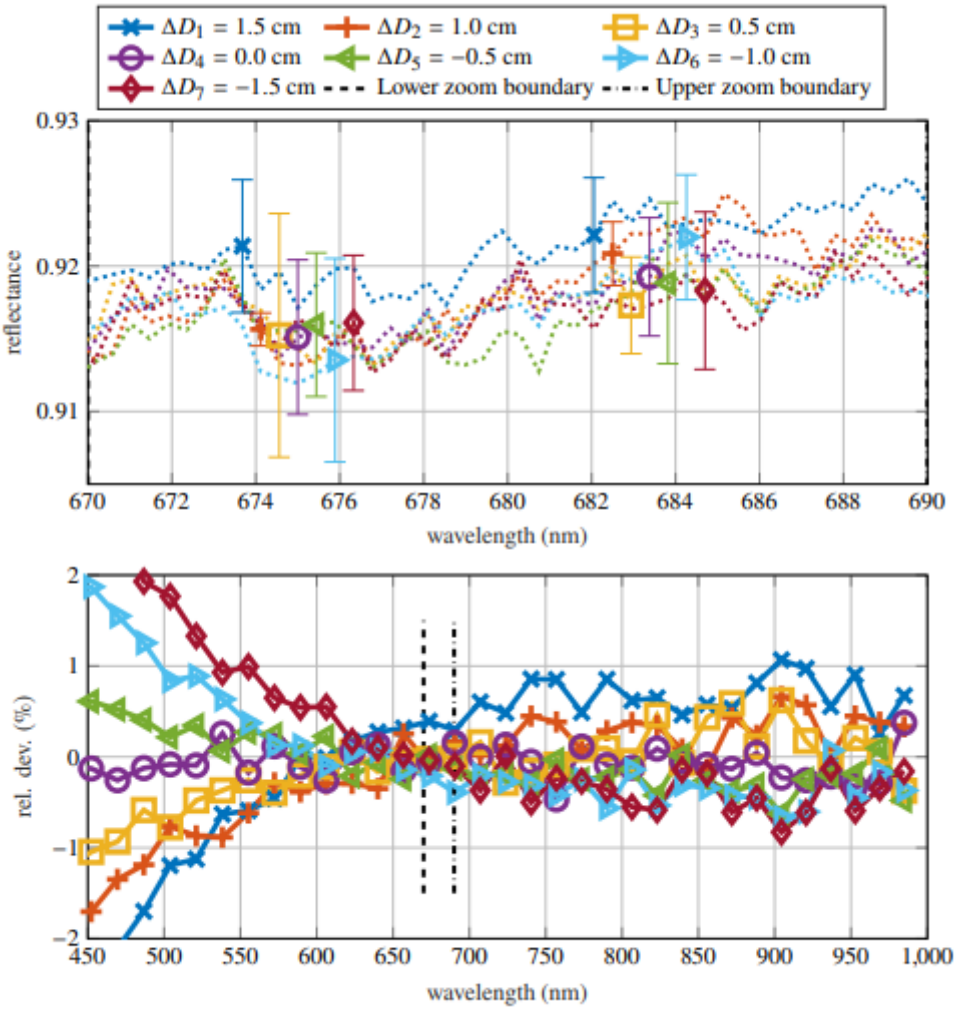

Figure 31 - Reflectance measurements of a sample with $\mu'_s = 60.87$ mm^{-1} and $\mu_a = 0.0014$ mm^{-1} at $\lambda = 633$ nm. Upper graph: Reflectance of the spectrum of interest between 670 nm and 690 nm. Lower graph: Relative deviation of the spectra to the mean value of all measured curves.

5.5 – Discussion

In this work, it was theoretically shown that a distance independent measurement of the reflected intensity from turbid media is possible within a certain range and under specific boundary conditions. The range is thereby defined by the optical parameters of the system, especially, by the lateral dimension of the illumination, by the focal length of the detection lens, by the diameter of the detection fiber, the free aperture of the detection lens and the optical properties of the sample under investigation. Using a Monte Carlo simulation, it was possible to show that the theoretical predictions could be confirmed using mainly ideal models of the optical components.

The relative difference to the mean value of all simulated curves was found to be within ± 0.5%. The results of the Monte Carlo simulation for weakly scattering samples ($\mu'_s = 1$ mm^{-1} and $\mu'_s = 0.1$ mm^{-1}) indicate a minimal loss in intensity for the largest distance of the sample surface to the detection lens. This can be explained by the large mean free paths within the sample and the decrease in size of A_{ROI}, which leads to the loss of light after a sufficient distance. By means of the experiment, we were able to show that within a range of 2.5 cm the highly scattering sample gives a relative deviation to the mean value much lower than ± 0.5% of all measured curves at different distances. This is for most applications smaller than the uncertainties caused by, for example, the intensity fluctuations of the light source. However, for the sample having a small reduced scattering coefficient ($\mu'_s = 8.28$ mm^{-1}) a slightly systematical dependence between the distance D and the measured intensity is present, as expected. An explanation for the non-perfectly working distance independence is the imperfection of the optical components. The aberrations caused by these imperfections are the more crucial, the further the light is distant from the optical axis. The smaller the scattering coefficient of the investigated scattering medium, the longer the mean free path and, therefore, the more light propagates towards the lens from a position away from the optical axis. Due to the long mean free paths light leaves the region of interest on the sample. This effect reduces the detected intensity for larger distances D. This is in good accordance with the Monte Carlo simulation although the effect was only seen for samples with significantly lower scattering coefficients and in a weaker form. In summary it is possible to perform a distance independent reflectance measurement within a certain range, depending on the measurement system and the optical properties of the samples. This is a large advance for many industrial relevant measurements, which need to be carried out fast and where an accurate positioning is not possible.

However, with the help of the total remission it is only possible to determine one optical parameter. Therefore, it is necessary to determine, for example, the scattering coefficient spectrally resolved otherwise. Since tablets, for instance, are of particular interest, the coherent backscattering (CBS) in combination with the TR is suitable as a hybrid system. With the help of the CBS, it is possible to determine the scattering coefficient of highly scattering media, when other setups, such as spatially resolved reflectance can no longer be used. Such a measurement system is to be installed and verified shortly.

Chapter 6: General Conclusions

The present thesis showed an extensive review of photonics biomedical applications and implications of the effect of melanin in diagnostics. The demand for a better understanding of dark-skinned optical properties in life sciences applications is a social demand and opens up opportunities for the biophotonics field.

Before measuring the optical properties of human skin, it was necessary to manufact an integrating spheres system, which must be calibrated and validated, to access the diffuse reflectance and transmittance of the human skin samples. The integrating spheres were manufactured using a 3D printer from the Physics Department of the University of São Paulo, Campus Ribeirão Preto, and the modeling was carried out in Autodesk software. The internal barium sulfate coating was able to maintain similar values to commercial models coated with Spectralon. Validation was performed with two calibrated biomimic phantoms acquired from INO. All the calibration steps done in this study were planned to provide the necessary data to the IAD algorithm, such as the entrance and exit port diameter, equipment diameter, internal walls and barium sulfate reflectance. Several contacts are frequently received for suggestions and questions about the system, indicating the relevance of sharing methods for manufacture adapted systems using a 3D printer, in particular, the integrating sphere.

With the equipment validated and functional, it was possible to start measuring the optical properties of the ex-vivo human skins. All samples were provided from female patients and same site (abdomen) to ensure reliability of the data. ITA was used to categorize the skin colour. A complete analysis of optical parameters relevant to biomedical applications was performed; absorption coefficient, scattering coefficient, effective attenuation coefficient, optical depth penetration and albedo. All optical properties indicated a direct correlation with ITA, except for the scattering coefficient. The absorption coefficient and the effective attenuation coefficient increase with the ITA decreasing, while to albedo and depth penetration the inverse is true. This was the first work to correlate the ITA and the optical parameters and may improve light-based diagnoses, through a reliable and reproducible method which takes into consideration the skin phototypes.

Since it was observed a correlation between the absorption coefficient and the ITA values, an experimental fitting was proposed to estimate the absorption as a function of the skin phototypes. On logarithmic scale, the absorption coefficient increases linearly with the decrease in ITA values, in other words, as lower the ITA higher the absorption coefficient. Them, it was possible to propose an experimental mathematical fitting model able to estimate skin absorption by using ITA solely. The scattering coefficient did not show significant changes as a function of the ITA, but it is known in the literature that it is possible to adjust a power law fitting. The hidden relevance of this findings lies in the possibility of, solely through skin colour, determining the appropriate fluency for medical treatment and increasing the accuracy of diagnoses. Furthermore, optical penetration depth is proportional to the absorption and scattering coefficient, and with the proposed mathematical expressions it is possible to estimate whether light, at a given wavelength, is able to penetrate the skin and deliver a proper fluence to an internal organ.

During the exchange in Germany, a height insensitive spectroscopy method was developed to measure the reflection of highly turbid samples in the visible and near infrared, at least by a few centimeters. This work paves the way for performing VIS-NIR spectroscopy measurements with higher precision and speed. For the biophotonics field, it can increase the accuracy of ITA measurements or real-time variation in skin colour as a function of biological changes, since it can be done indirectly and non-contact.

The thesis presented advances in the field of photonics and biophotonics, opening up opportunities for future work and clinical applications for dark-skinned persons. Some future possible applications are showing bellow.

Skin phototypes mimic phantom: it was studied human skin ITAs between ~33º to -13º, leaving a wide range open field to analyze. It is already known in the literature that the ITA can go up to +75º approximately, lightest skin, and below to -50º in Africans have already been reported. Thus, a broad study using tissue mimics phantoms, may further improve the understanding of how light interacts with different skin phototypes.

Optical oximetry and imaging techniques corrections: by estimating the optical absorption through ITA values, found in this thesis, it could be possible to perform an optical signal

correction routine to improve the quality of pulse oximetry devices for darker skin phototypes. It also could improve visualization of the physiological parameters of interest (e.g., artery, tendon, muscle) in imaging techniques and reduce the limitations for dark-skinned persons.

BIBLIOGRAPHY

[1] J. Popp, V. v. Tuchin, A. Chiou, and S. H. Heinemann, Eds., *Handbook of Biophotonics*, vol. 1. Wiley-VCH, 2012.

[2] K. Goda, "Biophotonics and beyond," *APL Photonics*, vol. 4, no. 5, p. 050401, May 2019, doi: 10.1063/1.5100614.

[3] C. Krafft, "Modern trends in biophotonics for clinical diagnosis and therapy to solve unmet clinical needs," *J Biophotonics*, vol. 9, no. 11–12, pp. 1362–1375, Dec. 2016, doi: 10.1002/jbio.201600290.

[4] M. Stracy, C. Lesterlin, F. Garza de Leon, S. Uphoff, P. Zawadzki, and A. N. Kapanidis, "Live-cell superresolution microscopy reveals the organization of RNA polymerase in the bacterial nucleoid," *Proceedings of the National Academy of Sciences*, vol. 112, no. 32, Aug. 2015, doi: 10.1073/pnas.1507592112.

[5] A. N. Bashkatov, E. A. Genina, V. I. Kochubey, and V. v. Tuchin, "Optical properties of human skin, subcutaneous and mucous tissues in the wavelength range from 400 to 2000 nm," *J Phys D Appl Phys*, vol. 38, no. 15, pp. 2543–2555, 2005, doi: 10.1088/0022-3727/38/15/004.

[6] L. J. G. W. van Wilderen, M. A. van der Horst, I. H. M. van Stokkum, K. J. Hellingwerf, R. van Grondelle, and M. L. Groot, "Ultrafast infrared spectroscopy reveals a key step for successful entry into the photocycle for photoactive yellow protein," *Proceedings of the National Academy of Sciences*, vol. 103, no. 41, pp. 15050–15055, Oct. 2006, doi: 10.1073/pnas.0603476103.

[7] V. Roukos, R. C. Burgess, and T. Misteli, "Generation of cell-based systems to visualize chromosome damage and translocations in living cells," *Nat Protoc*, vol. 9, no. 10, pp. 2476–2492, Oct. 2014, doi: 10.1038/nprot.2014.167.

[8] E. Stefánsson, R. Machemer, E. de Juan, B. W. McCuen, and J. Peterson, "Retinal Oxygenation and Laser Treatment in Patients With Diabetic Retinopathy," *Am J Ophthalmol*, vol. 113, no. 1, pp. 36–38, Jan. 1992, doi: 10.1016/S0002-9394(14)75750-2.

[9] T. Sakimoto, M. I. Rosenblatt, and D. T. Azar, "Laser eye surgery for refractive errors," *The Lancet*, vol. 367, no. 9520, pp. 1432–1447, Apr. 2006, doi: 10.1016/S0140-6736(06)68275-5.

[10] J. Marshall, S. L. Trokel, S. Rothery, and R. R. Krueger, “Long-term Healing of the Central Cornea after Photorefractive Keratectomy Using an Excimer Laser,” *Ophthalmology*, vol. 95, no. 10, pp. 1411–1421, Oct. 1988, doi: 10.1016/S0161-6420(88)32997-0.

[11] M. B. Eydelman *et al.*, “Standardized Analyses of Correction of Astigmatism by Laser Systems That Reshape the Cornea,” *Journal of Refractive Surgery*, vol. 22, no. 1, pp. 81–95, Jan. 2006, doi: 10.3928/1081-597X-20060101-16.

[12] D. v. Palanker *et al.*, “Femtosecond Laser–Assisted Cataract Surgery with Integrated Optical Coherence Tomography,” *Sci Transl Med*, vol. 2, no. 58, Nov. 2010, doi: 10.1126/scitranslmed.3001305.

[13] K. D. Polder, J. M. Landau, I. J. Vergilis-Kalner, L. H. Goldberg, P. M. Friedman, and S. Bruce, “Laser Eradication of Pigmented Lesions: A Review,” *Dermatologic Surgery*, vol. 37, no. 5, pp. 572–595, May 2011, doi: 10.1111/j.1524-4725.2011.01971.x.

[14] G. Scarcella, P. A. Gerber, D. Edge, and M. C. E. Nielsen, “Effective removal of solar lentigines by combination of pre– And post–fluorescent light energy treatment with picosecond laser treatment,” *Clin Case Rep*, vol. 8, no. 8, pp. 1429–1432, Aug. 2020, doi: 10.1002/ccr3.2839.

[15] K. M. Kent and E. M. Graber, “Laser tattoo removal: A review,” *Dermatologic Surgery*, vol. 38, no. 1. pp. 1–13, Jan. 2012. doi: 10.1111/j.1524-4725.2011.02187.x.

[16] J. Rao, “Treatment of Acne Scarring,” *Facial Plast Surg Clin North Am*, vol. 19, no. 2, pp. 275–291, May 2011, doi: 10.1016/j.fsc.2011.04.004.

[17] J. H. Kunishige, L. H. Goldberg, and P. M. Friedman, “Laser therapy for leg veins,” *Clin Dermatol*, vol. 25, no. 5, pp. 454–461, Sep. 2007, doi: 10.1016/j.clindermatol.2007.05.008.

[18] K. M. Kelly *et al.*, “Description and Analysis of Treatments for Port-wine Stain Birthmarks,” *Arch Facial Plast Surg*, vol. 7, no. 5, pp. 287–294, Sep. 2005, doi: 10.1001/archfaci.7.5.287.

[19] K.-H. Chen *et al.*, “A systematic review of comparative studies of CO_2 and erbium:YAG lasers in resurfacing facial rhytides (wrinkles),” *Journal of Cosmetic and Laser Therapy*, vol. 19, no. 4, pp. 199–204, May 2017, doi: 10.1080/14764172.2017.1288261.

[20] M. L. W. Juhasz and M. K. Levin, “The role of systemic treatments for skin lightening,” *J Cosmet Dermatol*, vol. 17, no. 6, pp. 1144–1157, Dec. 2018, doi: 10.1111/jocd.12747.

[21] O. A. Ibrahimi, M. M. Avram, C. W. Hanke, S. L. Kilmer, and R. R. Anderson, “Laser hair removal,” *Dermatol Ther*, vol. 24, no. 1, pp. 94–107, Jan. 2011, doi: 10.1111/j.1529-8019.2010.01382.x.

[22] R. M. Kuntz, “Laser treatment of benign prostatic hyperplasia,” *World J Urol*, vol. 25, no. 3, pp. 241–247, Jun. 2007, doi: 10.1007/s00345-007-0170-y.

[23] N. M. Fried and P. B. Irby, “Advances in laser technology and fibre-optic delivery systems in lithotripsy,” *Nat Rev Urol*, vol. 15, no. 9, pp. 563–573, Sep. 2018, doi: 10.1038/s41585-018-0035-8.

[24] N. Furzikov, “Different lasers for angioplasty: Thermooptical comparison,” *IEEE J Quantum Electron*, vol. 23, no. 10, pp. 1751–1755, Oct. 1987, doi: 10.1109/JQE.1987.1073238.

[25] A. Derkacz, “[Laser therapy application in invasive cardiology. Current state and future trends].,” *Przegl Lek*, vol. 61, no. 1, pp. 35–8, 2004.

[26] J. Sexton and D. O’hare, “Simplified treatment of vascular lesions using the argon laser,” *Journal of Oral and Maxillofacial Surgery*, vol. 51, no. 1, pp. 12–16, Jan. 1993, doi: 10.1016/S0278-2391(10)80380-5.

[27] J. Li *et al.*, “Review on Laser Technology in Intravascular Imaging and Treatment,” *Aging Dis*, vol. 13, no. 1, p. 246, 2022, doi: 10.14336/AD.2021.0711.

[28] J. D. B. Featherstone and D. G. A. Nelson, “Laser Effects On Dental Hard Tissues,” *Adv Dent Res*, vol. 1, no. 1, pp. 21–26, Dec. 1987, doi: 10.1177/08959374870010010701.

[29] J. A. Duncavage and R. H. Ossoff, “Use of the CO2 laser for malignant disease of the oral cavity,” *Lasers Surg Med*, vol. 6, no. 5, pp. 442–444, 1986, doi: 10.1002/lsm.1900060504.

[30] B. B. Burkey and G. Garrett, “Use Of The Laser In The Oral Cavity,” *Otolaryngol Clin North Am*, vol. 29, no. 6, pp. 949–961, Dec. 1996, doi: 10.1016/S0030-6665(20)30292-9.

[31] T. Inouye, T. Tanabe, M. Nakanoboh, Y. Ohmae, and M. Ogura, “Carcinoma of the larynx: role of laser surgery,” May 1995, p. 342. doi: 10.1117/12.209120.

[32] C. S. Hong, D. Deng, A. Vera, and V. L. Chiang, “Laser-interstitial thermal therapy compared to craniotomy for treatment of radiation necrosis or recurrent tumor in brain metastases failing radiosurgery,” *J Neurooncol*, vol. 142, no. 2, pp. 309–317, Apr. 2019, doi: 10.1007/s11060-019-03097-z.

[33] A. Maier, F. Tomaselli, F. Gebhard, P. Rehak, J. Smolle, and F. M. Smolle-Jüttner, "Palliation of advanced esophageal carcinoma by photodynamic therapy and irradiation," *Ann Thorac Surg*, vol. 69, no. 4, pp. 1006–1009, Apr. 2000, doi: 10.1016/S0003-4975(99)01440-X.

[34] M. Elhidsi *et al.*, "Therapeutic bronchoscopy followed by sequential radiochemotherapy in the management of life-threatening tracheal adenoid cystic carcinoma: a case report," *J Med Case Rep*, vol. 16, no. 1, p. 243, Dec. 2022, doi: 10.1186/s13256-022-03452-1.

[35] M. J. Maisels and A. F. McDonagh, "Phototherapy for Neonatal Jaundice," *New England Journal of Medicine*, vol. 358, no. 9, pp. 920–928, Feb. 2008, doi: 10.1056/NEJMct0708376.

[36] K. M. Beauchemin and P. Hays, "Phototherapy is a useful adjunct in the treatment of depressed in-patients," *Acta Psychiatr Scand*, vol. 95, no. 5, pp. 424–427, May 1997, doi: 10.1111/j.1600-0447.1997.tb09656.x.

[37] R. W. Lam, D. F. Kripke, and J. C. Gillin, "Phototherapy for Depressive Disorders: A Review," *The Canadian Journal of Psychiatry*, vol. 34, no. 2, pp. 140–147, Mar. 1989, doi: 10.1177/070674378903400215.

[38] T. A. Wehr, "Manipulations of Sleep and Phototherapy: Nonpharmacological Alternatives in the Treatment of Depression," *Clin Neuropharmacol*, vol. 13, pp. S54–S65, 1990, doi: 10.1097/00002826-199001001-00006.

[39] R. N. Golden *et al.*, "The Efficacy of Light Therapy in the Treatment of Mood Disorders: A Review and Meta-Analysis of the Evidence," *American Journal of Psychiatry*, vol. 162, no. 4, pp. 656–662, Apr. 2005, doi: 10.1176/appi.ajp.162.4.656.

[40] T. A. LeGates, D. C. Fernandez, and S. Hattar, "Light as a central modulator of circadian rhythms, sleep and affect," *Nat Rev Neurosci*, vol. 15, no. 7, pp. 443–454, Jul. 2014, doi: 10.1038/nrn3743.

[41] T. Dai, A. Gupta, C. K. Murray, M. S. Vrahas, G. P. Tegos, and M. R. Hamblin, "Blue light for infectious diseases: Propionibacterium acnes, Helicobacter pylori, and beyond?," *Drug Resistance Updates*, vol. 15, no. 4, pp. 223–236, Aug. 2012, doi: 10.1016/j.drup.2012.07.001.

[42] J. Wang, B. Li, and M. X. Wu, "Effective and lesion-free cutaneous influenza vaccination," *Proceedings of the National Academy of Sciences*, vol. 112, no. 16, pp. 5005–5010, Apr. 2015, doi: 10.1073/pnas.1500408112.

[43] D. P. Kuffler, “Photobiomodulation in promoting wound healing: a review,” *Regenerative Med*, vol. 11, no. 1, pp. 107–122, Jan. 2016, doi: 10.2217/rme.15.82.

[44] C. Dompe *et al.*, “Photobiomodulation—Underlying Mechanism and Clinical Applications,” *J Clin Med*, vol. 9, no. 6, p. 1724, Jun. 2020, doi: 10.3390/jcm9061724.

[45] M. R Hamblin, “Mechanisms and applications of the anti-inflammatory effects of photobiomodulation,” *AIMS Biophys*, vol. 4, no. 3, pp. 337–361, 2017, doi: 10.3934/biophy.2017.3.337.

[46] J. E. F. da Silva Júnior *et al.*, “Association of photobiomodulation therapy and therapeutic exercises in relation to pain intensity and neck disability in individuals with chronic neck pain: a systematic review of randomized trials,” *Lasers Med Sci*, vol. 37, no. 3, pp. 1427–1440, Apr. 2022, doi: 10.1007/s10103-021-03454-3.

[47] M. R. Hamblin, “Photobiomodulation for traumatic brain injury and stroke,” *J Neurosci Res*, vol. 96, no. 4, pp. 731–743, Apr. 2018, doi: 10.1002/jnr.24190.

[48] H. Zhu, S. O. Isikman, O. Mudanyali, A. Greenbaum, and A. Ozcan, “Optical imaging techniques for point-of-care diagnostics,” *Lab Chip*, vol. 13, no. 1, pp. 51–67, 2013, doi: 10.1039/C2LC40864C.

[49] I. R. M. Ramos, A. Malkin, and F. M. Lyng, “Current Advances in the Application of Raman Spectroscopy for Molecular Diagnosis of Cervical Cancer,” *Biomed Res Int*, vol. 2015, pp. 1–9, 2015, doi: 10.1155/2015/561242.

[50] A. J. Haes and R. P. van Duyne, “Preliminary studies and potential applications of localized surface plasmon resonance spectroscopy in medical diagnostics,” *Expert Rev Mol Diagn*, vol. 4, no. 4, pp. 527–537, Jul. 2004, doi: 10.1586/14737159.4.4.527.

[51] D. Rho, C. Breaux, and S. Kim, “Label-Free Optical Resonator-Based Biosensors,” *Sensors*, vol. 20, no. 20, p. 5901, Oct. 2020, doi: 10.3390/s20205901.

[52] A. M. Veitch, N. Uedo, K. Yao, and J. E. East, “Optimizing early upper gastrointestinal cancer detection at endoscopy,” *Nat Rev Gastroenterol Hepatol*, vol. 12, no. 11, pp. 660–667, Nov. 2015, doi: 10.1038/nrgastro.2015.128.

[53] G. Iddan, G. Meron, A. Glukhovsky, and P. Swain, “Wireless capsule endoscopy,” *Nature*, vol. 405, no. 6785, pp. 417–417, May 2000, doi: 10.1038/35013140.

[54] W. DREXLER and J. FUJIMOTO, “State-of-the-art retinal optical coherence tomography,” *Prog Retin Eye Res*, vol. 27, no. 1, pp. 45–88, Jan. 2008, doi: 10.1016/j.preteyeres.2007.07.005.

[55] A. Gh. PODOLEANU, “Optical coherence tomography,” *J Microsc*, vol. 247, no. 3, pp. 209–219, Sep. 2012, doi: 10.1111/j.1365-2818.2012.03619.x.

[56] Y. Hoshi and Y. Yamada, “Overview of diffuse optical tomography and its clinical applications,” *J Biomed Opt*, vol. 21, no. 9, p. 091312, Jul. 2016, doi: 10.1117/1.JBO.21.9.091312.

[57] L. FU and M. GU, “Fibre-optic nonlinear optical microscopy and endoscopy,” *J Microsc*, vol. 226, no. 3, pp. 195–206, Jun. 2007, doi: 10.1111/j.1365-2818.2007.01777.x.

[58] J. H. Uliana, D. R. T. Sampaio, A. A. O. Carneiro, and T. Z. Pavan, “Photoacoustic-based thermal image formation and optimization using an evolutionary genetic algorithm,” *Research on Biomedical Engineering*, vol. 34, no. 2, pp. 147–156, May 2018, doi: 10.1590/2446-4740.00218.

[59] R. F. Guthoff, A. Zhivov, and O. Stachs, “*In vivo* confocal microscopy, an inner vision of the cornea - a major review,” *Clin Exp Ophthalmol*, vol. 37, no. 1, pp. 100–117, Jan. 2009, doi: 10.1111/j.1442-9071.2009.02016.x.

[60] C. Tsui, R. Klein, and M. Garabrant, “Minimally invasive surgery: national trends in adoption and future directions for hospital strategy,” *Surg Endosc*, vol. 27, no. 7, pp. 2253–2257, Jul. 2013, doi: 10.1007/s00464-013-2973-9.

[61] I. S. Alam *et al.*, “Emerging Intraoperative Imaging Modalities to Improve Surgical Precision,” *Mol Imaging Biol*, vol. 20, no. 5, pp. 705–715, Oct. 2018, doi: 10.1007/s11307-018-1227-6.

[62] A. Egerton *et al.*, “The dopaminergic basis of human behaviors: A review of molecular imaging studies,” *Neurosci Biobehav Rev*, vol. 33, no. 7, pp. 1109–1132, Jul. 2009, doi: 10.1016/j.neubiorev.2009.05.005.

[63] Y. Liu *et al.*, “Mammalian models of chemically induced primary malignancies exploitable for imaging-based preclinical theragnostic research.,” *Quant Imaging Med Surg*, vol. 5, no. 5, pp. 708–29, Oct. 2015, doi: 10.3978/j.issn.2223-4292.2015.06.01.

[64] X. Luan, Y. Pan, Y. Gao, and Y. Song, “Recent near-infrared light-activated nanomedicine toward precision cancer therapy,” *J Mater Chem B*, vol. 9, no. 35, pp. 7076–7099, 2021, doi: 10.1039/D1TB00671A.

[65] J.-A. Sahel *et al.*, “Partial recovery of visual function in a blind patient after optogenetic therapy,” *Nat Med*, vol. 27, no. 7, pp. 1223–1229, Jul. 2021, doi: 10.1038/s41591-021-01351-4.

[66] M. Ha, S. Lim, and H. Ko, “Wearable and flexible sensors for user-interactive health-monitoring devices,” *J Mater Chem B*, vol. 6, no. 24, pp. 4043–4064, 2018, doi: 10.1039/C8TB01063C.

[67] N. L. Kazanskiy, M. A. Butt, and S. N. Khonina, “Recent Advances in Wearable Optical Sensor Automation Powered by Battery versus Skin-like Battery-Free Devices for Personal Healthcare—A Review,” *Nanomaterials*, vol. 12, no. 3, p. 334, Jan. 2022, doi: 10.3390/nano12030334.

[68] H. Xu, L. Yin, C. Liu, X. Sheng, and N. Zhao, “Recent Advances in Biointegrated Optoelectronic Devices,” *Advanced Materials*, vol. 30, no. 33, p. 1800156, Aug. 2018, doi: 10.1002/adma.201800156.

[69] S. Shabahang, S. Kim, and S. Yun, “Light-Guiding Biomaterials for Biomedical Applications,” *Adv Funct Mater*, vol. 28, no. 24, p. 1706635, Jun. 2018, doi: 10.1002/adfm.201706635.

[70] M. Niemz, *Laser-Tissue Interactions: Fundamentals and Applications*, 3rd ed. Springer, 1996.

[71] M. W. Sjoding, R. P. Dickson, T. J. Iwashyna, S. E. Gay, and T. S. Valley, “Racial Bias in Pulse Oximetry Measurement,” *New England Journal of Medicine*, vol. 383, no. 25, pp. 2477–2478, Dec. 2020, doi: 10.1056/nejmc2029240.

[72] P. E. Bickler, J. R. Feiner, and M. D. Rollins, “Factors Affecting the Performance of 5 Cerebral Oximeters During Hypoxia in Healthy Volunteers,” *Anesth Analg*, vol. 117, no. 4, pp. 813–823, Oct. 2013, doi: 10.1213/ANE.0b013e318297d763.

[73] M. J. Mendenhall, A. S. Nunez, and R. K. Martin, “Human skin detection in the visible and near infrared,” *Appl Opt*, vol. 54, no. 35, p. 10559, Dec. 2015, doi: 10.1364/AO.54.010559.

[74] T. Phan *et al.*, “Characterizing reduced scattering coefficient of normal human skin across different anatomic locations and Fitzpatrick skin types using spatial frequency domain imaging,” *J Biomed Opt*, vol. 26, no. 02, Feb. 2021, doi: 10.1117/1.JBO.26.2.026001.

[75] Y. Mantri and J. v. Jokerst, “Impact of skin tone on photoacoustic oximetry and tools to minimize bias,” *Biomed Opt Express*, vol. 13, no. 2, p. 875, Feb. 2022, doi: 10.1364/BOE.450224.

[76] X. Li *et al.*, “Optoacoustic mesoscopy analysis and quantitative estimation of specific imaging metrics in Fitzpatrick skin phototypes II to V,” *J Biophotonics*, vol. 12, no. 9, Sep. 2019, doi: 10.1002/jbio.201800442.

[77] E. F. Battle and L. M. Hobbs, “Laser therapy on darker ethnic skin,” *Dermatol Clin*, vol. 21, no. 4, pp. 713–723, Oct. 2003, doi: 10.1016/S0733-8635(03)00086-X.

[78] N. Khunger, A. Molpariya, and A. Khunger, “Complications of tattoos and tattoo removal: Stop and think before you ink,” *J Cutan Aesthet Surg*, vol. 8, no. 1, p. 30, 2015, doi: 10.4103/0974-2077.155072.

[79] B. Bent, B. A. Goldstein, W. A. Kibbe, and J. P. Dunn, “Investigating sources of inaccuracy in wearable optical heart rate sensors,” *NPJ Digit Med*, vol. 3, no. 1, p. 18, Feb. 2020, doi: 10.1038/s41746-020-0226-6.

[80] G. S. P. Fernandes, J. H. Uliana, L. Bachmann, A. A. O. Carneiro, M. A. L. Bell, and T. Z. Pavan, “Impact of skin pigmentation on photoacoustic imaging using linear array transducer: a pilot in vivo study,” in *2022 IEEE International Ultrasonics Symposium (IUS)*, Oct. 2022, pp. 1–4. doi: 10.1109/IUS54386.2022.9958826.

[81] X. Li *et al.*, “Optoacoustic mesoscopy analysis and quantitative estimation of specific imaging metrics in Fitzpatrick skin phototypes II to V,” *J Biophotonics*, vol. 12, no. 9, Sep. 2019, doi: 10.1002/jbio.201800442.

[82] Y. Mantri and J. v. Jokerst, “Impact of skin tone on photoacoustic oximetry and tools to minimize bias,” *Biomed Opt Express*, vol. 13, no. 2, p. 875, Feb. 2022, doi: 10.1364/BOE.450224.

[83] M. Xu and L. v. Wang, “Photoacoustic imaging in biomedicine,” *Review of Scientific Instruments*, vol. 77, no. 4, p. 041101, Apr. 2006, doi: 10.1063/1.2195024.

[84] K. C. Lee *et al.*, “Pulse Oximetry for Monitoring Patients with Covid-19 at Home — A Pragmatic, Randomized Trial,” *New England Journal of Medicine*, vol. 386, no. 19, pp. 1857–1859, May 2022, doi: 10.1056/NEJMc2201541.

[85] T. Greenhalgh, M. Knight, M. Inada-Kim, N. J. Fulop, J. Leach, and C. Vindrola-Padros, “Remote management of covid-19 using home pulse oximetry and virtual ward support,” *BMJ*, p. n677, Mar. 2021, doi: 10.1136/bmj.n677.

[86] S. del Bino and F. Bernerd, “Variations in skin colour and the biological consequences of ultraviolet radiation exposure,” *British Journal of Dermatology*, vol. 169, no. SUPPL. 3. pp. 33–40, 2013. doi: 10.1111/bjd.12529.

[87] T. B. Fitzpatrick, “Soleil et peau [Sun and skin],” *Journal de Medecine Esthetique*, vol. 2, pp. 33–34, 1975.

[88] T. B. Fitzpatrick, “The validity and practicality of sun-reactive skin types I through VI,” *Arch Dermatol*, vol. 124, no. 6, pp. 869–871, Jun. 1988, doi: 10.1001/archderm.124.6.869.

[89] M. S. Sommers *et al.*, “Are the Fitzpatrick Skin Phototypes Valid for Cancer Risk Assessment in a Racially and Ethnically Diverse Sample of Women?,” *Ethn Dis*, vol. 29, no. 3, pp. 505–512, Jul. 2019, doi: 10.18865/ed.29.3.505.

[90] C. E. Dubin Ba, G. W. Kimmel, P. W. Hashim, J. K. Nia, and J. A. Zeichner, “Objective Evaluation of Skin Sensitivity Across Fitzpatrick Skin Types,” *J Drugs Dermatol*, vol. 19, no. 7, pp. 699–702, 2020, doi: 10.36849/JDD.2020.4880.

[91] O. N. Agbai *et al.*, “Skin cancer and photoprotection in people of color: A review and recommendations for physicians and the public,” *J Am Acad Dermatol*, vol. 70, no. 4, pp. 748–762, Apr. 2014, doi: 10.1016/j.jaad.2013.11.038.

[92] I. L. Weatherall and B. D. Coombs, “Skin Color Measurements in Terms of CIELAB Color Space Values,” *Journal of Investigative Dermatology*, vol. 99, no. 4, pp. 468–473, Oct. 1992, doi: 10.1111/1523-1747.ep12616156.

[93] S. Alaluf, D. Atkins, K. Barrett, M. Blount, N. Carter, and A. Heath, “The Impact of Epidermal Melanin on Objective Measurements of Human Skin Colour,” *Pigment Cell Res*, vol. 15, no. 2, pp. 119–126, Apr. 2002, doi: 10.1034/j.1600-0749.2002.1o072.x.

[94] W. S. Huang *et al.*, “High correlation between skin color based on CIELAB color space, epidermal melanocyte ratio, and melanocyte melanin content,” *PeerJ*, vol. 2018, no. 5, 2018, doi: 10.7717/peerj.4815.

[95] A. Chardon, I. Cretois, and C. Hourseau, “Skin colour typology and suntanning pathways,” 1991.

[96] F. A. S. Addor, C. B. Barcaui, E. E. Gomes, O. Lupi, C. R. Marçon, and H. A. Miot, “Sunscreen lotions in the dermatological prescription: review of concepts and controversies,” *An Bras Dermatol*, vol. 97, no. 2, pp. 204–222, Mar. 2022, doi: 10.1016/j.abd.2021.05.012.

[97] G. Zonios, J. Bykowski, and N. Kollias, “Skin Melanin, Hemoglobin, and Light Scattering Properties can be Quantitatively Assessed In Vivo Using Diffuse Re¯ectance Spectroscopy,” 2001.

[98] L. Jiang *et al.*, “Skin color measurements before and after two weeks of sun exposure,” *Vision Res*, vol. 192, p. 107976, Mar. 2022, doi: 10.1016/j.visres.2021.107976.

[99] S. del Bino *et al.*, “Chemical analysis of constitutive pigmentation of human epidermis reveals constant eumelanin to pheomelanin ratio,” *Pigment Cell Melanoma Res*, vol. 28, no. 6, pp. 707–717, Nov. 2015, doi: 10.1111/pcmr.12410.

[100] C. Y. Wright, M. Wilkes, J. L. Plessis, and A. I. Reeder, “Self-reported skin colour and erythemal sensitivity vs. objectively measured constitutive skin colour in an <scp>A</scp> frican population with predominantly dark skin,” *Photodermatol Photoimmunol Photomed*, vol. 31, no. 6, pp. 315–324, Nov. 2015, doi: 10.1111/phpp.12191.

[101] L. E. Au, S. S. Harris, J. T. Dwyer, P. F. Jacques, and J. M. Sacheck, “Association of serum 25-hydroxyvitamin D with race/ethnicity and constitutive skin color in urban schoolchildren,” *Journal of Pediatric Endocrinology and Metabolism*, vol. 0, no. 0, Jan. 2014, doi: 10.1515/jpem-2014-0068.

[102] M. Charlton *et al.*, “The effect of constitutive pigmentation on the measured emissivity of human skin,” *PLoS One*, vol. 15, no. 11, p. e0241843, Nov. 2020, doi: 10.1371/journal.pone.0241843.

[103] E. K. Chan, B. Sorg, D. Protsenko, M. O’neil, M. Motamedi, and A. J. Welch, “Effects of Compression on Soft Tissue Optical Properties,” 1996.

[104] C. R. Simpson, M. Kohl, M. Essenpreis, and M. Cope, “Near-infrared optical properties of ex vivo human skin and subcutaneous tissues measured using the Monte Carlo inversion technique,” *Phys Med Biol*, vol. 43, no. 9, pp. 2465–2478, 1998, doi: 10.1088/0031-9155/43/9/003.

[105] T. L. Troy and S. N. Thennadil, “Optical properties of human skin in the near infrared wavelength range of 1000 to 2200 nm,” *J Biomed Opt*, vol. 6, no. 2, p. 167, 2001, doi: 10.1117/1.1344191.

[106] A. E. Karsten, A. Singh, P. A. Karsten, and M. W. H. Braun, “Diffuse Reflectance Spectroscopy as a Tool to Measure the Absorption Coefficient in Skin: South African Skin Phototypes,” *Photochem Photobiol*, vol. 89, no. 1, pp. 227–233, Jan. 2013, doi: 10.1111/j.1751-1097.2012.01220.x.

[107] N. Bosschaart, R. Mentink, J. H. Kok, T. G. van Leeuwen, and M. C. G. Aalders, “Optical properties of neonatal skin measured in vivo as a function of age and skin pigmentation,” *J Biomed Opt*, vol. 16, no. 9, p. 097003, 2011, doi: 10.1117/1.3622629.

[108] E. B. Wassenaar and J. G. H. van den Brand, “Reliability of Near-Infrared Spectroscopy in People With Dark Skin Pigmentation,” *J Clin Monit Comput*, vol. 19, no. 3, pp. 195–199, Jun. 2005, doi: 10.1007/s10877-005-1655-0.

[109] N. BHATT and T. S. ALSTER, “Laser Surgery in Dark Skin,” *Dermatologic Surgery*, vol. 34, no. 2, pp. 184–195, Jan. 2008, doi: 10.1111/j.1524-4725.2007.34036.x.

[110] E. F. Battle and C. E. Soden, “The Use of Lasers in Darker Skin Types,” *Semin Cutan Med Surg*, vol. 28, no. 2, pp. 130–140, Jun. 2009, doi: 10.1016/j.sder.2009.04.003.

[111] Y. Yamaguchi, M. Brenner, and V. J. Hearing, “The Regulation of Skin Pigmentation,” *Journal of Biological Chemistry*, vol. 282, no. 38, pp. 27557–27561, Sep. 2007, doi: 10.1074/jbc.R700026200.

[112] Y. Yamaguchi and V. J. Hearing, “Physiological factors that regulate skin pigmentation,” *BioFactors*, vol. 35, no. 2, pp. 193–199, Mar. 2009, doi: 10.1002/biof.29.

[113] L. A. Goldsmith, *Physiology, Biochemistry, and Molecular Biology of the Skin*, 2nd ed., vol. 2. Oxford University Press, 1991.

[114] W. D. James, D. Elston, J. R. Treat, and M. A. Rosenbach, *Andrews’ Diseases of the Skin*, 10th ed. Elsevier, 2006.

[115] A. R. Young, “Chromophores in human skin,” *Phys Med Biol*, vol. 42, no. 5, pp. 789–802, May 1997, doi: 10.1088/0031-9155/42/5/004.

[116] L. C. Henyey and J. L. Greenstein, “Diffuse radiation in the Galaxy,” *Astrophys J*, vol. 93, p. 70, Jan. 1941, doi: 10.1086/144246.

[117] Y. Wu, T. Tanaka, and M. Akimoto, “Utilization of Individual Typology Angle (ITA) and Hue Angle in the Measurement of Skin Color on Images,” *Bioimaging Society*, vol. 28, pp. 1–8, 2020.

[118] S. A. Prahl, M. J. C. van Gemert, and A. J. Welch, “Determining the optical properties of turbid media by using the adding–doubling method,” *Appl Opt*, vol. 32, no. 4, p. 559, 1993, doi: 10.1364/ao.32.000559.

[119] S. A. Prahl, “Everything I think you should know about inverse adding-doubling,” *Oregon Medical Laser Center, St. Vincent Hospital*, vol. 1344, no. March, pp. 1–74, 2011, [Online]. Available: http://omlc.ogi.edu/software/iad

[120] J. F. Beek *et al.*, “In vitro double-integrating-sphere optical properties of tissues between 630 and 1064 nm,” *Phys Med Biol*, vol. 42, no. 11, pp. 2255–2261, 1997, doi: 10.1088/0031-9155/42/11/017.

[121] J. W. Pickering, S. A. Prahl, N. van Wieringen, J. F. Beek, H. J. C. M. Sterenborg, and M. J. C. van Gemert, "Double-integrating-sphere system for measuring the optical properties of tissue," *Appl Opt*, vol. 32, no. 4, p. 399, 1993, doi: 10.1364/ao.32.000399.

[122] C. Zhang, N. C. Anzalone, R. P. Faria, and J. M. Pearce, "Open-Source 3D-Printable Optics Equipment," *PLoS One*, vol. 8, no. 3, 2013, doi: 10.1371/journal.pone.0059840.

[123] T. Baden, A. M. Chagas, G. Gage, T. Marzullo, L. L. Prieto-Godino, and T. Euler, "Open Labware: 3-D Printing Your Own Lab Equipment," *PLoS Biol*, vol. 13, no. 3, pp. 1–12, 2015, doi: 10.1371/journal.pbio.1002086.

[124] B. Wijnen, E. J. Hunt, G. C. Anzalone, and J. M. Pearce, "Open-source syringe pump library," *PLoS One*, vol. 9, no. 9, pp. 1–8, 2014, doi: 10.1371/journal.pone.0107216.

[125] L. J. Salazar-Serrano, J. P. Torres, and A. Valencia, "A 3D printed toolbox for opto-mechanical components," *PLoS One*, vol. 12, no. 1, 2017, doi: 10.1371/journal.pone.0169832.

[126] J. J. Tomes and C. E. Finlayson, "Low cost 3D-printing used in an undergraduate project: An integrating sphere for measurement of photoluminescence quantum yield," *Eur J Phys*, vol. 37, no. 5, 2016, doi: 10.1088/0143-0807/37/5/055501.

[127] R. S. P. S. Storm, Shannon L. (Ph. D. and P. S. Springsteen, Art (Ph. D., "The Integrating Sphere Reflectance Accessory," *Labsphere - February 1998 - Application Note No. 03*, no. Choosing the Right Sphere Size for Your Application The Integrating Sphere Reflectance Accessory, p. 7, 1998, [Online]. Available: https://www.labsphere.com/site/assets/files/2558/choosing-the-right-sphere-size-for-your-application.pdf

[128] L. M. Hanssen and K. A. Snail, "Integrating Spheres for Mid- and Near-Infrared Reflection Spectroscopy," *Handbook of Vibrational Spectroscopy*, 2001, doi: 10.1002/0470027320.s2405.

[129] N. Knighton and B. Bugbee, "A Mixture of Barium Sulfate and White Paint is a Low-Cost Substitute Reflectance Standard for Spectralon ® % Paint," *North*, no. Figure 1, pp. 4–6, 1981.

[130] T. P. Moffitt, "Compact Fiber-Optic Diffuse Reflection Probes for Medical Diagnostics," *PhD Thesis, Western Washington University*, no. July, pp. 1–73, 2007.

[131] A. L. Dayton and S. A. Prahl, "Turbid-polyurethane phantom for microscopy," *Design and Performance Validation of Phantoms Used in Conjunction with Optical Measurements of Tissue*, vol. 6870, no. 503, p. 687006, 2008, doi: 10.1117/12.764010.

[132] T. Moffitt, Y.-C. Chen, and S. A. Prahl, “Preparation and characterization of polyurethane optical phantoms,” *J Biomed Opt*, vol. 11, no. 4, p. 041103, 2006, doi: 10.1117/1.2240972.

[133] J.-P. Bouchard, I. Veilleux, R. Jedidi, I. Noiseux, M. Fortin, and O. Mermut, “Reference optical phantoms for diffuse optical spectroscopy Part 1 – Error analysis of a time resolved transmittance characterization method,” *Opt Express*, vol. 18, no. 11, p. 11495, 2010, doi: 10.1364/oe.18.011495.

[134] G. M. Hale and M. R. Querry, “Optical Constants of Water in the 200-nm to 200-µm Wavelength Region,” *Appl Opt*, vol. 12, no. 3, p. 555, 1973, doi: 10.1364/ao.12.000555.

[135] F. A. DeThomas, J. W. Hall, and S. L. Monfre, “Real-time monitoring of polyurethane production using near-infrared spectroscopy,” *Talanta*, vol. 41, no. 3, pp. 425–431, 1994, doi: 10.1016/0039-9140(93)E0055-I.

[136] J. M. Bjordal, C. Couppé, R. T. Chow, J. Tunér, and E. A. Ljunggren, “A systematic review of low level laser therapy with location-specific doses for pain from chronic joint disorders,” *Australian Journal of Physiotherapy*, vol. 49, no. 2. Australian Physiotherapy Association, pp. 107–116, 2003. doi: 10.1016/S0004-9514(14)60127-6.

[137] F. Bergmann, F. Foschum, L. Marzel, and A. Kienle, “Ex vivo determination of broadband absorption and effective scattering coefficients of porcine tissue,” *Photonics*, vol. 8, no. 9, Sep. 2021, doi: 10.3390/photonics8090365.

[138] E. K. Chan, B. Sorg, D. Protsenko, M. O’Neil, M. Motamedi, and A. J. Welch, “Effects of compression on soft tissue optical properties,” *IEEE Journal on Selected Topics in Quantum Electronics*, vol. 2, no. 4, pp. 943–950, 1996, doi: 10.1109/2944.577320.

[139] E. Salomatina, B. Jiang, J. Novak, and A. N. Yaroslavsky, “Optical properties of normal and cancerous human skin in the visible and near-infrared spectral range,” *J Biomed Opt*, vol. 11, no. 6, p. 064026, 2006, doi: 10.1117/1.2398928.

[140] E. A. Genina, A. N. Bashkatov, V. I. Kochubey, and V. v. Tuchin, “Effect of storage conditions of skin samples on their optical characteristics,” *Optics and Spectroscopy (English translation of Optika i Spektroskopiya)*, vol. 107, no. 6, pp. 934–938, Dec. 2009, doi: 10.1134/S0030400X09120169.

[141] M. A. Calin and S. v. Parasca, “In vivo study of age-related changes in the optical properties of the skin,” *Lasers Med Sci*, vol. 25, no. 2, pp. 269–274, Mar. 2010, doi: 10.1007/s10103-009-0725-9.

[142] G. Zonios, A. Dimou, M. Carrara, and R. Marchesini, “In Vivo Optical Properties of Melanocytic Skin Lesions: Common Nevi, Dysplastic Nevi and Malignant Melanoma”, doi: 10.1111.

[143] M. Osto, I. H. Hamzavi, H. W. Lim, and I. Kohli, “Individual Typology Angle and Fitzpatrick Skin Phototypes are Not Equivalent in Photodermatology,” *Photochem Photobiol*, vol. 98, no. 1, pp. 127–129, Jan. 2022, doi: 10.1111/php.13562.

[144] L. B. da Cruz Junior and L. Bachmann, “Manufacture and characterization of a 3D-printed integrating sphere,” *Instrum Sci Technol*, vol. 49, no. 3, pp. 276–287, May 2021, doi: 10.1080/10739149.2020.1824922.

[145] N. Madkhali, Hadi. R. Alqahtani, S. Al-Terary, A. Laref, and A. Hassib, “Control of optical absorption and fluorescence spectroscopies of natural melanin at different solution concentrations,” *Opt Quantum Electron*, vol. 51, no. 7, p. 227, Jul. 2019, doi: 10.1007/s11082-019-1936-3.

[146] T. Lister, P. A. Wright, and P. H. Chappell, “Optical properties of human skin,” *J Biomed Opt*, vol. 17, no. 9, p. 0909011, Sep. 2012, doi: 10.1117/1.JBO.17.9.090901.

[147] R. K. Lauridsen, H. Everland, L. F. Nielsen, S. B. Engelsen, and L. Nørgaard, “Exploratory multivariate spectroscopic study on human skin,” *Skin Research and Technology*, vol. 9, no. 2, pp. 137–146, May 2003, doi: 10.1034/j.1600-0846.2003.00014.x.

[148] F. Ries, V. Kapoustina, A. Kron, A. Fink, and M. Rädle, “Estimation of skin phototypes with optical parameters: an experimental study using newly developed fibre optic detection device,” *Int J Cosmet Sci*, vol. 35, no. 1, pp. 50–56, Feb. 2013, doi: 10.1111/ics.12003.

[149] J. B. Fishkin and E. Gratton, “Propagation of photon-density waves in strongly scattering media containing an absorbing semi-infinite plane bounded by a straight edge,” *Journal of the Optical Society of America A*, vol. 10, no. 1, p. 127, Jan. 1993, doi: 10.1364/JOSAA.10.000127.

[150] V. v. Tuchin, *Tissue Optics: Light Scattering Methods and Instruments for Medical Diagnosis*. Society of Photo-Optical Instrumentation Engineers (SPIE), 2015. doi: 10.1117/3.1003040.

[151] G. Ablon, “Phototherapy with Light Emitting Diodes: Treating a Broad Range of Medical and Aesthetic Conditions in Dermatology.,” *J Clin Aesthet Dermatol*, vol. 11, no. 2, pp. 21–27, Feb. 2018.

[152] L. B. da Cruz Junior, C. Girasol, P. S. Coltro, R. R. de J. Guirro, and L. Bachmann, “Optical Properties of Human Skin Phototypes and their Correlation with Individual Angle Typology,” *Photobiomodul Photomed Laser Surg*, vol. Under review, no. ID PHOTOB-2022-0111, pp. 1–15, 2022.

[153] A. Ishimaru, *Wave Propagation and Scattering in Random Media*, vol. 2. Elsevier, 1978. doi: 10.1016/B978-0-12-374701-3.X5001-7.

[154] S. Nothelfer, F. Foschum, and A. Kienle, “Goniometer for determination of the spectrally resolved scattering phase function of suspended particles,” *Review of Scientific Instruments*, vol. 90, no. 8, p. 083110, Aug. 2019, doi: 10.1063/1.5086294.

[155] F. Foschum and A. Kienle, “Optimized goniometer for determination of the scattering phase function of suspended particles: simulations and measurements,” *J Biomed Opt*, vol. 18, no. 8, p. 085002, Aug. 2013, doi: 10.1117/1.JBO.18.8.085002.

[156] R. Drezek, A. Dunn, and R. Richards-Kortum, “Light scattering from cells: finite-difference time-domain simulations and goniometric measurements,” *Appl Opt*, vol. 38, no. 16, p. 3651, Jun. 1999, doi: 10.1364/AO.38.003651.

[157] A. Häffner, P. Krauter, and A. Kienle, “Density-dependent determination of scattering properties of pharmaceutical tablets using coherent backscattering spectroscopy,” *Opt Express*, vol. 26, no. 16, p. 19964, Aug. 2018, doi: 10.1364/OE.26.019964.

[158] S. A. Lohner, K. Biegert, S. Nothelfer, A. Hohmann, R. McCormick, and A. Kienle, “Determining the optical properties of apple tissue and their dependence on physiological and morphological characteristics during maturation. Part 1: Spatial frequency domain imaging,” *Postharvest Biol Technol*, vol. 181, p. 111647, Nov. 2021, doi: 10.1016/j.postharvbio.2021.111647.

[159] C. Abrahamsson, J. Johansson, S. Andersson-Engels, S. Svanberg, and S. Folestad, “Time-Resolved NIR Spectroscopy for Quantitative Analysis of Intact Pharmaceutical Tablets,” *Anal Chem*, vol. 77, no. 4, pp. 1055–1059, Feb. 2005, doi: 10.1021/ac0487754.

[160] D. Khoptyar *et al.*, “Broadband photon time-of-flight spectroscopy of pharmaceuticals and highly scattering plastics in the VIS and close NIR spectral ranges,” *Opt Express*, vol. 21, no. 18, p. 20941, Sep. 2013, doi: 10.1364/OE.21.020941.

[161] B. Chance *et al.*, “Comparison of time-resolved and -unresolved measurements of deoxyhemoglobin in brain.,” *Proceedings of the National Academy of Sciences*, vol. 85, no. 14, pp. 4971–4975, Jul. 1988, doi: 10.1073/pnas.85.14.4971.

[162] E. Simon, P. Krauter, and A. Kienle, “Time-resolved measurements of the optical properties of fibrous media using the anisotropic diffusion equation,” *J Biomed Opt*, vol. 19, no. 7, p. 075006, Jul. 2014, doi: 10.1117/1.JBO.19.7.075006.

[163] M. S. Patterson, B. Chance, and B. C. Wilson, “Time resolved reflectance and transmittance for the noninvasive measurement of tissue optical properties,” *Appl Opt*, vol. 28, no. 12, p. 2331, Jun. 1989, doi: 10.1364/AO.28.002331.

[164] M. S. Patterson, J. D. Moulton, B. C. Wilson, K. W. Berndt, and J. R. Lakowicz, “Frequency-domain reflectance for the determination of the scattering and absorption properties of tissue,” *Appl Opt*, vol. 30, no. 31, p. 4474, Nov. 1991, doi: 10.1364/AO.30.004474.

[165] A. Kienle, L. Lilge, M. S. Patterson, R. Hibst, R. Steiner, and B. C. Wilson, “Spatially resolved absolute diffuse reflectance measurements for noninvasive determination of the optical scattering and absorption coefficients of biological tissue,” *Appl Opt*, vol. 35, no. 13, p. 2304, May 1996, doi: 10.1364/AO.35.002304.

[166] R. A. J. Groenhuis, H. A. Ferwerda, and J. J. ten Bosch, “Scattering and absorption of turbid materials determined from reflection measurements 1: Theory,” *Appl Opt*, vol. 22, no. 16, p. 2456, Aug. 1983, doi: 10.1364/AO.22.002456.

[167] R. A. J. Groenhuis, J. J. ten Bosch, and H. A. Ferwerda, “Scattering and absorption of turbid materials determined from reflection measurements 2: Measuring method and calibration,” *Appl Opt*, vol. 22, no. 16, p. 2463, Aug. 1983, doi: 10.1364/AO.22.002463.

[168] F. Foschum, M. Jäger, and A. Kienle, “Fully automated spatially resolved reflectance spectrometer for the determination of the absorption and scattering in turbid media,” *Review of Scientific Instruments*, vol. 82, no. 10, p. 103104, Oct. 2011, doi: 10.1063/1.3648120.

[169] V. Markel, “Modified spherical harmonics method for solving the radiative transport equation,” *Waves in Random Media*, vol. 14, no. 1, pp. L13–L19, Jan. 2004, doi: 10.1088/0959-7174/14/1/L02.

[170] M. Machida, “The Green’s function for the three-dimensional linear Boltzmann equation via Fourier transform,” *J Phys A Math Theor*, vol. 49, no. 17, p. 175001, Apr. 2016, doi: 10.1088/1751-8113/49/17/175001.

[171] D. J. Cuccia, F. Bevilacqua, A. J. Durkin, and B. J. Tromberg, “Modulated imaging: quantitative analysis and tomography of turbid media in the spatial-frequency domain,” *Opt Lett*, vol. 30, no. 11, p. 1354, Jun. 2005, doi: 10.1364/OL.30.001354.

[172] S. Nothelfer, F. Bergmann, A. Liemert, D. Reitzle, and A. Kienle, “Spatial frequency domain imaging using an analytical model for separation of surface and volume scattering,” *J Biomed Opt*, vol. 24, no. 07, p. 1, Sep. 2018, doi: 10.1117/1.JBO.24.7.071604.

[173] B. J. Tromberg *et al.*, “Non–invasive measurements of breast tissue optical properties using frequency–domain photon migration,” *Philos Trans R Soc Lond B Biol Sci*, vol. 352, no. 1354, pp. 661–668, Jun. 1997, doi: 10.1098/rstb.1997.0047.

[174] M. Machida, Y. Hoshi, K. Kagawa, and K. Takada, “Decay behavior and optical parameter identification for spatial-frequency domain imaging by the radiative transport equation,” *Journal of the Optical Society of America A*, vol. 37, no. 12, p. 2020, Dec. 2020, doi: 10.1364/JOSAA.402124.

[175] F. Foschum, “Broadband absorption spectroscopy of turbid media using a dual step steady-state method,” *J Biomed Opt*, vol. 17, no. 3, p. 037009, Apr. 2012, doi: 10.1117/1.JBO.17.3.037009.

ANNEX A

Mathematical sequence to compute the L*a*b* coordinates by using an integrating sphere or spectrometers.

$$L^* = 116 \cdot f\left(\frac{Y}{Y_n}\right) - 16 \tag{3}$$

$$a^* = 500 \cdot \left(f\left(\frac{X}{X_n}\right) - f\left(\frac{Y}{Y_n}\right)\right) \tag{4}$$

$$b^* = 200 \cdot \left(f\left(\frac{Y}{Y_n}\right) - f\left(\frac{Z}{Z_n}\right)\right) \tag{5}$$

$f(t)$ is a conditional equation according to (6)

$$f(t) = \begin{cases} \sqrt[3]{t} & if\ t > \delta^3 \\ \frac{t}{3\delta^2} + \frac{4}{29} & otherwise \end{cases} \tag{6}$$

were $\delta = {}^{6}/_{29}$ and $t = {}^{Y}/_{Y_n}$; ${}^{X}/_{X_n}$; ${}^{Z}/_{Z_n}$. To compute X, Y and Z the equations (7) to (10) can be used.

$$X = \frac{K}{N}\int_{\lambda_1}^{\lambda_2} S(\lambda)I(\lambda)\bar{x}d\lambda \tag{7}$$

$$Y = \frac{K}{N}\int_{\lambda_1}^{\lambda_2} S(\lambda)I(\lambda)\bar{y}d\lambda \tag{8}$$

$$Z = \frac{K}{N}\int_{\lambda_1}^{\lambda_2} S(\lambda)I(\lambda)\bar{z}d\lambda \tag{9}$$

and

$$N = \int_{\lambda_1}^{\lambda_2} I(\lambda)\bar{y}d\lambda \tag{10}$$

where $S(\lambda)$ is the experimental reflectance signal, $I(\lambda)$ the source signal, $\bar{x}$, $\bar{y}$ and $\bar{z}$ are the chromatic response normalized by the human eye (tristimulus), and N is a normalization factor. To compute X_n, Y_n and Z_n a white reference must be used. K is a set constant.

Annex B

IAD algorithm diagram.

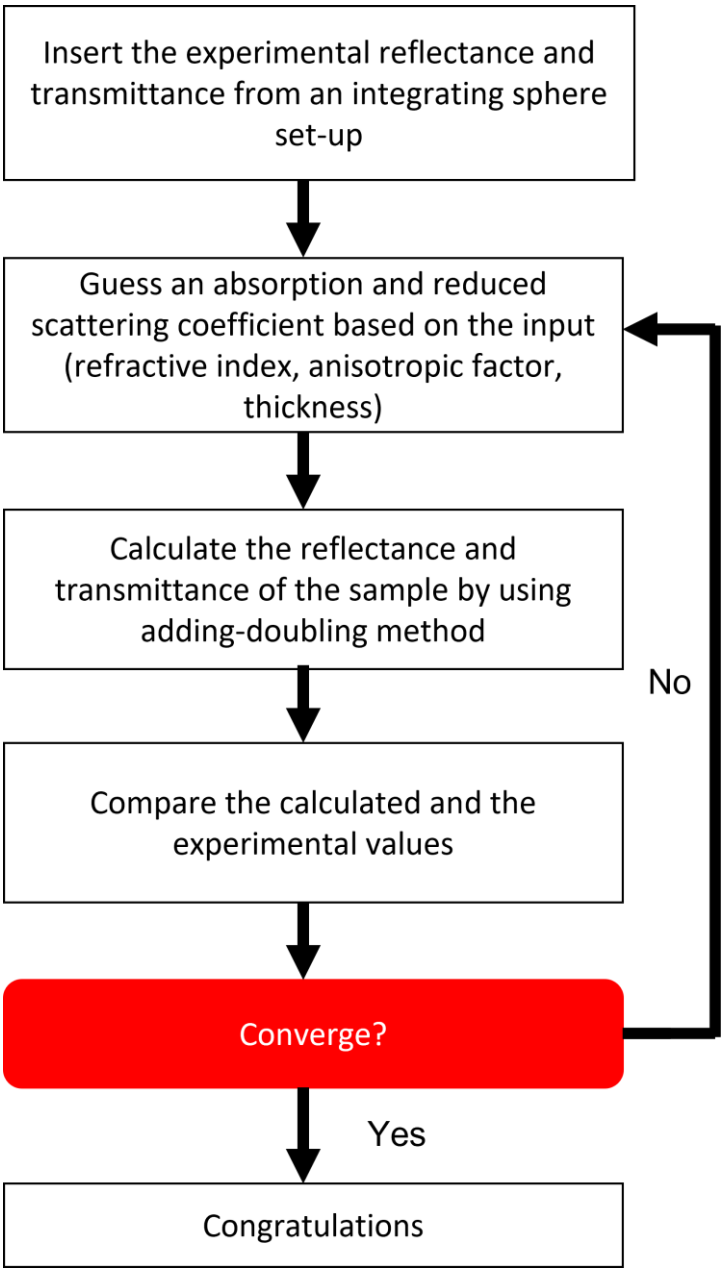

Figure 32 – General IAD algorithm diagram. Adapted from [119].

Annex C

Institut für Lasertechnologien in der Medizin und Meßtechnik
an der Universität Ulm
Helmholtzstr. 12, 89081 Ulm

Prof. Dr. Alwin Kienle
Tel: 0049 731 1429224
Fax: 0049 731 1429442
e-mail: alwin.kienle@ilm-ulm.de

28. April 2022

Feedback letter for Luismar Barbosa da Cruz Junior

To whom it may concern,

Luismar Barbosa da Cruz Junior, a Ph.D. student at the university of Sao Paulo, worked in our laboratory from September 2011 to February 2022. His research project was to investigate a method of measuring the spectrally resolved total reflectance with the constraint that the position of the investigated sample does not influence the results within a large axial range.
We were impressed by Luismar's commitment to achieve this goal. He is able to organize a logical sequence of experiments to isolate and solve problems, and has the scientific maturity to examine his own results critically. We hope to publish a paper presenting the results he obtained during his stay. In addition, Luismar gave profound talks in the seminar of our department as well as in the seminar of the whole institute.
In summary, we enjoyed having Luismar Barbosa in our lab. Besides the scientific work, we had several enjoyable meetings, where I could learn a lot from the Brazilian culture, fauna, flora and geography. Please contact me, if further information is needed.

Sincerely,

Prof. Dr. Alwin Kienle, Vice President